Finite Element Modeling in the Design and Optimization of Portable Instrumentation

by

©Behzad Parsi

A dissertation submitted to the School of Graduate Studies
in partial fulfillment of the requirements for the degree of

Master of Engineering

Faculty of Engineering & Applied Science

Memorial University of Newfoundland

Supervisory Committee

Dr. Lihong Zhang (Supervisor)

August 2018

St. John's, Newfoundland

Abstract

Finite element modeling method (FEM) is a powerful numerical analysis method that is widely used in various engineering and scientific domains. In this thesis, we have utilized FEM to study structural analysis, heat transfer, and fluid flow in the instrumentation design and optimization. In particular, we have designed and optimized a portable micro-dispenser for bio-medical applications and a portable enclosure device for industrial applications. In the micro-dispenser study, our proposed model is comprised of a permanent mainframe and a disposable main tank, which can hold a bulk volume of sample fluid as an off-chip reservoir. The height of the micro-dispenser and the diameter of the passive valve have been analytically designed upon the physical properties of the fluid sample. A Peltier thermoelectric device supported by a fuzzy logic controller is dedicated to controlling the temperature within the micro-dispenser. As an extension, we have also explored another piezoelectric-based actuator, which is further optimized by genetic algorithm and verified by FEM simulations. Furthermore, in the enclosure study, we have proposed a design and optimization methodology for the self-heating portable enclosures, which can warm up the inner space from -55°C for encasing the low-cost industrial-class electronic devices instead of expensive military-class ones to work reliably within their allowed operating temperature limit. By considering various factors (including hardness, thermal conductivity, cost, and lifetime), we have determined to mainly use polycarbonate as the manufacturing material of the enclosure. The placement of the thermal resistors is studied with the aid of FEM-based thermal modeling. In summary, despite the distinct specialties and diverse applications in this multi-disciplinary research, we have proposed our design methodologies based on FEM. The design efficacy has been not only demonstrated by the FEM simulations, but also validated by our experimental measurements of the corresponding prototypes fabricated with a 3D printer.

Table of Contents

List of Tables

List of Figures

ACKNOWLEDGEMENT

I dedicate this to my family

Chapter 1   Introduction

The physics laws for the space- and time-dependent problems can usually be expressed in partial differential equations (PDEs). For many geometry-related problems, these PDEs cannot be easily solved with analytical methods. Instead, an approximation of the equations can be utilized, typically based upon different types of discretization. These discretization methods approximate the PDEs with numerical model equations, which can be solved by using numerical methods. The solutions to the numerical model equations are in turn an approximation of the real solutions to the PDEs.

The purpose of the finite element method (FEM) or finite element analysis (FEA) is to compute such approximations. It is a numerical method for computing engineering or mathematical physics problems. It is typically comprised of the following operations: (1) divide the domain of the problem into a collection of subdomains, (2) represent each subdomain by a set of element equations to the original problem, (3) systematically recombine all sets of the element equations into a global system of equations for the final calculation, and (4) the global system of equations is calculated by using known solution techniques along with the initial values of the original problem to obtain a numerical answer. The typical problem areas of interest include structural analysis, heat transfer, fluid flow, mass transport, and electromagnetic potential. A good example of commercial FEM software is COMSOL Multiphysics, which is a powerful tool to simulate the interface among solid structure, fluid environment, and electrical field. Figure 1-1 shows the interfaces among those modules.
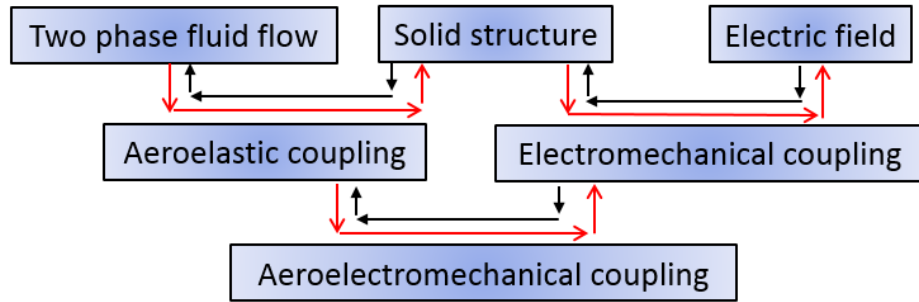
Figure 1-1 Three different interfaces in one FEM software, COMSOL Multiphysics.

The main reason for the popularity of the FEM method is its significance to the cost reduction. If utilizing the FEM software, various devices or instruments can be designed and tested without prototyping. A good example of utilizing the FEM method for structural analysis was presented by Kaviani *et al.* [1], who designed a piezoelectric actuator for a valveless micropump. An analytical model was introduced to express the natural frequencies. Then by using the FEM method, they verified the accuracy of the proposed analytical modeling method. Another study, where FEM was utilized to design a solid structure, was presented by Hu *et al.* [2]. The authors designed a new PZT (Lead Zirconate Titanate) actuator to decrease the resonant frequency as an outstanding advantage. They verified the FEM model with their experimental setup.

Similarly, Esfahani and Bahrami [3] utilized the FEM method to design an instrument, which consists of fluid flow and solid structure. They also analyzed the vibration of an edge clamp for a rectangular PZT actuator in a fluid environment. They considered the effect of fluid in the system by adding a damping coefficient to their equations, and then solved the governing equations by a numerical method. In [4], Esfahani *et al.* extended that work by investigating the effect of the input voltage, viscoelastic elements, damping coefficient, and excitation signal on the system response. They also verified their proposed analytic modeling with the FEM method by using COMSOL Multiphysics software. For the heat transfer study, the FEM method can also be a powerful tool.

3

Antonova *et al.* utilized the FEM method to design a thermoelectric device [5]. Their analysis showed that when current passed through a Peltier device, the low-temperature surface would absorb heat and the high-temperature surface would release heat [5]. However, when the direction of current changed, the hot and cold surfaces would be swapped [5].

In this thesis, two different portable instruments have been designed and optimized by using the FEM method. The first instrument is a micro-dispenser. In this design, the interfaces among solid structure, fluid environment, and electrical field were modeled, while the proposed analytical model was verified by the FEM simulations and finally validated by the measurement of the prototype manufactured with a 3D printer. As for the second portable instrument, an enclosure was designed and optimized by using the FEM method. In this study, COMSOL Multiphysics software was utilized to perform thermal analysis for the solid structure.

This thesis is organized as follows. Chapter 2 will present a literature review on the previous works. Then Chapter 3 will be focused on the description of the disposable off-chip micro-dispenser for accurate droplet transportation. Chapter 4 will present the design and optimization of piezoelectric actuators for the valveless micropump applications. And Chapter 5 will present the design and optimization of cost-effective coldproof portable enclosures for polar environment. Finally, the conclusion and future work will be provided in Chapter 6.

Chapter 2   Previous Works

2.1. Micro-Dispenser Devices

Microfluidics has received undivided attention in Lab-on-a-Chip (LOC) systems thanks to its unique offerings including sample volume reduction, fast processing time, and risk reduction when dealing with dangerous materials [6,7]. The lowered cost is another advantage for this technology, which makes it feasible to manufacture complex systems that are otherwise unjustifiable due to budgetary concerns if using other technologies especially in the biomedical applications [8]. In general, microfluidic systems can be divided into multi-phase, continuous, droplet, and digital ones. In the multi-phase microfluidic systems several immiscible fluids are separated from each other by flexible fluidic interfaces [9], while the continuous microfluidic systems utilize channels to guide fluid flow [10]. The droplet microfluidic systems operate on the discrete volumes of fluids in the immiscible phases with low Reynolds number and in the laminar flow regimes with microvalves and micropumps, which are controlled by mechanical, electrical, or other types of actuators [11]. On the other side, the term of digital microfluidics is referred to manipulating the droplets individually as digital particles on a 2D surface [8].

Most of the continuous microfluidic (CMF) systems require 3D geometries, including pre-etched or machined microchannel passages and external modules (e.g., syringe pumps and electrical or mechanical actuators). This makes the fabrication of the CMF devices complicated and in turn expensive. In addition, the dead volume left inside the microchannel would normally cause excessive waste for the sample fluids. In contrast, digital microfluidic (DMF) systems can be readily fabricated by photolithography process. The fluid manipulation mechanism of these systems does not require extensive external devices such as pumps or valves. Another crucial feature of the DMF systems is that the actuating electrodes on the chip can be fabricated on a 2D

structure with a general electrode design. As a result, a single platform can be utilized for multiple applications [12].

Featuring distinct advantages, the multi-phase, continuous, droplet, and digital microfluidic systems have been widely applied to various applications. The determination of a specific microfluidic type selection is usually dependent on type of fluids, precision requirements, cost constraints, and other design factors. To facilitate the transportation of fluids for a specific application, it is normally demanded that two or more microfluidic systems are synergistically connected into one seamless entity. For instance, in a typical parallel plate electro wetting on dielectric (EWOD) digital microfluidic device [13,14], sample fluids are loaded onto chip central surface from on-chip reservoirs as shown in Figure 2-1. If an external reservoir with larger volume is attached to this EWOD device, it is usually called off-chip reservoir, which may be implemented by another technique different from the digital microfluidics. An off-chip reservoir is normally classified as a CMF system, while an on-chip reservoir is typically categorized as a DMF system. Combining two or more microfluidic sub-systems together can help take full advantage of the distinct features from each component. However, our literature survey of the recent advances in the microfluidics area has exposed an obvious lack in such an intermediate region.

(a)

(b)
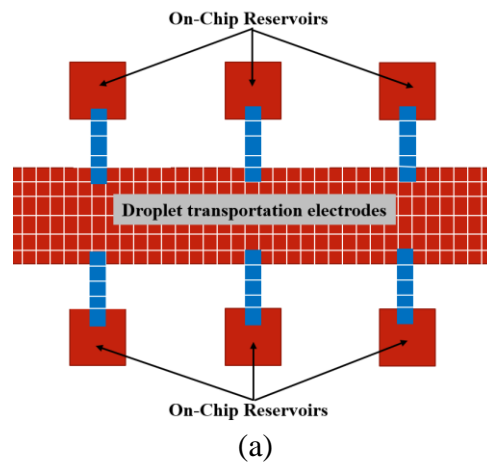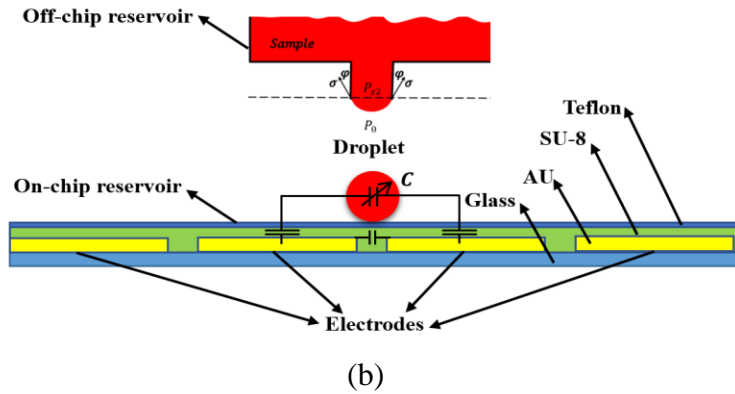
Figure 2-1 A schematic view of on-chip reservoirs in an EWOD device (a) Top view, (b) Side view

Digital microfluidics is growing in popularity in recent years [15]. Nowadays dispensing liquid to digital microfluidic devices is typically done either by manual loading with syringes/pipettes or automatic transferring with syringe pumps. In general, there exist two approaches for manually dispensing liquid to on-chip reservoirs in the digital microfluidic devices. As the first approach, the on-chip reservoirs are filled with sample fluids before the digital microfluidic devices are assembled. In contrast, as the second approach the liquid is injected from outside after the assembly of the device. Hung *et al.* [16] claimed that dispensing liquid before the assembly of EWOD systems has some problems. When a droplet is dispensed and then sandwiched between two plates, it is so pressed that certain unexpected flow may be generated or even mixed with each other. On the other hand, such an undesirable flow between the reservoirs would not happen if the on-chip reservoirs in an already assembled device are manually loaded by a thin pipette very carefully. Nevertheless, this manual operation, which demands high user experience, is difficult to control precision and reproducibility.

Chatterjee *et al.* suggested to manually load droplets onto the microfluidic chips just prior to actuation [17]. This can effectively reduce evaporative losses and potential for vapor cross-

8

contamination related to the on-chip storage. In contrast, storage of sample fluids in the off-chip reservoirs may address these abovementioned concerns. In this regard, Ren *et al*. [18] introduced a complicated system for controlling on-chip droplet dispensing with capacitance feedback (Figure 2-2) [18]. A pneumatically-driven system was developed to automatically generate continuous droplets of 0.1 M KCl aqueous solution from a sealed off-chip reservoir at high rates up to 120 droplets/minute. However, this method, although being highly expensive in the system design/manufacture, does not show how to perform a good control especially for the wetting liquid. In another research, Ding *et al*. introduced an effective system that could manipulate sample liquid from off-chip reservoirs to on-chip reservoirs (Figure 2-3) [19]. After claiming the accurate volume control as a challenge, the authors proposed an automated syringe pump and a controller unit to manage the liquid delivery in an accurate and reliable manner. They integrated the proposed system with an EWOD device for the chemical synthesis of radiotracers dedicated to medical imaging. However, their fully automated droplet dispensing system requires an expensive and complex setup.

Figure 2-2 Schematic view of the connection of the pipette to EWOD system (taken from [18]).
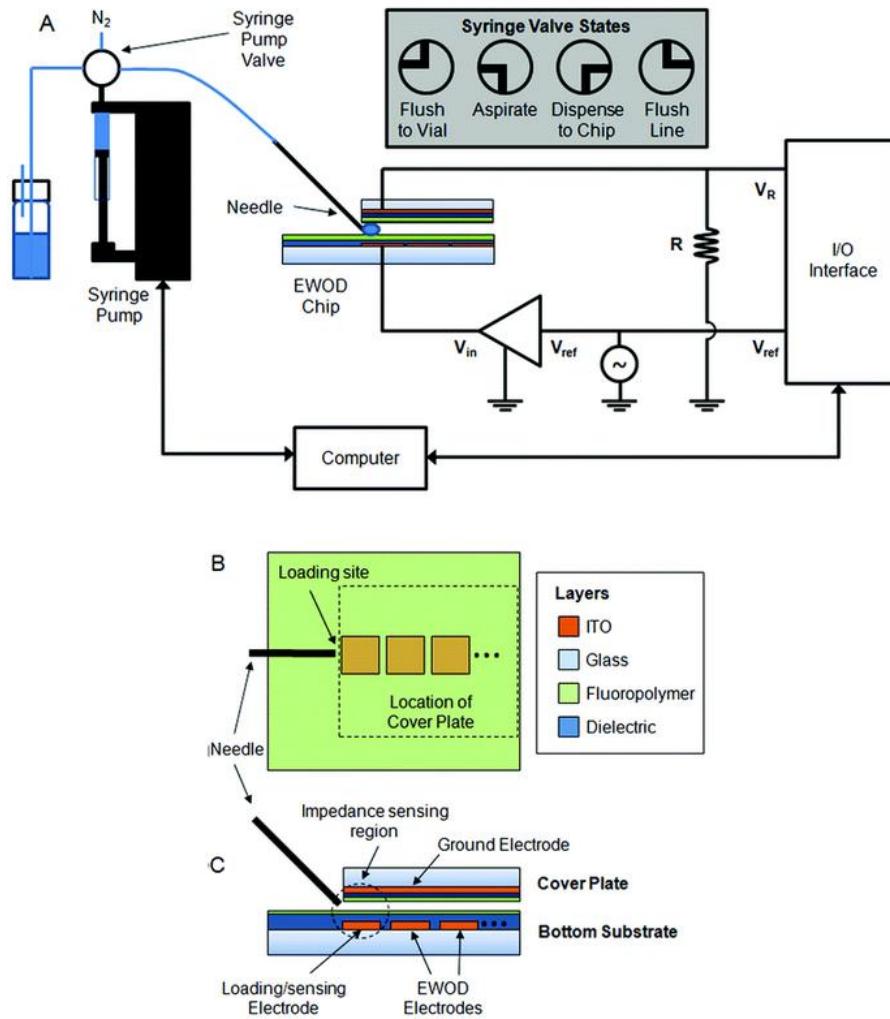
Figure 2-3 (A) A schematic of the reagent dispensing system connected to the EWOD chip. (B) Top and (C) cross-section views illustrating the position of the needle for reagent loading (taken from [19]).

Generally, the aforementioned methods have the following drawbacks. For the manual operation method, the volume of sample liquid, which must be eventually stored into the on-chip reservoirs, is limited to the size of the EWOD devices. Hence, the maximum number of the drops that can be manually dispensed is critically constrained. As a result, in some situations (such as washing cycles, repeated assays, or sample preparation operations) when a larger number of droplets is needed, more challenges may emerge due to limited accuracy in addition to evaporation

problems [20]. Moreover, another big challenge of the manual on-chip dispensing is the coarse volume accuracy and poor reproducibility of the dispensed droplets. Similarly, the method with fully automated instrumentation also has a drawback in terms of droplet size compared to the EWOD device. In addition, the limited portability and relatively prohibitive cost due to automated syringe pumps should be also considered. On the other hand, storage of sample fluids in disposable, portable, and low cost off-chip reservoirs may address all of these concerns above.

Typically, there are three continuous microfluidic micropump structures for the off-chip reservoirs, that is, mechanical micropumps, electrokinetic and magneto-kinetic micropumps, and phase-change and elctrochemical micropumps (Figures 2-5 to 2-8) [10, 21-21]. In the mechanical micropumps, the motion of a mechanical part (such as gear or diaphragm) produces pressure difference needed to move fluid. They can be further classified as rotary micropumps, moving diaphragm micropumps, and peristaltic micropumps. The electrokinetic and magneto-kinetic micropumps are based on the conversion of electrical or magnetic energy to fluid movement. Russel *et al*. proposed a micromachined electrohydrodynamic (EHD) micropump, which could create a gradient in the electrical permittivity or conductivity of the working fluid [23]. In this work, the authors studied how to enhance performance of the EHD micropumps, such as number of interdigitated electrode pairs, electrode surface topology, effect of doping ferrocene in the working fluid, and effect of external flow on the discharge characteristics. Within the category of the phase-change and elctrochemical micropumps, bubble pumps have attracted more attention owing to simplicity of the actuation method in addition to the capability of being applied to non-specific liquids. When fluid is heated, bubbles appear and gradually grow up to a steady size to fill the microchannels and cause pressure gradient for pumping action. Liu *et al*. investigated thermal bubble micropumps and proposed a new bubble generating method by using magnetic induction

11

heating [24]. It is based on wireless energy transfer between the heating plate inside the chamber and external excitation coil.
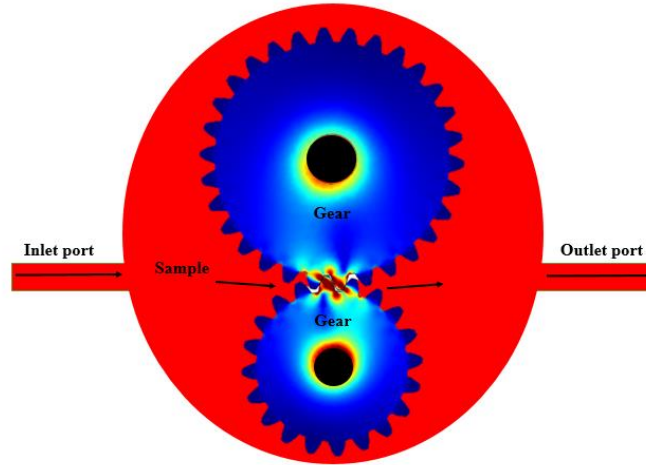
Figure 2-4 Schematic of the rotary micropump
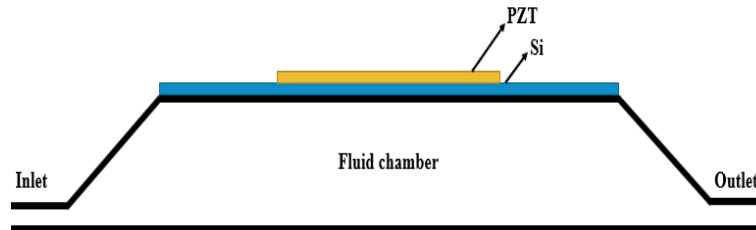
Figure 2-5 Schematic of the moving diaphragm micropump (taken from [1]).
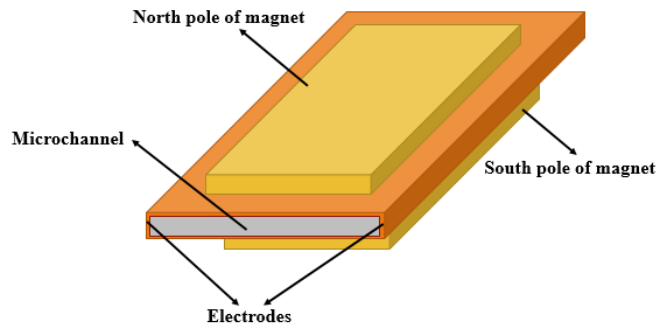
Figure 2-6 Schematic of the most common type of the magnetohydrodynamic micropump (taken from [25]).
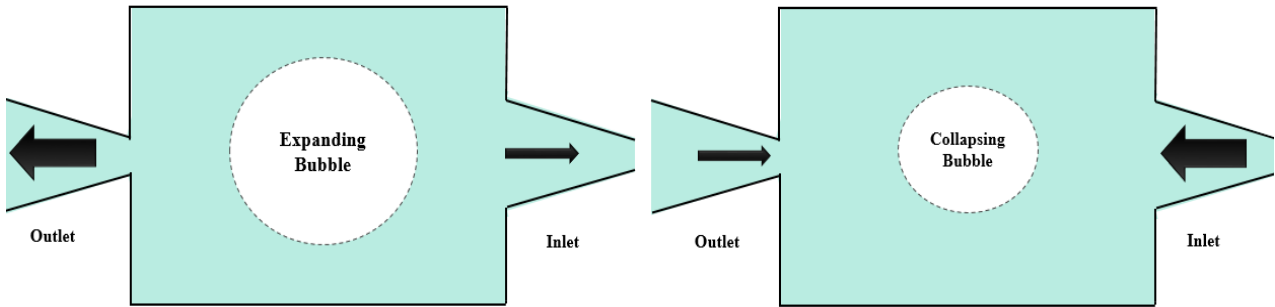
Figure 2-7 Top view of pumping chamber (taken from [27]).

On the other side, there are the following five actuation methods for manipulating fluid droplets in the digital microfluidic domain: electrical, magnetic, acoustic, optical, and thermocapillary methods (Figures 2-9 to 2-12) [25-28]. For instance, manipulation of droplets by the electrical method is also called electrowetting on dielectric (EWOD). Since the wetting behavior of droplets can be changed by electric field, the electrowetting actuation can be performed by applying AC or DC voltage.
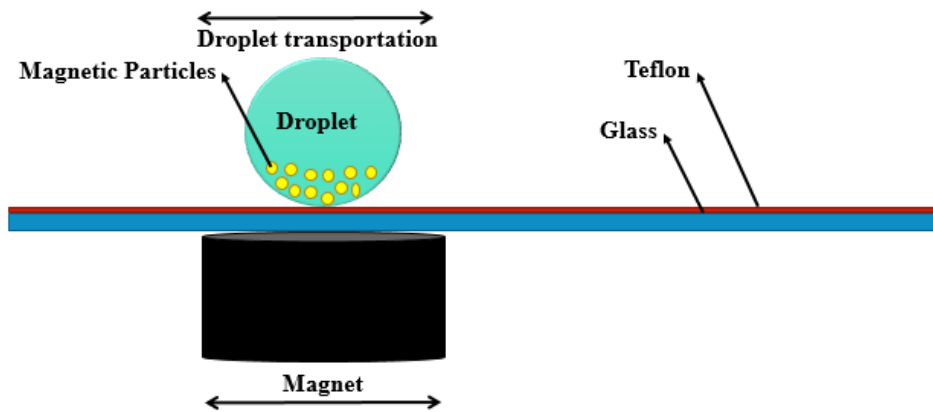
Figure 2-8 Schematic of the DMF with the magnetic actuator (taken from [26]).
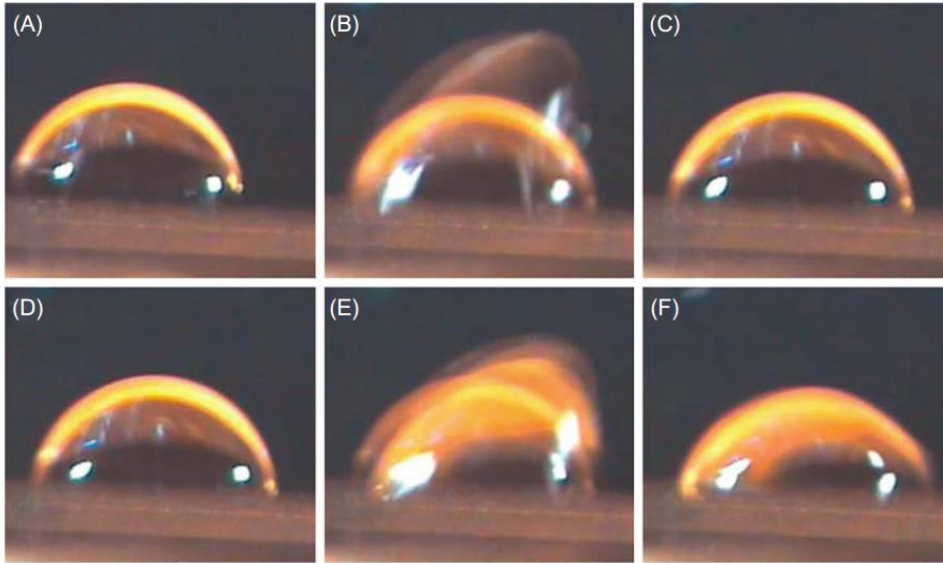
Figure 2-9 A "jumping" droplet containing 50 nL water, on a flat substrate. The snapshots are taken at consecutive times. Source: From Ref. Wixforth 2003, Elsevier, (taken from [25]).
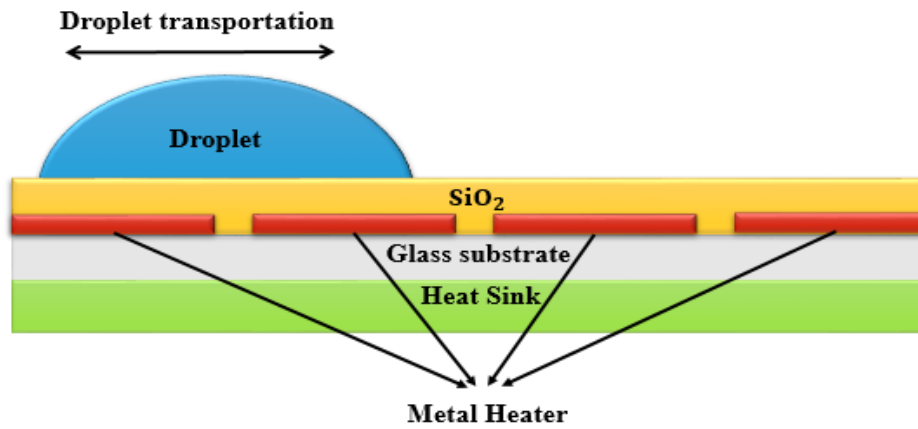
Figure 2-10 Schematic of the thermocapillary actuation method.
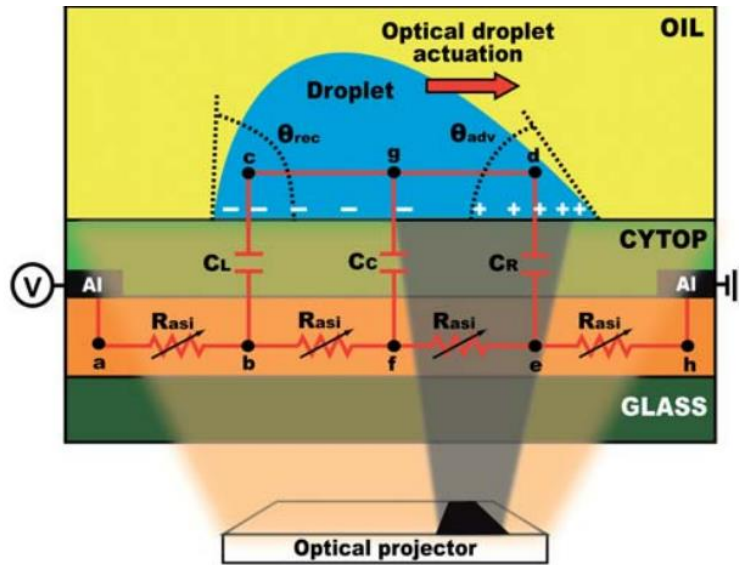
Figure 2-11 Schematic of the optical actuation method (taken from [29]).

To connect CMF off-chip reservoirs to DMF on-chip reservoirs, by nature there are two methods for the interface: active microvalve and passive microvalve [30][31]. The most well-known type of active microvalves is to use cantilevers as the key mechanical component. Usually the reservoir is equipped with a piezoelectric actuator. The volume of the reservoir can be changed from the initial flat shape to the deformed state by applying voltage to the piezoelectric material. In other words, the reciprocating motion of the piezoelectric material with the cantilever microvalve acting as a one-way valve can cause the pumping action. Its advantages include high accuracy and no leakage, while the disadvantage is its complicated fabrication process and the associated high cost. With no moving part inside, passive microvalve is based on geometry properties or nozzle/diffuser features. In other words, a nozzle-diffuser element has higher flow rate in the diffuser direction than in the nozzle direction [32]. The passive microvalves are normally less expensive and also less accurate than the active microvalves. However, if the passive microvalves are designed very carefully based on capillary forces and surface tension forces, one can build an accurate passive microvalve [33].

15

Figure 2-12 shows possible methods of transferring sample fluids into the on-chip reservoirs. The goal of this research is to make a link between CMF systems and DMF systems by dispensing fluids from a CMF off-chip reservoir to on-chip reservoirs of DMF devices. In this regard, as shown in Figure 2-12 we have proposed a new model, which is called hybrid model as a combination of the manual method and automatic method described above. As a cost-effective solution, it supports portability and disposability for small/medium laboratory environment. It can provide a holding force that prevents uncontrollable flooding onto the chip. Moreover, it can also protect sensitive reagents from environmental contamination. We have also developed a new method for sensing the dripping activity by using a piezoelectric cantilever, while in the common DMF systems such a sensing is identified by capacitance change as shown in Figure 2-12 (b).
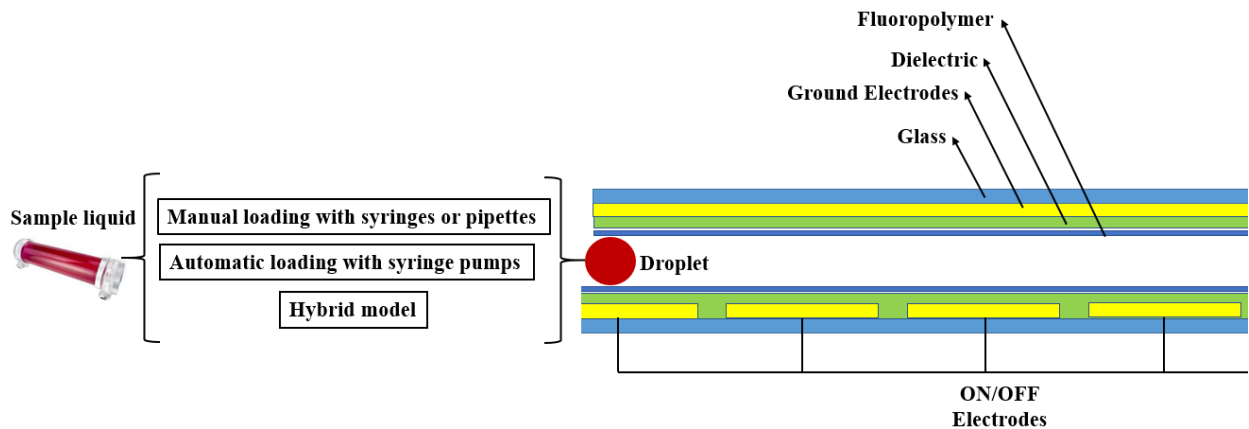
Figure 2-12 Various methods of transferring sample liquid to on-chip reservoirs.

2.2. Piezoelectric Micropumps

The concept of microfluidics was introduced 40 years ago, with the advent of inkjet printing nozzle by IBM [34]. In 1993, P. Gravesen *et al*. published a review paper about micro-pumping technologies and different actuating principles [35]. Afterwards many new fabrication

16

technologies and in turn new micropump technologies have been developed, such as the positive displacement micropump by Cunneen *et al.* in 1997 [36], the electro-osmotic micropump by Chen *et al.* in 2005 [37], the pneumatic PDMS micropump by Jeong and Konishi in 2007 [38], the piezoelectric micropump by Samira Kaviani *et al.* in 2014 [1], and the high pressure peristaltic micropump by Loth and Förster in 2016 [39]. These are just some examples of the new technologies and fabrication methods in the microfluidics area, where the micropump design is highly dependent on specific applications.

In general, being applied a voltage, a piezoelectric (PZT) layer bends inwards as a micropump [40]. This action pushes the fluid out of the chamber through the outlet valve. In the suction mode, when the voltage is removed, the PZT layer would back up to allow the fluid to enter the chamber. This reciprocating process causes the pumping action. A recent attempt of improving PZT micropump was done by Hu *et al.* in 2017 [2], who added a new layer to the previous design to decrease the resonant frequency as an advantage. The authors verified the FEM model with the experimental setup. An accurate analytic modeling for a single circular piezoelectric actuator was developed by Mo *et al.* [41]. They investigated the effect of the thickness ratio and the radius of the piezoelectric layer, which is bonded to a metallic layer with the maximum deflection by using their proposed analytic model. Moreover, a recent analytic modeling based on the thin plate theory and Kelvin–Voigt laws for a single piezoelectric actuator was proposed by Esfahani and Bahrami [3]. They also studied the vibration of an edge clamp for a rectangular PZT actuator in a fluid environment.

In this thesis, a valveless micropump with a piezoelectric (PZT) multilayer actuator has been studied for pumping fluid sample. The multilayer PZT actuator has been installed on a valveless micropump to study its effect on the flow rate of the valveless micropump. In the conventional

mechanical micropump, the motion of one component such as gear or diaphragm can produce pressure difference, which is needed to move fluid sample. The mechanical micropumps can be classified into the following categories: rotary micropumps, moving diaphragm micropumps, and peristaltic micropumps. The actuation methods of the moving diaphragm micropumps include piezoelectric, electrostatic, thermopneumatic, shape memory alloys, and other novelties. In a typical valveless micropump, there is no moving part. It works on the basis of geometric properties of nozzle and diffuser.

2.3. Enclosure Systems

A significant issue for the normal operation of electronic devices is the ambient temperature. Low temperature may change the property of the material and then change the electrical resistivity. The resistivity of intrinsic semiconductor materials increases at a lower temperature, while extrinsic semiconductor materials have more complicated temperature profiles. As a result, any change in the ambient temperature can cause variations in threshold voltage, saturation velocity, and carrier mobility of a MOSFET.

Kumar and Kursun showed that the propagation delay of various logic gates increased up to 19.6% in 180nm CMOS technology and 54.5% in 65nm CMOS technology when the temperature rose from 25°C to 125°C [42]- [43]. On the other side, when the temperature is very low, semiconductors would turn to insulators, which do not feature conductance any longer. Therefore, integrated circuits (ICs) must be warmed up first to allow bandgap voltage references to boot. Keane *et al*. claimed that low temperature of -50°C or below might terminate the normal operation of switches, relays, ICs, and other part of electrical equipment [44]. They suggested that the electronic devices should work at the temperature of -25°C or above if no heating unit is used.

Based on the International Electrotechnical Commission (IEC) standards, the electronic devices in the industrial/commercial class can only operate at the temperature between -40°C and 55°C. If any electronic device has to work below such an allowed temperature range, there may be the following two options. The first countermeasure is to use military-class electronic devices, which are normally highly expensive. As a second choice, a heating method has to be deployed to warm up the local surroundings of ICs or batteries to above -40°C if the ambient temperature is lower.

For warming up batteries, Ji and Wang compared different strategies (such as internal heating, external heating, and convection heating) in terms of warm-up time, capacity loss, system durability, cost, and lifetime [45]. They showed that with those strategies the heating time could be significantly shortened especially when reducing cell output voltage. They also claimed that the battery capacity loss was around 5% if using the high-efficiency heating method. Recently Wang *et al*. proposed a new lithium-ion battery structure for self-heating to address its power loss in cold climates [46]. This mechanism can internally warm up the battery to work normally within 20 seconds at -20°C and 30 seconds at -30°C. Nevertheless, to the best of our knowledge, thus far there is no reported work in the literature that can sustainably warm up any industrial/commercial-class electronic devices working in the extremely cold polar environment.

In this thesis, we propose an external portable structure (called enclosure hereafter) in the extremely cold environment (up to -55°C) to warm up any internal industrial-class low-power electronic systems, which may consist of ICs, sensors, and batteries normally operating at the temperature between -40°C and 55°C. For choosing the external heating sources, ceramic heating elements are studied both by using COMSOL Multiphysics software and experimentally. Since the selection of the enclosure material and isolation material is crucial for the performance of the

enclosure, we use professional software to identify the best materials for the working environment. In addition, we have developed a control system based on fuzzy logic to control the inner temperature and reduce the power consumption.

Chapter 3　Disposable Off-chip Micro-dispenser

for Accurate Droplet Transportation

3.1.   Introduction

Liquid dispensing in small scale is typically done by using either automatic syringe pumps or manual operation with syringes or pipettes. The micro-dispensers, which can precisely transport a variety of droplet fluids in the μL range, have received increasingly more attention in the area of Lab-on-a-Chip (LOC). In this paper, we present the design of a portable, efficient, accurate yet cost-effective micro-dispenser, which is ideal for improving simple laboratory applications. Our proposed design is comprised of a main frame and a disposable main tank for accommodating a bulk volume of sample fluid. The whole unit functions as an off-chip reservoir to transport the sample fluid to elsewhere through a passive valve. The height of the disposable main tank and the diameter of the passive valve are carefully designed upon the physical properties of the fluid sample. Moreover, our micro-dispenser is equipped with a flexible layer of elastic diaphragm. An electromagnetic actuator is utilized to produce push-pull force, while a Peltier thermoelectric device supported by a fuzzy logic controller is dedicated to controlling the temperature within the tank. The experimental measurements of our prototyped device exhibit that our proposed design features multiple advantages over the conventional methods, including repeatable dispensing, high accuracy, disposability, and controllable temperature.

This chapter is organized as follows. In Section 3.2, after discussing various methods that can make a link in between DMF and CMF, our new proposed model will be presented. An analytic modeling approach will be presented in Section 3.3 to calculate the critical displacement, pressure as well as the outlet hole diameter. Section 3.4 will present our developed fuzzy logic controller for temperature control, while Section 3.5 will report the experimental results. Finally, a summary is made in Section 3.6.

3.2.   Proposed Model

In this thesis, we have designed a micro-dispenser, which works as an off-chip reservoir for storing sample fluids at the user-desired temperature to be accurately transported through a passive valve on the bottom to on-chip reservoirs. We have opted for a mechanical micropump to manipulate the continuous microfluidic in the micro-dispenser in the light of simplicity and low fabrication cost (e.g., compatibility with 3D printers for easy prototyping). As for the manipulation of fluid droplets in the DFM on-chip reservoirs, any method works since it is independent of our micro-dispenser design. Figure 3-1 shows the schematic view of our proposed model.
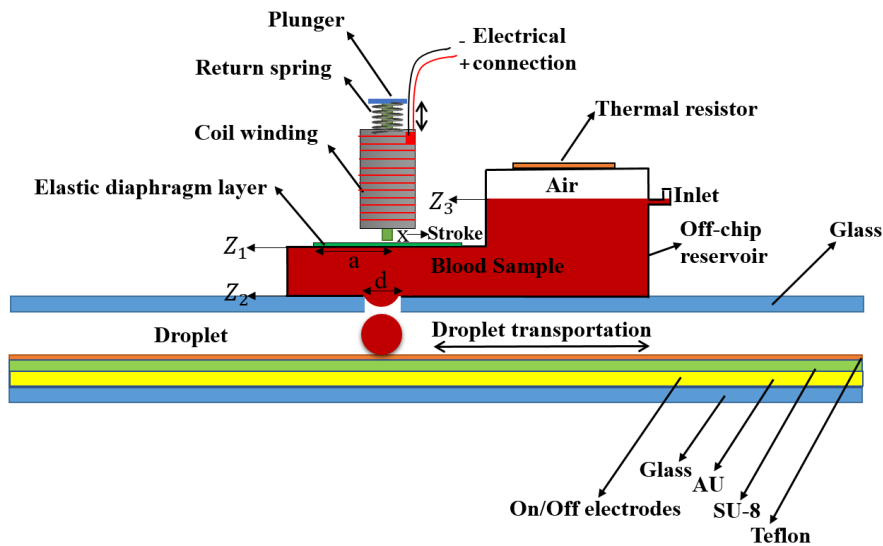
Figure 3-1 Schematic cross-sectional view of our proposed model.

As shown in Figure 3-1, our proposed model consists of a reservoir, which is filled with sample fluid passing through a passive valve. The diameter of this passive valve is carefully designed as per the physical properties of the sample fluid. For example, as reported in Section 3.5, our experiments were conducted on simulated blood. Thus, the height of the reservoir and

the diameter of the passive valve were designed specifically for this sample fluid. The reservoir is equipped with a flexible layer called *elastic diaphragm*. An electromagnet actuator is deployed to produce a push and pull force, while a thermoelectric device is selected to control the temperature of the sample fluid in the reservoir.

The main advantages of using a thermoelectric device include accurate temperature control (up to ± 0.1 $^o C$ difference), small size, and long-life time. Moreover, it can be used as either a heating or a cooling device. In our design, the thermoelectric device has no direct contact with the sample fluid. Instead a second fluid (e.g., air) with low thermal conductivity coefficient is placed between the thermoelectric device and the sample fluid because the hot surface of the thermal device may have a negative impact on the sample fluid. In our experiments, with lower density compared to the simulated blood, air first occupies the reservoir, which is then filled with the simulated blood. Since the density of air is less than that of blood (i.e., 1060 kg/m^3), air will spontaneously fill the gap between the thermoelectric device and blood. Another advantage of using a thermoelectric device is its potential to enhance the flowing rate for a quicker response by warming up the sample fluid. In this regard, it actually functions as an actuator for the situation that one needs a continuous flow instead of separate droplets.

To avoid contamination of sample fluids, in our design the reservoir is separated into two parts. As shown in Figure 3-2, the first part called *disposable tank* is disposable. It can be manufactured by a 3D printer with the fabrication cost of less than $2.50. In large volume fabrication, this cost might be reduced to under one dollar. The second part called *mainframe*, which consists of an electromagnetic actuator, a control circuit, and a thermoelectric device, is permanent. In the regular operation, the disposable main tank is first filled with one sample

fluid and then inserted into the mainframe. Figure 3-3 shows the connection between the micro-dispenser and DMF on-chip reservoirs.

Among the available materials compatible for 3D printing, polycarbonate is selected thanks to its low thermal conductivity (i.e., 0.22 Watt/(Meter·Kelvin)) and relatively high hardness (i.e., 24 HV (Hardness Vickers)). Polycarbonate is one common engineering thermoplastic material with good insulation feature and low price (i.e., $4.70 /Kg). As a result, the fabrication of our proposed micro-dispenser by 3D printing is highly cost-effective for commercial applications.
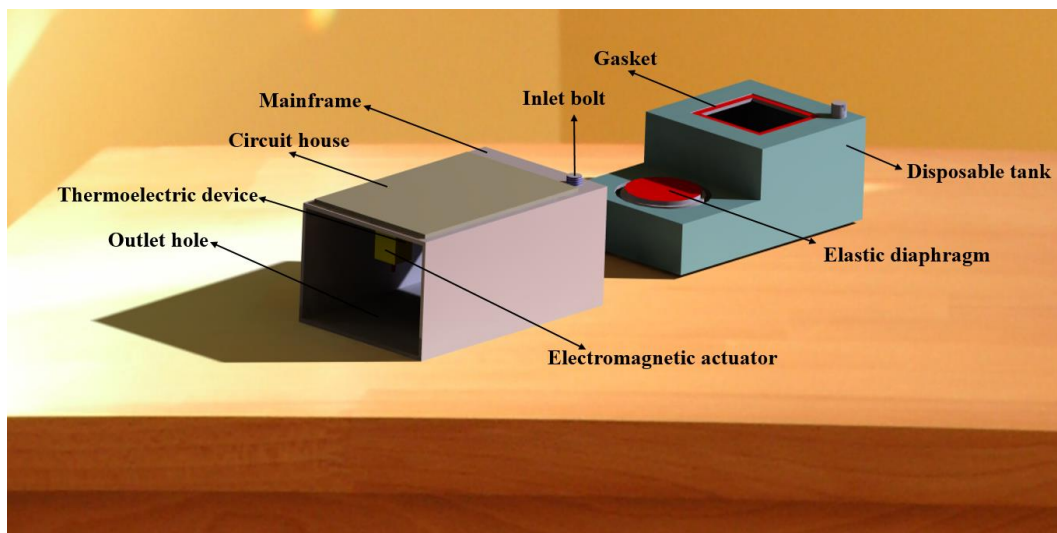
Figure 3-2 Schematic view of the mainframe and disposable tank of the proposed off-chip reservoir model.
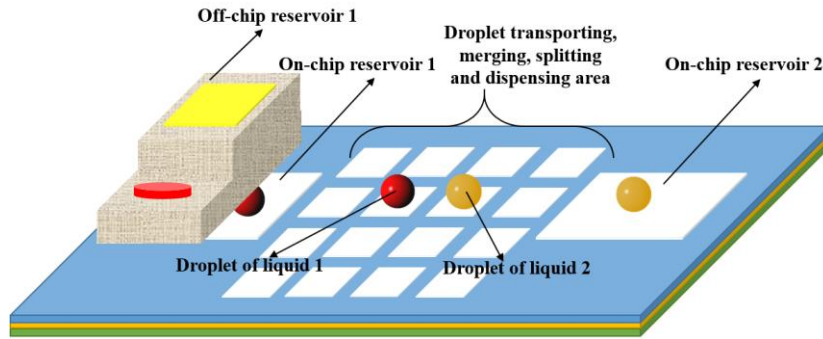
Figure 3-3 3D views of the proposed connection model between the off-chip reservoir and on-chip reservoir.

In this research, we are focusing on a versatile solution within the micro-dispenser in order to alleviate the requirements to the on-chip reservoirs in the digital microfluidic domain. As a result, instead of sensing the droplets by the on-chip reservoirs, we have proposed a new technique for sensing the dripping activity. Here a piezoelectric cantilever sensor is utilized as shown in Figure 3-4(a)-(b). Whenever a droplet falls onto the tip of the piezoelectric cantilever whose other end is anchored, the external force would be applied to the cantilever tip end to cause strain in the piezoelectric material deposited on the surface of the cantilever. This generated strain would produce electrical voltage on the piezoelectric cantilever due to the piezoelectric effect.

(a)   (b)
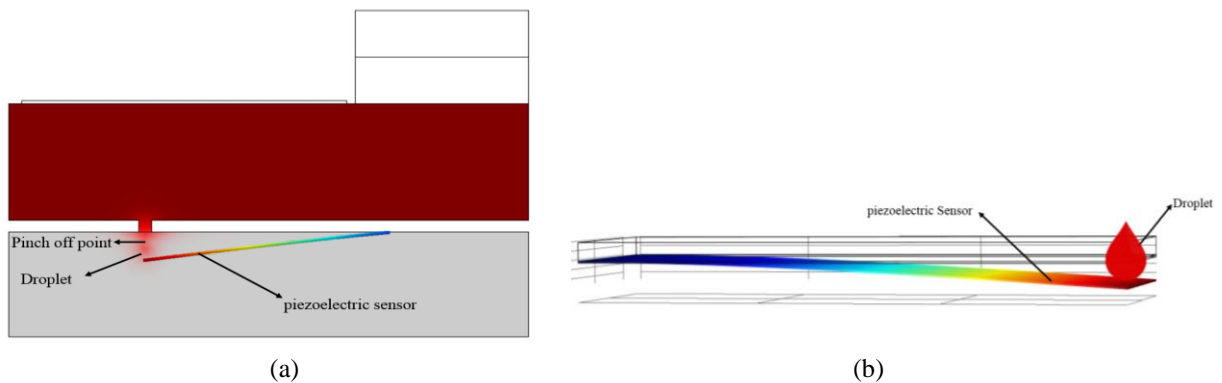
Figure 3-4 (a) Off-chip reservoir with piezoelectric cantilever sensor, (b) piezoelectric cantilever sensor.

26

3.3.　　　Analytic Modeling of the Off-Chip Reservoir

In this section, we propose a general analytic design methodology, which can help quickly estimate the critical design parameters, such as diaphragm displacement and pressure as well as the outlet hole diameter. Certain displacement and pressure have to be applied to the elastic diaphragm until a tiny droplet drips through the outlet hole of the disposable main tank. In order to generate a drip, the pressure that is caused by diaphragm displacement must overcome the surface tension and capillary force. Moreover, since the proposed micro-dispenser is a valveless device, the diameter of the outlet hole in the disposable main tank must be carefully designed so that the droplet must not drip through the outlet hole when there is no input in the stationary situation.

Figure 3-5 shows the deformation of the elastic diaphragm layer when the electromagnetic actuator applies a force. The elastic diaphragm layer is clamped along the edge and the electromagnetic actuator applies a sudden initial velocity into the center of the elastic diaphragm layer over a small circular area.
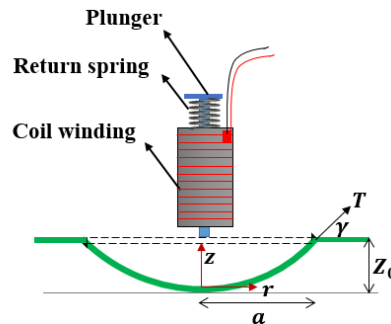
Figure 3-5 The schematic model of electromagnet actuator and diaphragm layer deformation.

Since this is an axisymmetric problem, the governing equation of the elastic diaphragm layer motion can be defined by [1]:

$$T \cdot \left(\frac{\partial^2 Z(r,t)}{\partial r^2} + \frac{1}{r} \cdot \frac{\partial Z(r,t)}{\partial r} \right) = \rho \cdot \frac{\partial^2 Z(r,t)}{\partial t^2} ,$$ (1-a)

where T is the tension, ρ is the density (i.e., mass per unit area) of the elastic diaphragm layer, Z is the transverse movement of the elastic diaphragm layer, r is the polar coordinate, and t is the time. The elastic diaphragm layer is clamped along the edge such that there is no displacement initially. As a result, the boundary equations can be written as follows:

$$Z(0,t) \neq \infty ,$$ (1-b)

$$Z(a,t) = 0 .$$ (1-c)

where a is the radius of the elastic diaphragm layer.

In this case, the initial displacement of the elastic diaphragm layer is zero and suddenly the electromagnet actuator applies velocity U. Thus, the initial conditions are defined as follows:

$$Z(r,0) = 0 ,$$ (2-a)

$$\frac{\partial Z(r,0)}{\partial t} = \begin{cases} U, & 0 < r < b \\ 0, & b < r < a \end{cases} ,$$ (2-b)

where b is the radius of the plunger of the electromagnetic actuator. To solve this problem, the separation-of-variables method will be utilized as follows:

$$\partial Z(r,t) = u(r) . v(t) ,$$ (3)

$$\frac{1}{u(r)} \cdot \left(\frac{\partial^2 u}{\partial r^2} + \frac{1}{r} \cdot \frac{\partial u}{\partial r} \right) = \frac{\rho}{T} \cdot \frac{1}{v(t)} \cdot \frac{\partial^2 v}{\partial t^2} = -\lambda^2 ,$$ (4)

$$Z(r,t) = \left(A \cdot J_0(\lambda \cdot r) + B \cdot Y_0(\lambda \cdot r) \right) \left(C \cdot \cos \left(\lambda \cdot \sqrt{\frac{T}{\rho}} . t \right) + D \cdot \sin \left(\lambda \cdot \sqrt{\frac{T}{\rho}} \cdot t \right) \right) ,$$ (5)

where λ, A, B, C, and D are unknown constant parameters, which must be determined with the aid of the initial conditions and boundaries conditions above. By applying the first boundary condition (i.e., $Z(0, t) \neq \infty$), the unknown constant B will be set to zero and (5) can be rewritten as:

$$Z(r,t) = J_0(\lambda \cdot r) \cdot \left(\tilde{C} \cdot \cos\left(\lambda \cdot \sqrt{\frac{T}{\rho}} \cdot t \right) + \tilde{D} \cdot \sin\left(\lambda \cdot \sqrt{\frac{T}{\rho}} \cdot t \right) \right). \tag{6}$$

Then when we apply the second boundary condition (i.e., $Z(a, t) = 0$), we will derive the following,

$$J_0(\lambda \cdot a) = 0, \tag{7-a}$$

$$\lambda_n = \frac{\delta_n}{a}, \tag{7-b}$$

where δ_n is the roots of Bessel function.

$$Z(r,t) = \sum_{n=1}^{\infty} J_0(\lambda_n \cdot r) \cdot \left(\tilde{C}_n \cdot \cos\left(\lambda_n \cdot \sqrt{\frac{T}{\rho}} \cdot t \right) + \tilde{D}_n \cdot \sin\left(\lambda_n \cdot \sqrt{\frac{T}{\rho}} \cdot t \right) \right). \tag{7-c}$$

Now by applying the initial condition $Z(r, 0) = 0$, the constant $\tilde{C}_n$ will be set to zero. The other unknown constant $\tilde{D}_n$ will be calculated with the last initial condition as follows:

$$Z(r,t) = \sum_{n=1}^{\infty} J_0(\lambda_n \cdot r) \cdot \left(\tilde{D}_n \cdot \sin\left(\lambda_n \cdot \sqrt{\frac{T}{\rho}} \cdot t \right) \right), \tag{8}$$

$$\frac{\partial Z(r,t)}{\partial t} = \sum_{n=1}^{\infty} J_0(\lambda_n \cdot r) \cdot \lambda_n \cdot \sqrt{\frac{T}{\rho}} \cdot \left(\tilde{D}_n \cdot \cos\left(\lambda_n \cdot \sqrt{\frac{T}{\rho}} \cdot t \right) \right), \tag{9}$$

$$\frac{\partial Z(r,0)}{\partial t} = U = \sum_{n=1}^{\infty} J_0(\lambda_n \cdot r) \cdot \lambda_n \cdot \sqrt{\frac{T}{\rho}} \cdot \left(\tilde{D}_n \cdot \cos\left(\lambda_n \cdot \sqrt{\frac{T}{\rho}} \cdot 0 \right) \right), \tag{10}$$

$$\tilde{D}_n = \frac{\int_0^b U \cdot J_0(\lambda_n \cdot r) \cdot r \cdot dr}{\sqrt{\frac{T}{\rho}} \int_0^a J_0^2(\lambda_n \cdot r) \cdot \lambda_n \cdot r \cdot dr} = \frac{2 \cdot U \cdot b \cdot J_1(\lambda_n \cdot b)}{(\lambda_n \cdot a)^2 \cdot \sqrt{\frac{T}{\rho}} \cdot J_1^2(\lambda_n \cdot a)}. \tag{11}$$

Finally, the general equation that can describe the motion of the elastic diaphragm layer due to the electromagnetic actuator movement will be rewritten as:

$$Z(r,t) = \sum_{n=1}^{\infty} J_0(\lambda_n \cdot r) \cdot \left(\frac{2 \cdot U \cdot b \cdot J_1(\lambda_n \cdot b)}{(\lambda_n a)^2 \cdot \sqrt{\frac{T}{\rho}} J_1^2(\lambda_n a)} \cdot sin\left(\lambda_n \cdot \sqrt{\frac{T}{\rho}} \cdot t \right) \right) . \tag{12}$$

Since the maximum displacement occurs when $r = 0$, (12) will be simplified to:

$$Z_0(t) = \sum_{n=1}^{\infty} \left(\frac{2 U b J_1(\lambda_n b)}{(\lambda_n \cdot a)^2 \cdot \sqrt{\frac{T}{\rho}} J_1^2(\lambda_n \cdot a)} \cdot sin\left(\lambda_n \cdot \sqrt{\frac{T}{\rho}} \cdot t \right) \right) \tag{13}$$

In a similar way, the constant tension can be calculated from the membrane stress by considering the thickness and circumference of the membrane as follows,

$$\sum F_Z = 0 \Rightarrow P_{z1} \cdot \pi \cdot a^2 = -T \cdot sin(\gamma) = -\sigma_e \cdot h \cdot 2 \cdot \pi \cdot a \cdot sin(\gamma) , \tag{14}$$

$$P_{z1} \cdot \pi \cdot a^2 = -\sigma_e \cdot h \cdot 2 \cdot \pi \cdot a \cdot sin(\gamma) , \tag{15}$$

where P_{z1} is the pressure at level Z_1 , h is the thickness of the membrane, σ_e is the equivalent stress of the thin circular membrane, γ is the angle between the surface tension force and the horizontal line, and T is the tension of the thin circular membrane. For a small angle of γ, (15) can be rewritten as [47]:

$$P_{z1} \cdot \pi \cdot a^2 = -\sigma_e \cdot h \cdot 2 \cdot \pi \cdot a \cdot \frac{\partial Z}{\partial r}|_{r=a} , \tag{16}$$

where Z is defined as follows by considering the feature of the circular membrane,

$$Z(r) = Z_0 \cdot \left(\frac{a^2 - r^2}{a^2} \right) . \tag{17}$$

By inserting (17) into (16), we can solve it for pressure:

$$P_{z1} = \frac{4 \cdot \sigma_e \cdot Z_0 \cdot h}{a^2}. \tag{18}$$

After that, we insert the equivalent stress (σ_e) in the function of specific geometry (Z_0 and a), Young's module (E), and Poisson's ratio (ν) of the thin circular membrane, which can be obtained from any material mechanics books, into (18). Then we can derive the final expression to describe the maximum pressure that the membrane can provide,

$$P_{z1} = \frac{8 \cdot h \cdot E}{3a^4 \cdot (1-\nu^2)} \cdot \left(\sum_{n=1}^{\infty} \left(\frac{2 \cdot U \cdot b \cdot J_1(\lambda_n \cdot b)}{(\lambda_n \cdot a)^2 \cdot \sqrt{\frac{T}{\rho}} J_1^2(\lambda_n \cdot a)} \, sin\left(\lambda_n \cdot \sqrt{\frac{T}{\rho}} \cdot t \right) \right) \right)^3. \tag{19}$$

In order to establish the expression of pressure-change as a function of depth, the following equation will be utilized to calculate the pressure at the bottom of the disposable main tank:

$$P_{Z_2} - P_{Z_1} = \rho_b \cdot g \cdot (Z_1 - Z_2), \tag{20}$$

where the density ρ_b is a constant, Z_1 is the height of level Z_1 (as shown in Figure 3-1), Z_2 is the height of level Z_2 (as shown in Figure 3-1), and g is the Earth's gravity constant. As a result, the pressure in term of depth can be expressed by:

$$P_{z2} = P_{z1} + \rho_b \cdot g \cdot (Z_3 - Z_1) + P_0 + \rho_b \cdot g \cdot (Z_1 - Z_2), \tag{21}$$

where P_{z2} is the pressure at level Z_2, Z_3 is the height of level Z_3 (as shown in Figure 3-1), and P_0 is the atmosphere pressure.
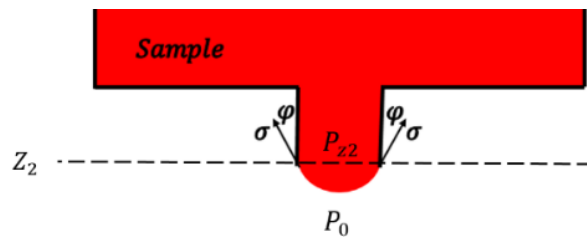
Figure 3-6 Schematic of the outlet hole in the disposable tank

In the outlet of the disposable main tank, there is an interface between the sample fluid and air. In order to find the critical outlet diameter, the stationary situation will be studied. The stationary situation means that the summation of the external and internal forces is equal to the interfacial tension force as shown in Figure 3-6,

$$P_{z2} \cdot \pi \cdot r^2 - P_0 \cdot \pi \cdot r^2 = 2 \cdot \pi \cdot r \cdot \sigma \cdot \cos(\varphi) , \tag{22}$$

where P_{z2} is the pressure at the height z_2, P_0 is the atmosphere pressure, r is the radius of the outlet hole, φ is the contact angle, and σ is the surface tension. By solving Equation (24), we can derive the following:

$$r = \frac{2 \cdot \sigma \cdot \cos(\varphi)}{(P_{z2} - P_0)} . \tag{23}$$

3.4.   Fuzzy Logic Controller

Controlling the tank temperature of the off-chip reservoir is an essential part of this research. We have developed a fuzzy logic controller to control the inner temperature of the disposable tank. In general, the fuzzy logic control method is useful for the systems that can hardly be mathematically modeled [48]. In our study, the required power that the thermoelectric device needs to heat up the disposable tank is the input of our target system to be controlled, while the temperature that is read out by the temperature sensor is the output of our target system.

The Fuzzy Logic Controller (FLC) consists of four components: fuzzification interface, knowledge base, inference engine, and a defuzzification interface. Each of these components has a different role in the control process and thus affects the performance of the whole system. The fuzzification interface is a mapping operation of numerical data from the input to linguistic terms. The knowledge base works as a knowledge source to provide necessary information for all the

components of the fuzzy controller. The inference engine, also called logical decision maker, is actually the brain of the controller. In other words, it simulates the decision-making process of human beings. Table 3-1 lists the properties of the inference engine for our proposed FLC. We have used the Mamdani-type inference engine with the applied options for and-method, or-method, implication, and defuzzification. At the end of the inference stage, the obtained result is a fuzzy value that cannot be directly used to control the real world (e.g., the temperature in our case). Thus, this fuzzy value has to be defuzzified through the defuzzification interface to a crisp value to be directly used outside [49].

Table 3-1 Properties of the fuzzy logic controller

Name	Applied Option
Controller type	Mamdani
And method	Min
Or method	Max
Implication	Min
Defuzzification	Centroid

A membership function is a curve that defines how each point in the input space is mapped to a membership value (or degree of membership) between 0 and 1. It is important for the fuzzification and defuzzification stages of the FLC to evaluate the non-fuzzy input values to fuzzy linguistic terms. A membership function can be implemented to measure the linguistic terms. For instance, the membership functions for the linguistic terms of the temperature variable used in our proposed FLC are depicted in Figure 3-7.

Figure 3-7 Correspondence between fuzzy input values and linguistic terms.

In the fuzzification process, a real scalar value is mapped into a fuzzy value. The arrangement of fuzzy variables through the defined membership functions can ensure that these real values get translated into the proper fuzzy values. After translating such real values into fuzzy values as shown in Figure 3-7, the possible outcome is called "linguistic terms". The control rules are used to further convert the linguistic terms to the output linguistic variables, which linguistically express the applied values to the real world, i.e., the thermoelectric device for temperature control in our proposed FLC. In Table 3-2, we present the developed rules of our proposed FLC. The linguistic input terms include *very negative*, *negative*, *zero*, *positive*, *very positive*, while the linguistic output variables include *zero*, *very low*, *low*, *high*, *very high*.

Table 3-2 Control rules of the developed fuzzy logic controller

Controller Rule I	If the temperature difference is very negative, then the power must be zero
Controller Rule II	If the temperature difference is negative, then the power must be very low
Controller Rule III	If the temperature difference is zero, then the power must be low

34

Controller Rule IV	If the temperature difference is positive, then the power must be high
Controller Rule V	If the temperature difference is very positive, then the power must be very high

As can be observed in Figure 3-7, the input of the fuzzy sets is defined as the temperature difference between the reference temperature (i.e., 14°C) and the actual sampled temperature. Based on the input fuzzy terms, our developed fuzzy control rules can give an appropriate output fuzzy set and then in turn a specific power value as shown in Figure 3-8.
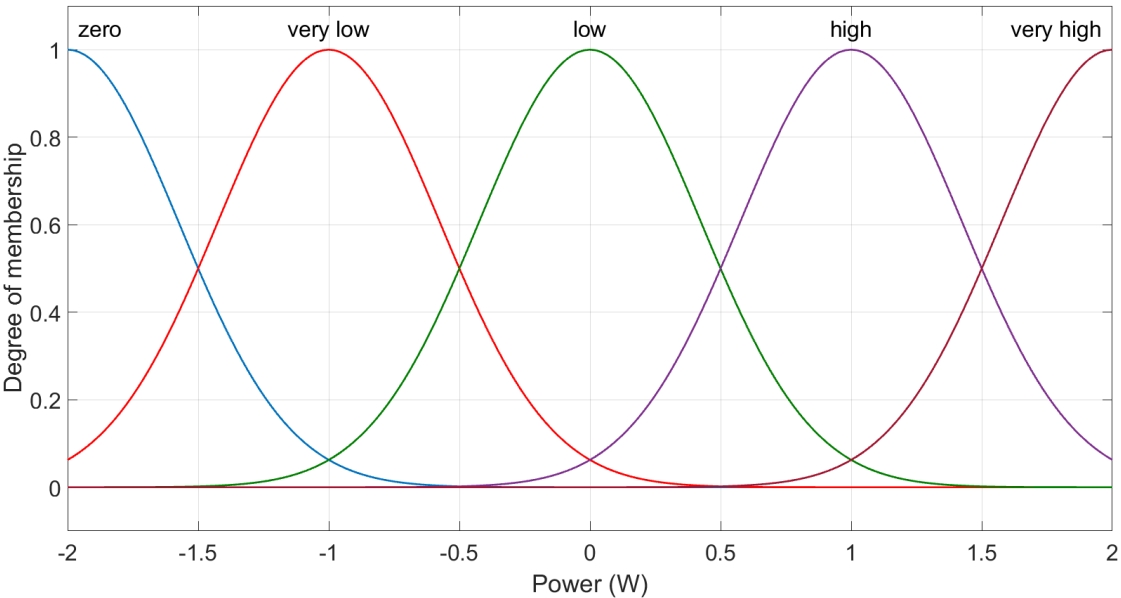
Figure 3-8 Membership functions corresponding to fuzzy out sets.

Figure 3-9 shows an example of mapping a fuzzy input (i.e., temperature difference) to a fuzzy output (i.e., power). Here, assumes the temperature difference to be 5°C. This point on that scale has five truth values (one for each of the five functions). The vertical red line in the left image represents a particular temperature difference (5°C). Since the vertical line in the first row indicates zero, this temperature difference may be interpreted as "very negative". Similarly, the second, third, fourth, and fifth rows may be interpreted as "negative", "zero", "positive", and "very

35

positive", respectively. In the next step, for each truth value, the membership function must be evaluated and then with the or-operator the resulting curves will be combined. In the defuzzification step, the weight-center of the shaded area of the curves will be determined. Finally, the X-axis position of this center is actually used as the final output power (i.e., 0.427W) of the FLC system.
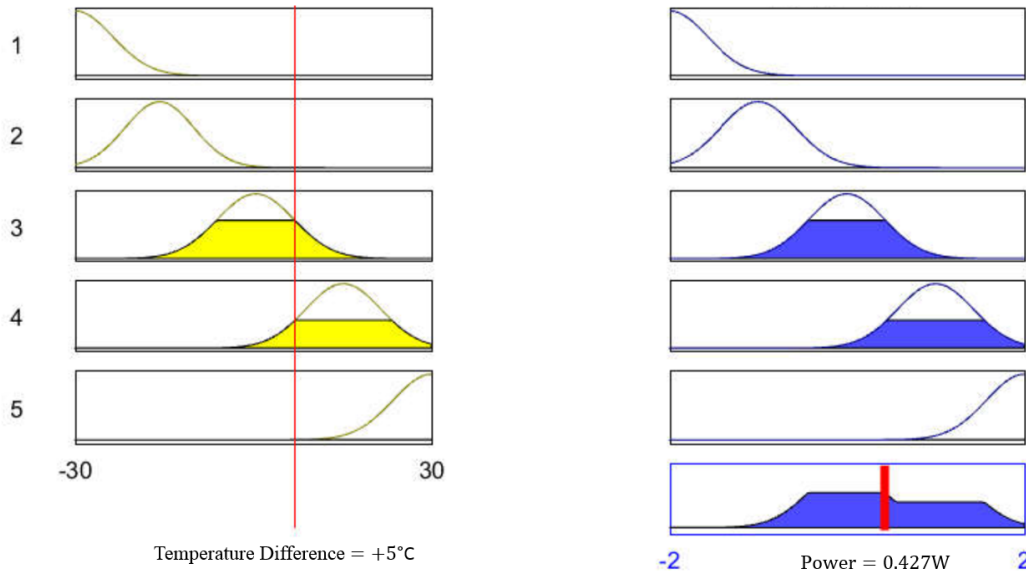
Figure 3-9 An example of the correspondence/mapping between fuzzy input and output set.

3.5.   Experimental Setup and Results

By following the discussion in Section 3.3, we prototyped the proposed micro-dispenser (including the mainframe and disposable main tank) as shown in Figure 3-10 with polycarbonate by using a 3D printer (Formlabs Form 2SLA). We used simulated blood as the sample fluid in our experiments. In the experimental setup, sensing is an indispensable part for the system design. In this regard, we need a sensor to form a closed-loop system, which can determine whether the droplet drips or not. In certain situations, more than one droplet is

36

needed. Therefore, dripping has to be sensed so that the user can decide what to do in the next step.
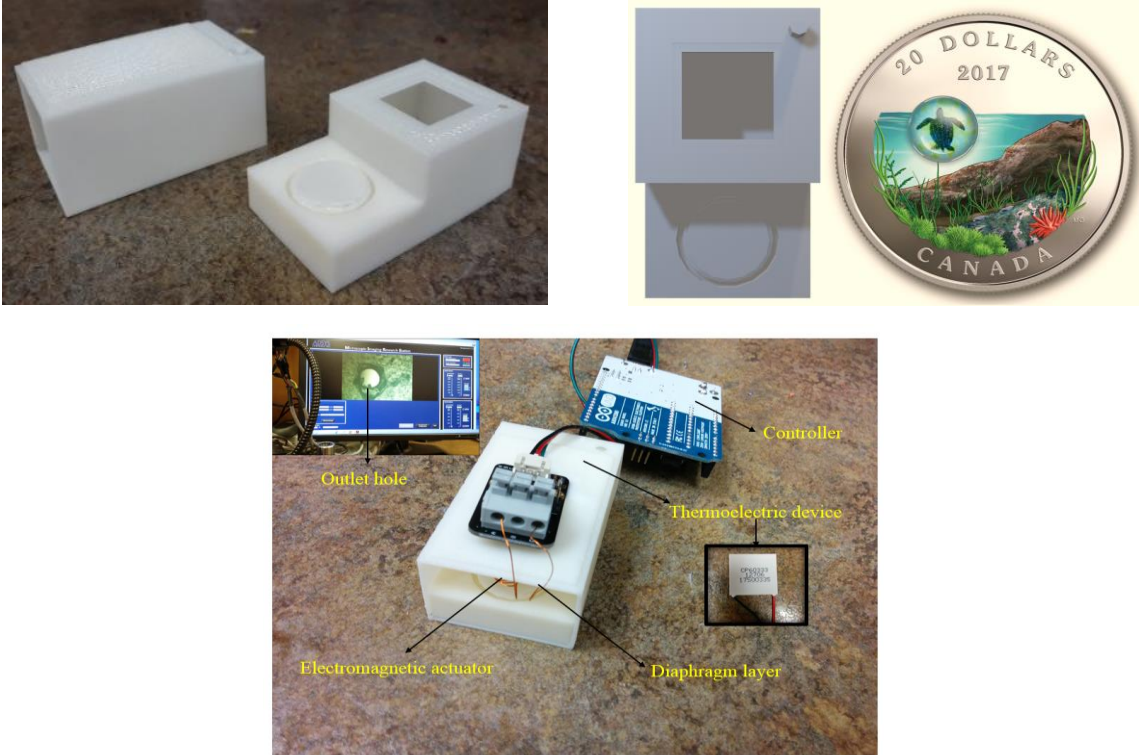
Figure 3-10 Prototyped off-chip reservoir

Table 3-3 Material properties of the elastic diaphragm layer (i.e., silicon nitride), sample fluid, and polycarbonate wall [50] [51].

Mechanical property	Silicon nitride (Si3N4)	Artificial blood sample	Polycarbonate
Mass density	3290 (Kg/m^3)	1060 (Kg/m^3)	1220 (Kg/m^3)
Elastic modulus	310 (GPa)	---	2.4 (GPa)
Uniform tensions per unit length	12.66 (N/m)	---	--
Poisson's ratio	0.27	---	0.37
Thermal Conductivity	---	0.52 (W/m/C)	0.22 (W/m/C)
Viscosity	---	3.65E-3 $(Pa.s)$	---
Heat Capacity of blood	---	3617 (J/kg/C)	1.3 (KJ/kg/C)

As can be seen in Equation (19), the diaphragm pressure is a function of time. In order to find the critical displacement, the maximum pressure that can be applied to the system must be first calculated. Therefore, by substituting the physical parameters of the elastic diaphragm layer and blood sample fluid as listed in Table 3-3, Equation (19) can be solved numerically. Figure 3-11 shows the pressure as a function of time, where the maximum pressure is $2.0087e^6\ pa$ and the corresponding displacement is equal to $1.898\ e^{-3}\ m$.
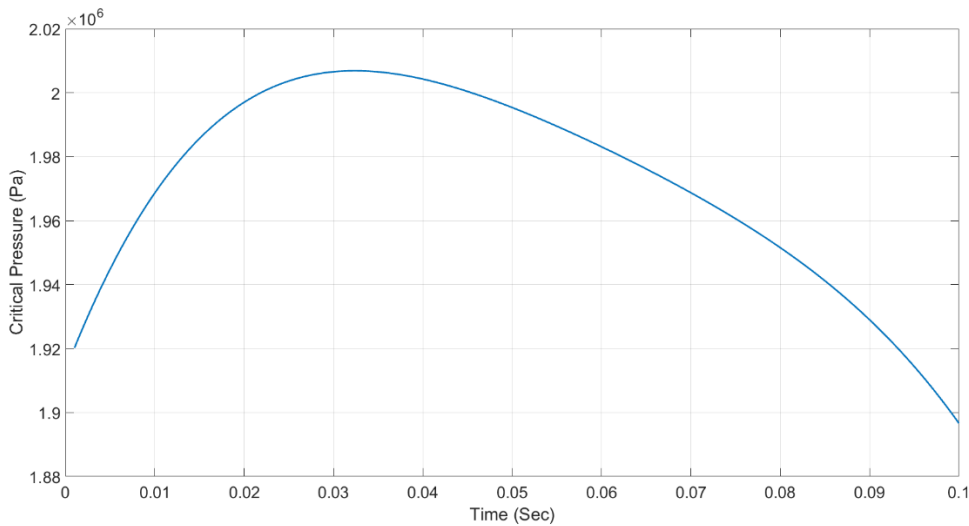
Figure 3-11 Critical pressure curve as a function of time in one cycle.

By using the physical parameters of the elastic diaphragm layer and blood sample fluid as listed in Table 3-3, the critical outlet hole diameter is calculated to be $0.4978\ mm$. In other words, if the diameter of the outlet hole is equal to $0.4978\ mm$, in a stationary situation there is no drip through the outlet hole. When the displacement of the elastic diaphragm reaches $1.898\ e^{-3}\ m$, the surface tension force is not strong enough to hold the fluid so that one droplet will drip through the outlet hole. In the later part of this section, this diameter will be refined to include the effect of temperature, which is another important factor to be considered.

Equations (19-23) can be solved numerically by a common software such as MATLAB or MAPLE so that the designer can quickly calculate the maximum static pressure and the required

outlet hole diameter for the specific materials and micro-dispenser dimensions. After calculating the critical displacement, we conducted a group of FEM simulations to verify the droplet motion by using COMSOL Multiphysics software, a powerful software tool for simulating the interface among solid structure, fluid environment, and electrical field.

(a)   (b)
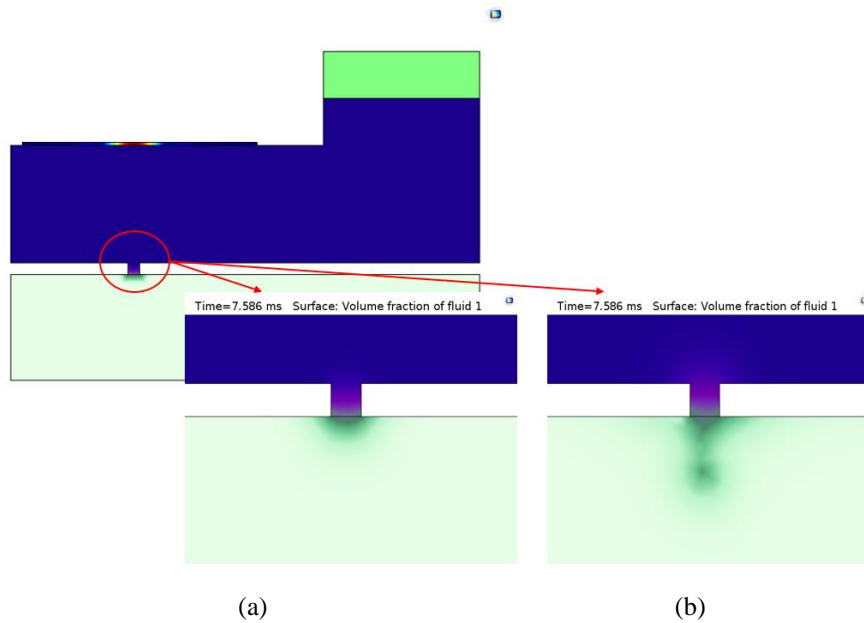
Figure 3-12 FEM simulations when the elastic diaphragm layer is applied by (a) a displacement less than the critical displacement, (b) a displacement a little greater than the critical displacement.

Figure 3-12 (a) shows the COMSOL simulation result when the maximum displacement $1.6\ e^{-3}m$ of the elastic diaphragm is less than the critical displacement (i.e., $1.898e^{-3}$m). As can be seen from the figure, the droplet grew up gradually, but the pressure produced by the diaphragm was less than the surface tension force applied to the droplet. As a result, there is no drip in Figure 3-12 (a). Figure 3-12 (b) shows another micro-dispenser in the same condition and time step, while the displacement $1.92\ e^{-3}m$ of the elastic diaphragm layer is over the critical displacement. Since the pressure induced by the elastic diaphragm layer is more than the surface tension forces, the droplet gradually grew up and then dropped.

In addition, another group of simulations was executed to find out the droplet dripping behavior along the time. Figure 3-13 shows the formation of the droplet in the time domain. As can be seen in this figure, the droplet gradually grew up and finally dripped at 7.586 ms. Figure 3-14 shows the experimental measurement setup when the displacement ($1.90\ e^{-3}m$) of the elastic diaphragm is a little larger than the critical displacement. As can be seen in this figure, the droplet gradually grew up and then dropped.
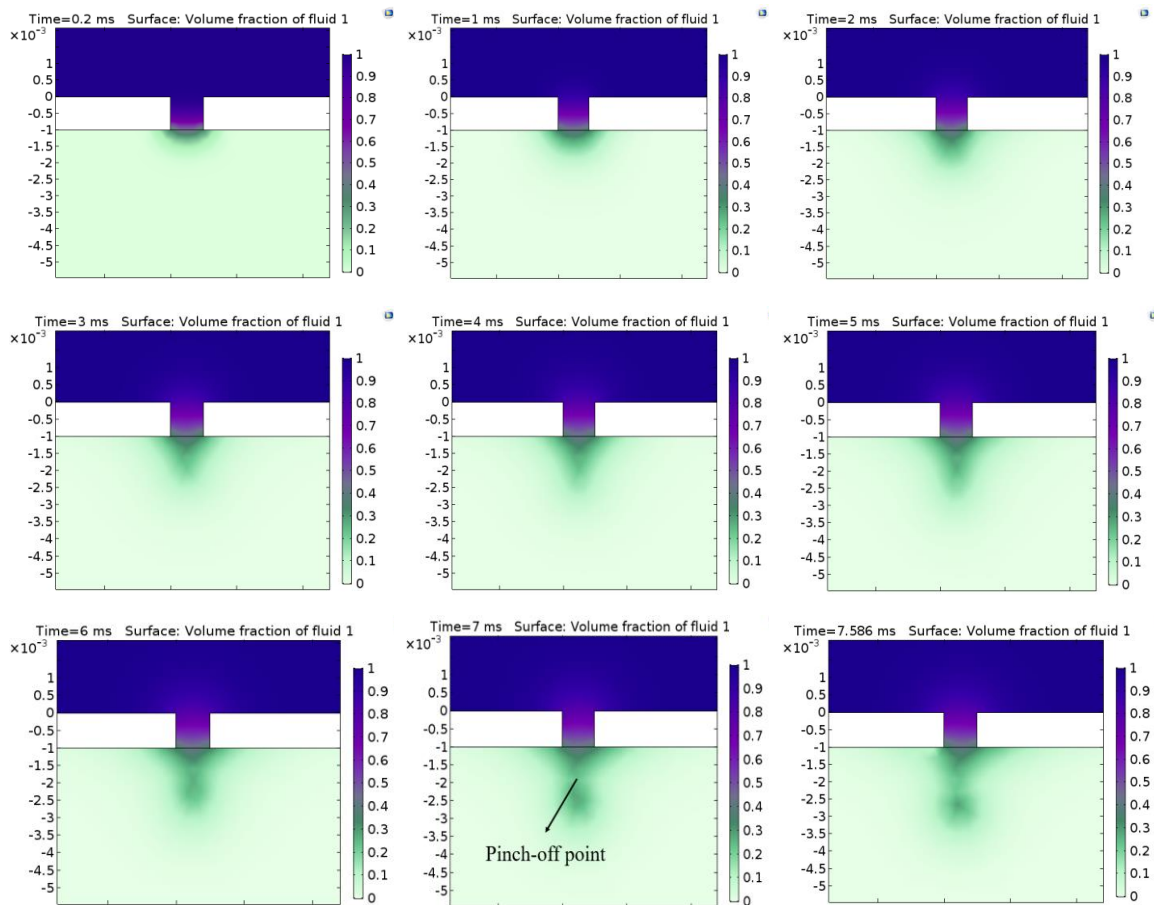
Figure 3-13 FEM simulations in the time domain from $0.1\ ms$ to $7.5\ ms$ when the displacement is a little greater than the critical displacement applied to the elastic diaphragm layer
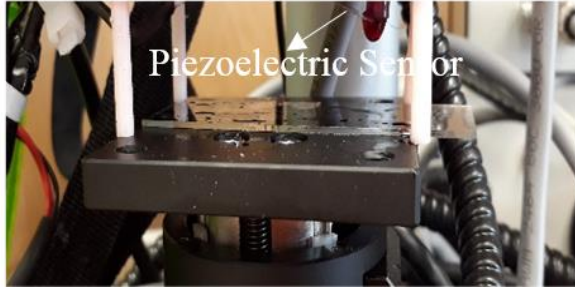
(a)
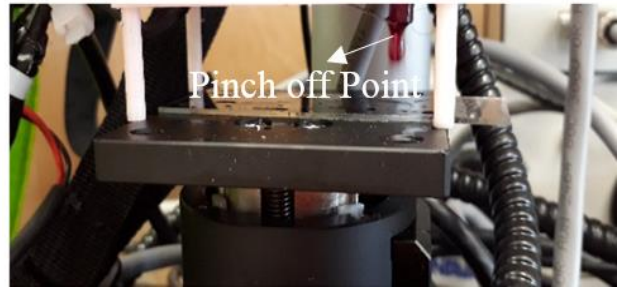
(b)
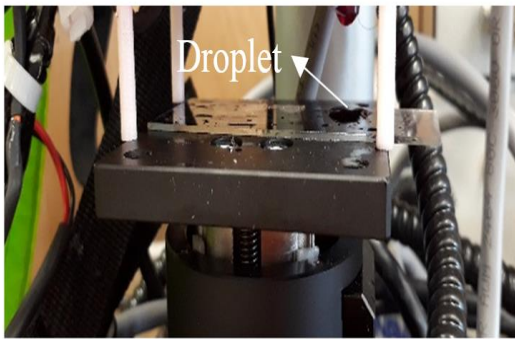
(c)
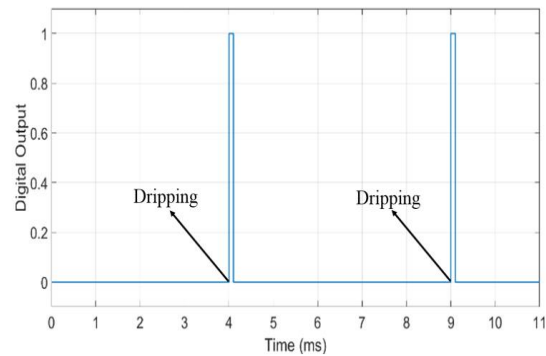
(d)

Figure 3-14 The experimental setup from $4\ ms$ to $8.9\ ms$ when the displacement is a little greater

than the critical displacement applied to the elastic diaphragm layer.

As shown in Figure 3-1 , we have included a thermoelectric device that can regulate the temperature of sample fluid. In some cases, there is a need to increase or decrease the temperature of sample fluids. For example, a washing buffer needs to warm up blood sample to 65 °C before extracting DNA [52] [53] [54], while blood sample has to be warmed up to room temperature quickly when it is taken from refrigerated storage (2°C~ 6°C). Therefore, changing the temperature of sample fluid is an essential feature of our proposed micro-dispenser. The temperature, which has a great impact on surface tension, would affect equation (23). When the temperature increases, surface tension force becomes less. In order to measure various surface tension constants at

different temperatures, an experimental setup was utilized in a temperature chamber as depicted in Figure 3-15(a). After doing the experiments at different temperatures, the correlation between temperature and surface tension constant is plotted in Figure 3-16. By using curve fitting technique, we can derive the following analytic equation with a root-mean-squared (RMS) error of 0.27%:

$$\sigma = 0.0602e^{-\left(\frac{T-287.6}{88.18}\right)^2} \, ,$$
(24)

where σ is the surface tension factor and T is the temperature in the unit of Kelvin. As a result, equation (23), where the radius of the outlet hole in the disposable main tank is a function of temperature, can be rewritten as follows:

$$r = \frac{0.378e^{-\left(\frac{T-287.6}{88.18}\right)^2}.\cos(\varphi)}{(P_{Z2} - P_0)} \, .$$
(25)
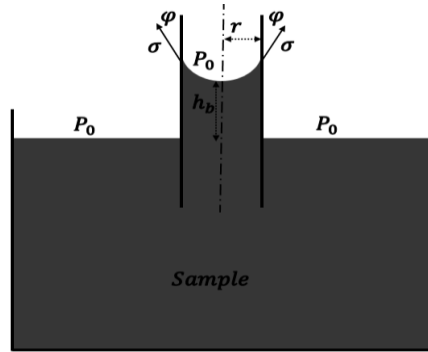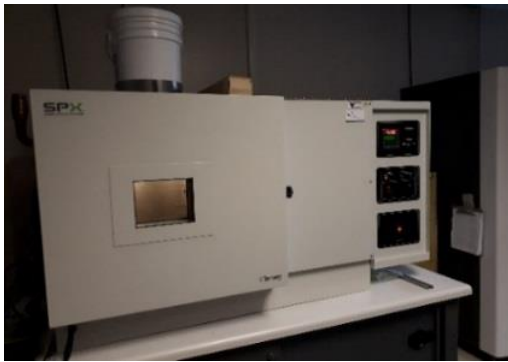
Figure 3-15 Experimental setups for measuring the surface constants at different temperatures.

As can be seen in figure 3-15, a vertical glass tube is used. If a tube is sufficiently narrow and the liquid adhesion to the walls is sufficiently strong, surface tension can draw liquid-up the tube in a phenomenon known as capillary action. The height to which the column is lifted is given by Jurin's-law. This experiment has been done several times in the different temperature conditions which are controlled by our temperature chamber.
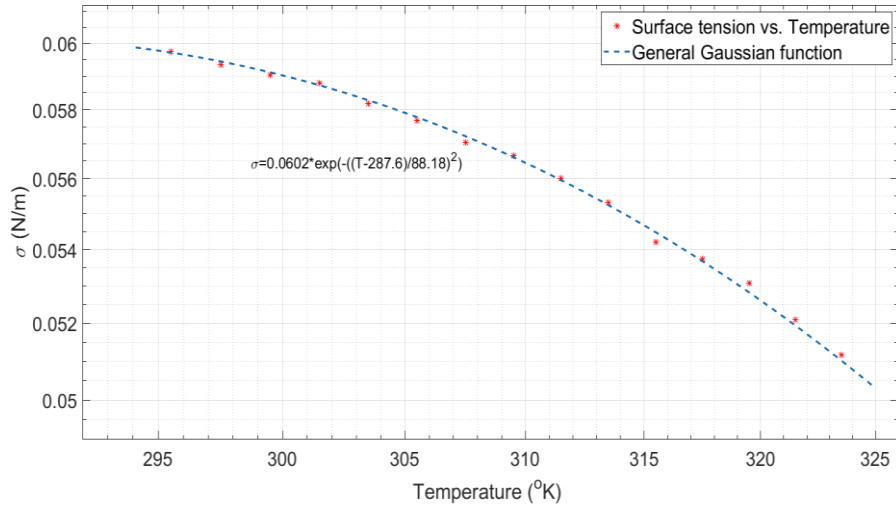
Figure 3-16 Surface tension constant as a function of temperature

We have selected a thermoelectric device (CP60240) as our heating/cooling element in the prototype. The main advantage of utilizing a thermoelectric device is that when electrical current passes through such a Peltier device, the low-temperature surface will absorb heat and the high-temperature surface will release heat. When the direction of the electrical current changes, the hot and cold surfaces will actually be swapped [55]. In other words, the direction of heat dissipation is completely reversible so that a heating device might be changed to a cooling device if the electrical polarity changes. Therefore, a combination of a thermoelectric device and a control unit can be built up for our micro-dispenser to regulate the temperature of sample fluids. Figure 3-17 shows the FEM modeling of our micro-dispenser with a thermoelectric device that can cool or heat the sample fluid within the disposable main tank. As can be seen in Figure 3-17, the thermoelectric device has no direct contact with the sample fluid. In fact, a second fluid (e.g., air) with low thermal conductivity coefficient is placed between the thermoelectric device and sample fluid since the surface of the thermoelectric device may be so hot that a negative impact is made on the sample fluid. By utilizing such a second fluid, the impact of this phenomenon is eliminated. Our simulation

43

shows that the temperature difference between the top and bottom surfaces of the second fluid is

around 27^oC. In this model, the boundary conditions are defined as a surface heat flux at the top

and zero convective heat flux at the walls.
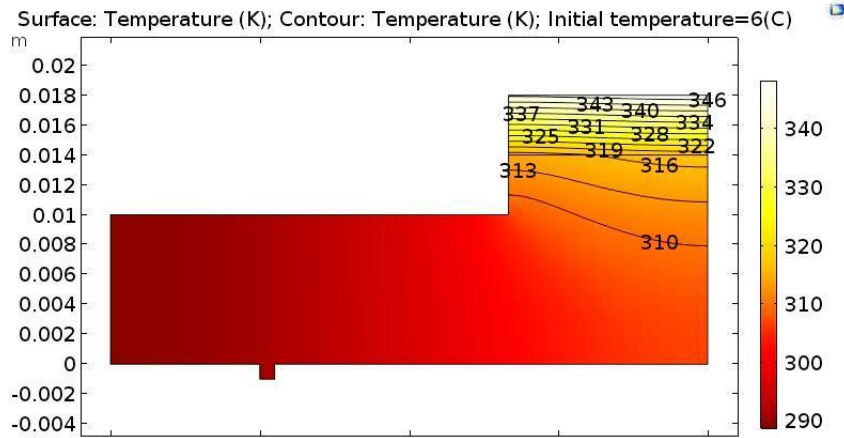
(a)
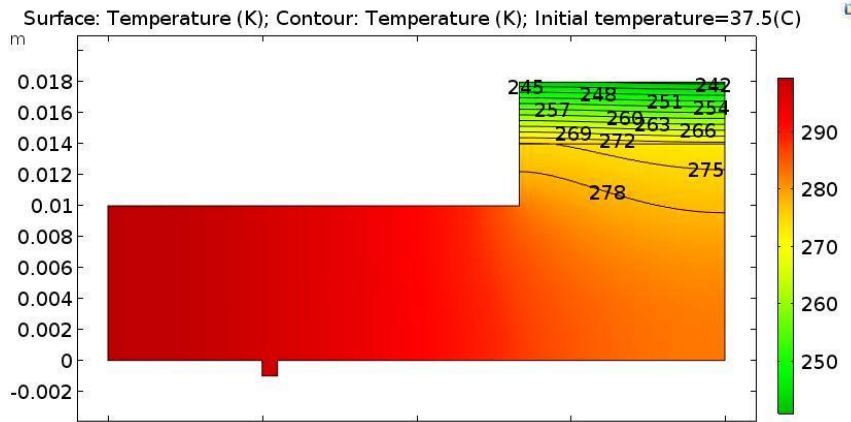
(b)

Figure 3-17 Temperature profile in FEM model: (a) heating mode, (b) cooling mode

44
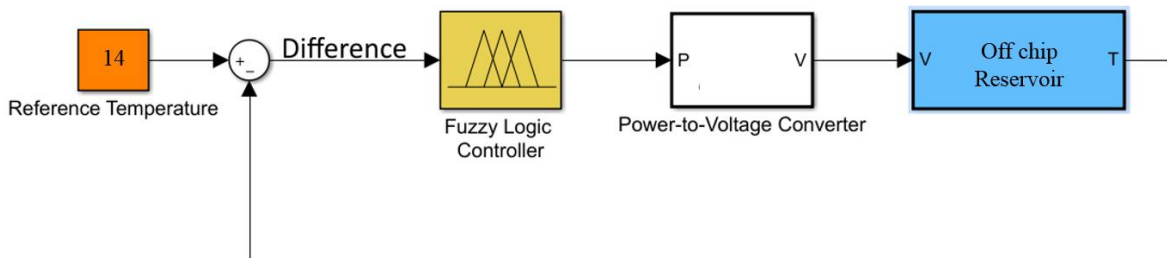
Figure 3-18 The schematic of the close-loop system with the proposed fuzzy controller.

In order to maintain the sample fluid temperature in the disposable main tank at a certain temperature (e.g., 14℃ in our experiments), our proposed fuzzy control logic, which is detailed in Section 3.4, was utilized in our experiments. Figure 3-18 shows the schematic of the close-loop testbench with our proposed fuzzy logic controller and micro-dispenser prototype. The reference temperature of the fuzzy logic controller was set as 14℃. We implemented the proposed fuzzy logic controller and power-to-voltage converter with MATLAB Simulink. The output voltage from the power-to-voltage converter module was connected to our micro-dispenser prototype to power up the thermoelectric Peltier unit. Figure 3-19 shows the average temperature of the micro-dispenser prototype when a fuzzy control controller is utilized. This shows the excellent performance of our proposed micro-dispenser heating and control system, which can reach 14℃ smoothly (± 0.07℃) from the initial temperature (6℃).

To demonstrate the efficacy of our proposed fuzzy logic controller, we also implemented two other controllers for the comparison purpose with the same testbench depicted in Figure 3-19. State machine controllers and proportional–integral–derivative (PID) controllers are widely used for the systems that can hardly be mathematically modeled. The state machine represents a reactive system that contains a finite number of states [56]. The state machine controller changes states based on the categorized conditions of the target system. In our implementation there are two states: "0" when the controller is not active, and "1" when the controller is active. The controller would decide when to switch between these two states based on a function called "Is System Cool", which compares the sensed temperature from the DS18B20 temperature sensor with the reference temperature (14°C). On the other side, the PID controller calculates the error between the reference temperature and the actually sampled temperature of the target system. It can decrease the error by

using proportional, integral, and derivative operators. Figure 3-19 shows the comparison among the state machine, PID, and our proposed fuzzy logic controllers. As can be seen from this figure, the output from the fuzzy logic controller has the least oscillation around the reference temperature since the fuzzy output can continuously change between 0 and 1. In contrast, the state machine controller and classical PID controller suffer large fluctuation ($\pm 0.17°C$ and $\pm 0.4°C$, respectively) around the reference temperature of 14°C. This is mainly due to the simple control logic used in these controllers.
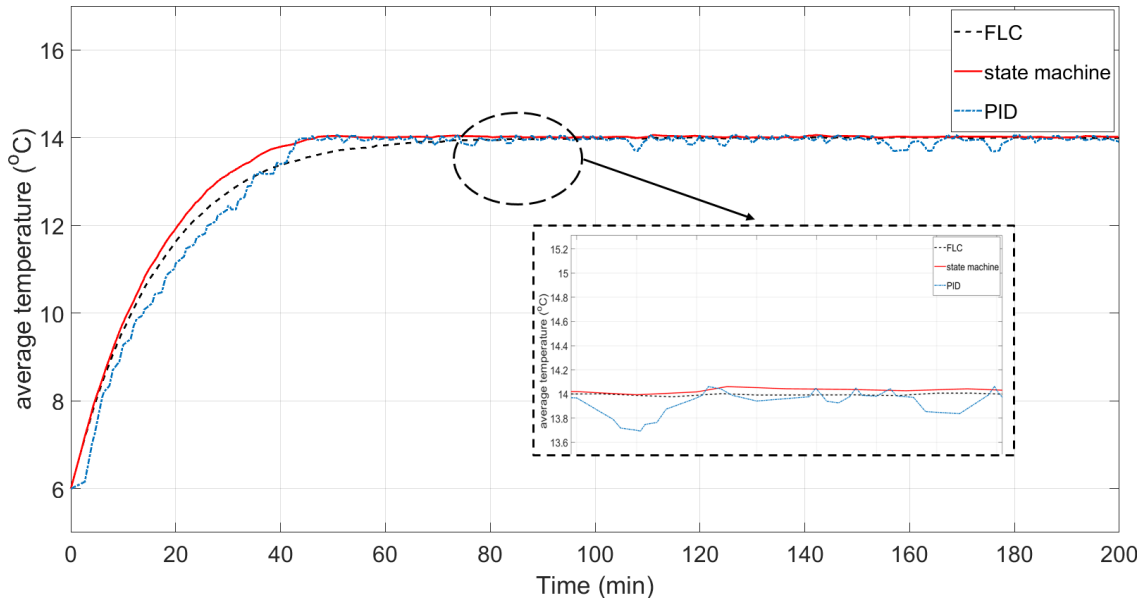
Figure 3-19 Comparison of the average temperature versus time among the state machine, PID, and fuzzy logic controllers.

Finally, to measure the average volume of the dispensed droplets, ten droplets were sequentially dispensed by our micro-dispenser prototype. The volume of each dispensed droplet was computed after the mass measurement by using an ultra-precise scale (APX-200.3). The average droplet volume is equal to $21.7\ \mu L$, while the standard deviation is $91\ nL$. Thus, we can see that our proposed design methodology can offer a highly precise micro-dispenser with only

0.4% error at the nominal droplet volume of 21.7 μL. In comparison, the complex automated syringe pump developed by Ding *et al.* reported its accuracy of 100 nL [19]. That is to say, the accuracy of our proposed micro-dispenser is 9% higher than their work in addition to the simplicity, low-cost, and disposability advantages of our design. A full comparison among the previously published works and our proposed device is listed in Table 3-4.

Table 3-4 Comparison among the previously published works and our proposed device

Device	Low cost	Portability	Disposability	Temperature controllability	Accuracy
[9]	✓	✓	✓	✗	✗
[10]	✓	✓	✓	✗	✗
[11]	✗	✗	✗	✗	✓
[12]	✗	✗	✗	✗	✓
[24]	✗	✗	✗	✗	✓
[25]	✓	✓	✓	✗	✗
Our device	✓	✓	✓	✓	✓

3.6.   Summary

In this chapter, we presented a complete design methodology for cost-effective portable micro-dispensers, which can connect off-chip reservoirs in the continuous microfluidic domain to on-chip reservoirs in the digital microfluidic domain for accurate droplet transportation. Our proposed micro-dispenser consists of two separate parts: mainframe (having no direct contact with sample fluids) and disposable main tank, which can effectively avoid contamination of sample fluids between two consecutive operations. The temperature of the fluid stored in the disposable main tank can be regulated with a fuzzy logic controller by using a thermoelectric device for heating/cooling purposes. Moreover, we developed a complete analytic method to design the key off-chip reservoir parameters, including the critical displacement of the elastic diaphragm layer and the diameter of the outlet hole of the disposable main tank. We validated our proposed design

methodology and demonstrated its high efficacy by using FEM simulations and prototype measurements.

Chapter 4   Design and Optimization of

Piezoelectric Actuator for a Valveless Micropump

4.1.   Introduction

In the conventional mechanical micropumps, the motion from one component (such as gear or diaphragm) produces pressure difference, which is needed to move the fluid. In this chapter, we propose a new method to use multi-sheet piezoelectric material (PZT) as an actuator for a valveless micropump. Instead of one single PZT sheet, multiple PZT sheets are utilized to produce larger movement force. We have derived analytic equations for expressing the natural frequency of the actuator. The FEM simulations are utilized to verify the analytic equations. Thanks to their high accuracy, we have used the derived analytic equations as fitness functions of genetic algorithm (GA) for the optimization purpose. Our experimental results show that the GA is capable of optimizing multiple physical parameters of the piezoelectric actuator. A typical valveless micropump with the proposed multi-sheet PZT actuator is verified by using the COMSOL Multiphysics software. The flow rate of this configuration is compared with a single-sheet PZT actuator in order to demonstrate the effect of the optimized PZT actuator on the application of the valveless micropumps.

This chapter is organized as follows. In Section 4.2, the governing equations of the optimized PZT layer with a bonding layer will be presented and then the natural frequency will be calculated. In Section 4.3 the optimization algorithm will be discussed, while the FEM simulations will be presented to verify the analytic solutions in Section 4.4. We use COMSOL Multiphysics software to help design a typical valveless micropump with a single-PZT-sheet actuator and a double-PZT-sheet actuator. A high AC voltage with the natural frequency is applied to the micropump to investigate the effect of the PZT-based actuators on the output flow rate. Finally, we will make a summary in Section 4.5.

4.2.　Analytical Modeling

The primary purpose of an optimized piezoelectric-layer actuator is to provide large bending displacement in the transverse direction. As illustrated in Figure 4-1, a piezoelectric (e.g., PZT) layer, which might be physically implemented by multiple PZT sheets, is glued with the diaphragm layer. These two layers are assumed to connect each other by a massless and linear epoxy bonding layer. The radius of the PZT layer and bonding layer is r_o, while their thicknesses are t_p and t_b, respectively. In this model, since the thickness of the electrodes is less than 0.5 μm, their effect on the deflection of the PZT layer will be ignored [57].
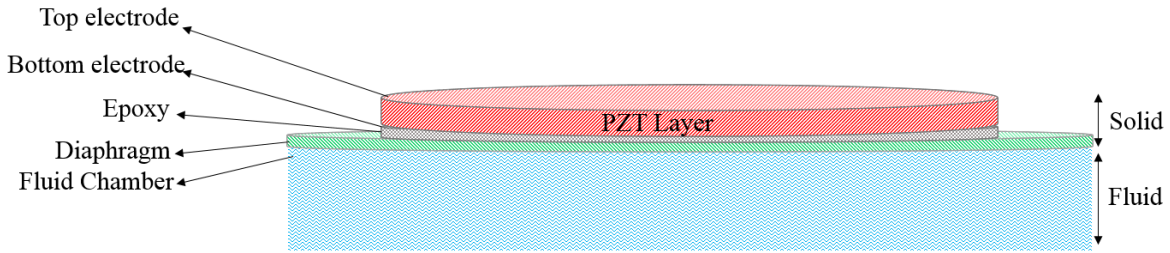
Figure 4-1 Schematic view of a typical piezoelectric actuator.

To calculate the natural frequency, the dynamic behavior of the system has to be studied. By utilizing LaGrange method, we can derive the axisymmetric governing equations as follows [1]:

$$T_1 \cdot \left(\frac{\partial^2 w_1(r,t)}{\partial r^2} + \frac{1}{r} \cdot \frac{\partial w_1(r,t)}{\partial r} \right) = m_1 \cdot \frac{\partial^2 w_1(r,t)}{\partial t^2} + k \cdot \left(w_1(r,t) - w_2(r,t) \right) , \tag{1-1}$$

$$T_2 \cdot \left(\frac{\partial^2 w_2(r,t)}{\partial r^2} + \frac{1}{r} \cdot \frac{\partial w_2(r,t)}{\partial r} \right) = m_2 \cdot \frac{\partial^2 w_2(r,t)}{\partial t^2} - k \cdot \left(w_1(r,t) - w_2(r,t) \right) , \tag{1-2}$$

where T_1 and T_2 are the applied tension on the piezoelectric and diaphragm layer respectively, w_1 and w_2 are the displacement of the piezoelectric and diaphragm layer respectively, k is the stiffness coefficient of the epoxy layer, m_1 and m_2 are the mass per unit area of the piezoelectric and diaphragm layer respectively. The PZT layer, which may physically include multiple PZT

51

sheets, is clamped along the edge such that there is no displacement. As a result, the boundary condition equations can be written as follows:

$$w_i(r_o, t) = 0, w_i(0, t) \neq \infty. \text{ (i=1 or 2)} . \tag{2}$$

Moreover, the PZT layer has no initial velocity:

$$w_i(r, 0) = w_0, \frac{\partial w_i}{\partial t}(r, 0) = 0 . \tag{3}$$

By applying the separation variation method, w_1 and w_2 can be rewritten as follows:

$$w_1(r, t) = R_1(r) \cdot Z(t) , \tag{4-1}$$

$$w_2(r, t) = R_2(r) \cdot Z(t) , \tag{4-2}$$

$$Z(t) \cdot T_1 \cdot \left(\frac{\partial^2 R_1(r)}{\partial r^2} + \frac{1}{r} \cdot \frac{\partial R_1(r)}{\partial r} \right) = m_1 \cdot R_1(r) \cdot \frac{\partial^2 Z(t)}{\partial t^2} + k \cdot \left(R_1(r) \cdot Z(t) - R_2(r) \cdot \right. \tag{5-1}$$

$$\left. Z(t) \right) ,$$

$$Z(t) \cdot T_2 \cdot \left(\frac{\partial^2 R_2(r)}{\partial r^2} + \frac{1}{r} \cdot \frac{\partial R_2(r)}{\partial r} \right) = m_2 \cdot R_2(r) \cdot \frac{\partial^2 Z(t)}{\partial t^2} - k \cdot \left(R_1(r) \cdot Z(t) - R_2(r) \cdot \right. \tag{5-2}$$

$$\left. Z(t) \right) .$$

Let's assume $Z(t) = Z_0 . e^{-i\omega t}$, then:

$$Z_0 \cdot e^{-i\omega t} \cdot T_1 \cdot \left(\frac{\partial^2 R_1(r)}{\partial r^2} + \frac{1}{r} \cdot \frac{\partial R_1(r)}{\partial r} \right) = m_1 \cdot R_1(r) Z_0 e^{-i\omega t}(-\omega^2) +$$

$$k \left(R_1(r) Z_0 e^{-i\omega t} - R_2(r) \cdot Z_0 \cdot e^{-i\omega t} \right) , \tag{6-1}$$

$$Z_0 \cdot e^{-i\omega t} \cdot T_2 \cdot \left(\frac{\partial^2 R_2(r)}{\partial r^2} + \frac{1}{r} \cdot \frac{\partial R_2(r)}{\partial r} \right) = m_2 \cdot R_2(r) \cdot Z_0 e^{-i\omega t}(-\omega^2) - k \cdot$$

$$\left(R_1(r) \cdot Z_0 \cdot e^{-i\omega t} - R_2(r) \cdot Z_0 \cdot e^{-i\omega t} \right) . \tag{6-2}$$

These equations can be rewritten as:

$$Z_0 \cdot e^{-i\omega t} T_1 \cdot \left(\frac{\partial^2 R_1(r)}{\partial r^2} + \frac{1}{r} \frac{\partial R_1(r)}{\partial r} \right) = m_1 \cdot R_1(r) \cdot Z_0 \cdot e^{-i\omega t} \cdot (-\omega^2) + k \cdot$$

$$Z_0 \cdot e^{-i\omega t} \cdot \left(R_1(r) - R_2(r) \right) \;, \tag{7-1}$$

$$Z_0 \cdot e^{-i\omega t} \cdot T_2 \cdot \left(\frac{\partial^2 R_2(r)}{\partial r^2} + \frac{1}{r} \frac{\partial R_2(r)}{\partial r} \right) = m_2 \cdot R_2(r) \cdot Z_0 \cdot e^{-i\omega t} \cdot (-\omega^2) -$$

$$k \cdot Z_0 \cdot e^{-i\omega t} \cdot \left(R_1(r) - R_2(r) \right) \;. \tag{7-2}$$

With simplification:

$$T_1 \cdot \left(\frac{\partial^2 R_1(r)}{\partial r^2} + \frac{1}{r} \cdot \frac{\partial R_1(r)}{\partial r} \right) = -m_1 \cdot \omega^2 \cdot R_1(r) + k \cdot \left(R_1(r) - R_2(r) \right) \;, \tag{8-1}$$

$$T_2 \cdot \left(\frac{\partial^2 R_2(r)}{\partial r^2} + \frac{1}{r} \cdot \frac{\partial R_2(r)}{\partial r} \right) = -m_2 \cdot \omega^2 \cdot R_2(r) - k \cdot \left(R_1(r) - R_2(r) \right) \;. \tag{8-2}$$

Let's define $\nabla R_i = \frac{\partial^2 R_i(r)}{\partial r^2} + \frac{1}{r} \cdot \frac{\partial R_i(r)}{\partial r}$. By putting ∇R_i into the equations, the following equations

will be obtained:

$$T_1 \cdot \nabla R_1 + (m_1 \cdot \omega^2 - k) \cdot R_1(r) + k \cdot R_2(r) = 0 \;, \tag{9-1}$$

$$T_2 \cdot \nabla R_2 + (m_2 \cdot \omega^2 - k) \cdot R_2(r) + k \cdot R_1(r) = 0 \;. \tag{9-2}$$

By eliminating R_2 from these equations, the following equation can be obtained:

$$(\nabla + C_1^2) \cdot (\nabla + C_2^2) \cdot R_1 = 0 \;, \tag{10}$$

where C_1 and C_2 are equal to:

$$C_{1,2}^2 = \frac{1}{T_1 \cdot T_2} \left((m_2 \cdot T_1 + m_1 \cdot T_2) \cdot \omega^2 - (T_1 + T_2) \cdot k \right) \pm (2 \cdot T_1 \cdot T_2 \cdot k^2 +$$

$$T_2^2 \cdot m_1^2 \cdot \omega^4 + T_1^2 \cdot m_2^2 \cdot \omega^4 + T_2^2 \cdot k^2 + T_1^2 \cdot k^2 - 2 \cdot m_2 \cdot \omega^2 \cdot T_1^2 \cdot k + 2 \cdot m_1 \cdot \tag{11}$$

$$T_2^2 \cdot \omega^2 \cdot k - 2 \cdot m_2 \cdot m_1 \cdot T_1 \cdot T_2 \cdot \omega^4 + 2 \cdot m_1 \cdot T_1 \cdot T_2 \cdot k \cdot \omega^2)^{\frac{1}{2}}) \;.$$

The solution of this equation can be represented as the sum of the roots from the Bessel function as follows:

$$R_{1i} = a_i \cdot J_o(C_i \cdot r) + b_i \cdot Y_o(C_i \cdot r) \ , \tag{12}$$

$$J_o(C_i \cdot r_o) = 0 \ \text{ or } J_o(\delta) = 0 \ , \tag{13}$$

where δ is the root of the Bessel function. Now by solving this simple algebraic equation, natural frequencies ω of the system can be calculated. We can see that this analytic model is very valuable, since the designers can use it to estimate the natural frequency of a new PZT layer quickly for different dimensions without any expensive FEM simulation. To calculate the mode shape function, (12) must be solved. The general solution can be achieved as follows:

$$R_1 = \sum_{i=1}^{2} (a_i \cdot J_0(C_i \cdot r) + b_i \cdot Y_0(C_i \cdot r)) \ , \tag{14}$$

$$R_2 = \sum_{i=1}^{2} d_i \cdot (a_i \cdot J_0(C_i \cdot r) + b_i \cdot Y_0(C_i \cdot r)) \ , \tag{15}$$

where d_i is:

$$d_i = \frac{1}{k} \cdot (m_1 \cdot \omega^2 + T_1 \cdot C_i^2 + k) \ . \tag{16}$$

By applying the first boundry condition, since $R_{1i}(0) \neq \infty$, b_i should be equal to zero. In addition, by applying the second boundry condition $R_{1_i}(r_o, t) = 0$, we can get the following equations:

$$\begin{cases} a_1 \cdot J_0(C_1 \cdot r_0) + a_2 \cdot J_0(C_2 \cdot r_0) = 0 \\ d_1 \cdot a_1 \cdot J_0(C_1 \cdot r_0) + d_2 \cdot a_2 \cdot J_0(C_2 \cdot r_0) = 0 \end{cases} , \tag{17}$$

or in matrix form:

$$\begin{bmatrix} J_0(C_1 \cdot r_0) & J_0(C_2 \cdot r_0) \\ d_1 \cdot J_0(C_1 \cdot r_0) & d_2 \cdot J_0(C_2 \cdot r_0) \end{bmatrix} \begin{bmatrix} a_1 \\ a_2 \end{bmatrix} = \begin{bmatrix} 0 \\ 0 \end{bmatrix} \quad , \tag{18}$$

In order to have a non-zero solution in (18), the following condition must be satisfied:

$$(d_1 - d_2) \cdot J_0(C_1 \cdot r_0) \cdot J_0(C_2 \cdot r_0) = 0 \quad . \tag{19}$$

In the end, the characteristic equation will be obtained as:

$$J_o(C_n \cdot r_o) = 0 \ \text{ or } J_o(\delta_n) = 0 \quad , \tag{20}$$

where δ_n is the root of the Bessel function, and n denotes the n-th root of the Bessel function. Now by solving this simple algebraic equation, natural frequencies ω of the system can be calculated. In addition, the mode shape of the piezoelectric layer and the diphragm layer can be expressed respectively as follows:

$$R_1(r) = a_{1n} \cdot J_o(C_n \cdot r) \quad , \tag{21-1}$$

$$R_2(r) = d_i \cdot a_{1n} \cdot J_o(C_n \cdot r) \quad , \tag{21-2}$$

where a_{1n} is equal to:

$$a_{1n}^2 = \frac{1}{\pi \cdot \rho \cdot r_1^2 \cdot J_1^2(C_n \cdot r_1)} \quad . \tag{21-3}$$

4.3.   Optimization Algoritm

The Genetic Algorithm (GA) is an evolutionary computing algorithm for optimizing sophisticated problems by mimicking biological evolution [40]. The GA starts its mechanism by generating some stochastic numbers for variables to minimize certain defined fitness functions.

The GA solutions are normally coded in binary string structure. During the computation, three different operators can be typically applied to the set of solutions to provide new evolutionary population. The flow-chart of the GA mechanism is shown in Figure 4-2.
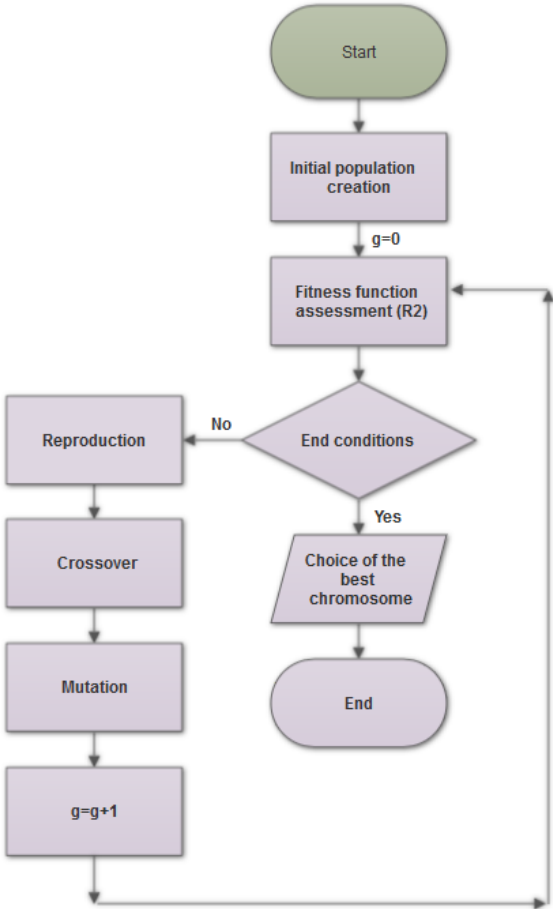
Figure 4-2 Working mechanism flowchart of the GA optimization algorithm.

As shown in Figure 4-2, the GA optimization starts with the initialization block, where the variables are coded in the form of fixed length binary strings. Each variable can be randomly selected with equal probability. Usually the first operator that performs on a population is the reproduction, which strives to find appropriate individuals in a population and interpolate them into a mating pool. A number of methods for individual selection have been proposed in the literature, although the main idea of this operation is to choose, duplicate, and insert certain

56

preferable individuals from the current population into the pool. The next operator within GA is the crossover, where typically two individuals are selected from the mating pool and a certain quota of these individuals are exchanged in between. In other words, the recombination between these pairs produces new individuals, called *offspring*. Finally, the mutation operator is performed to change one bit from 1 to 0 or vice versa. This process is also random with a very low probability (called *mutation rate*) on the entire population.

All the three operators are performed on the entire population in one GA generation. Thus, the search and optimization aspect of GA is mainly provided by the crossover and mutation operators. The multi-dimensional search capability offered by GA can effectively prevent it from being entrapped by local optima [40]. Therefore, a significant feature of GA in comparison with the conventional optimization approaches is its advantageous access to the global optimum. In this study, our proposed GA-based optimization method is performed to identify the best physical aspects of the piezoelectric layer to increase the displacement of the diaphragm. The coverage of the electrodes is defined identical to the size of the piezoelectric film. In the following section, the capability of the GA-based optimization methodology will be studied.

4.4.   Results and Discussion

Since the analytic equations, which show the relationship among the thickness of the piezoelectric layer, the thickness of the diaphragm, the radius of the layers, and the maximum deflection of the layers as discussed in Section 4.2, are able to accurately estimate the thicknesses of the piezoelectric and diaphragm layers, we have deployed them (mainly (21-2)) as a fitness function of our GA optimization algorithm. We may include multiple physical variables as

optimizable parameters. But in this study, we treat the piezoelectric thickness (h_p) as the only optimizable parameter.

We have implemented the GA-based optimization method in MATLAB by using its genetic algorithm tool box (Version 2017) in order to enhance the vertical displacement magnitude of the layers. The applied fitness function and constraints of the optimization are defined by (22):

Maximize: $\{R_2\}$,

Subject to : design rules of the optimizable parameters (22)

For the optimizable physical parameter (i.e., h_p), the upper and lower bounds are defined as per the design rule constraints as [1μ, $1000\ \mu$], respectively. According to the listed data in Table 4-1, the optimized thickness for the piezoelectric layer is 92.95 μm. In other word, based on the other factors and parameters, such a thickness of the piezoelectric layer can provide the maximum displacement performance. The required thickness can be achieved by multiple cost-effective over-the-shelf commercial piezoelectric sheets instead of the expensive customized one-layer piezoelectric material. For our case study, we have deployed two PZT sheets with the same diameter and thickness (i.e., 42 μm). The material properties within the system are shown in Table 4-2.

Table 4-1 The parameters of the system.

	Optimized diaphragm layer thickness	Optimized piezoelectric layer thickness	Radius	Input voltage
Value	117 μm	92.95 μm	7.5 mm	100 V

Table 4-2 Material properties within the system.

Mechanical property	Bonding layer (Epoxy Resin)	PZT (Lead Zirconate Titanate)
Mass density	$2000\ (Kg/m^3)$	$7500\ (Kg/m^3)$
Elastic modulus	$5.17\ (GPa)$	$9.5\ (GPa)$
Poisson's ratio	0.31	0.30

In order to calculate the natural frequency by using the analytical method, (20) must be solved. By solving this simple algebraic Bessel function, natural frequencies ω of the system can be calculated. Figure 4-3 show the Bessel function and its roots, which are equal to the natural frequency of the systme. In addition, by solving (21), the mode shapes of the system will be calculated. Figure 4-4 shows the first mode shape of the diaphragm layer by the analytical model.
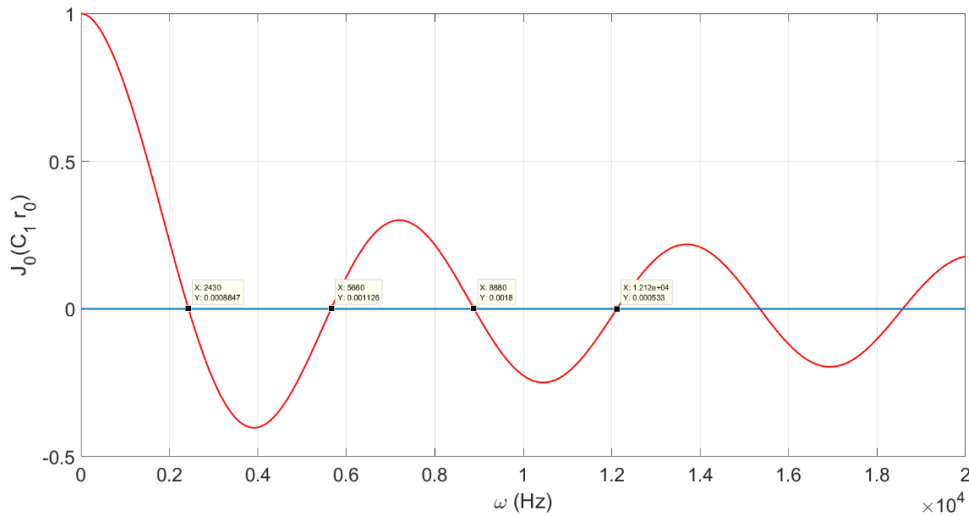
Figure 4-3 The solution of the characteristic equation.
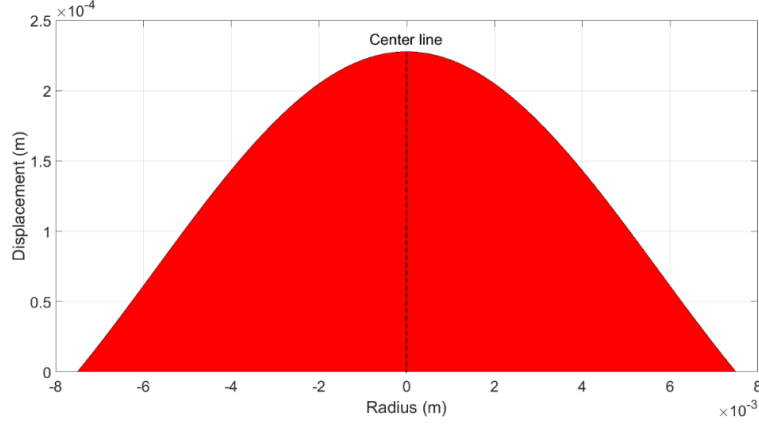
Figure 4-4 The first mode shape of the diaphragm layer $(R_2(r))$ calculated by the analytical

method.

To validate our methodology, we have run two groups of FEM simulations. In the first group, one piezoelectric layer with the optimized thickness was simulated in COMSOL Multiphysics (Version 5.3). Figure 4-5 shows the natural frequency and mode shape of this simulation. In the other groups of simulations, the equivalent thickness was managed by attaching multiple piezoelectric sheets together along with the epoxy bonding layer. The results of the simulations are shown in Figure 4-6. To better compare the performance, all the conditions (i.e., radius, initial conditions, and boundary conditions) are the same in both groups of simulations. Table 4-3 shows this comparison. The absolute percentage error (APD) is calculated by the following equation:

$$\epsilon_i = 100\% \cdot \left| \frac{(\omega_{F_i} - \omega_{A_i})}{\omega_{F_i}} \right| , \tag{23}$$

where ω_{F_i} is the natural frequencies calculated by the FEM simulation, and ω_{opt_i} is the natural frequencies in the optimized cases also calculated by the FEM simulation.

60

(a)

(b)

(c)
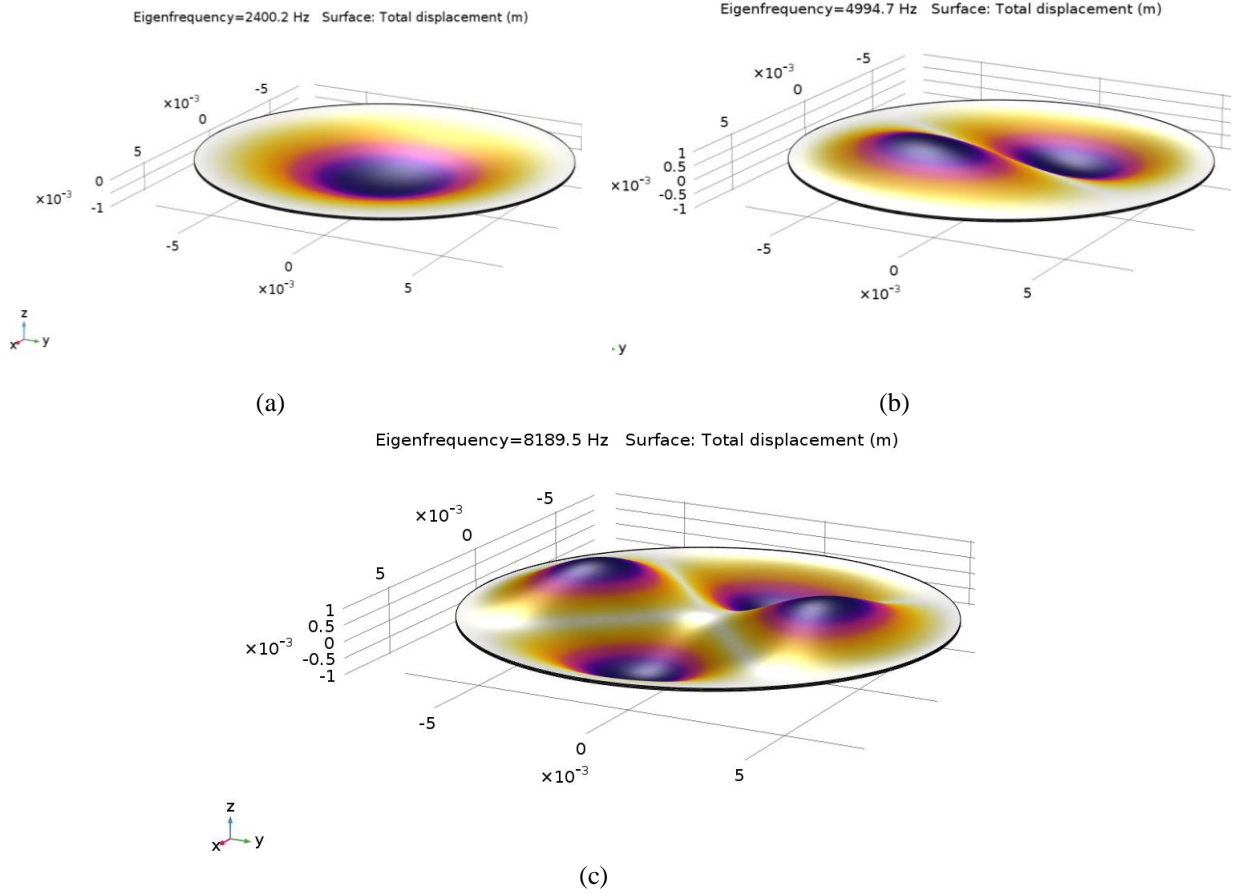
Figure 4-5 The natural frequencies of the optimized PZT layer in Comsol Multiphysics, a) The first

mode shape, b) The second mode shape, c) The third mode shape.

(a)

(b)

Eigenfrequency=8630.4 Hz   Surface: Total displacement (m)

(c)
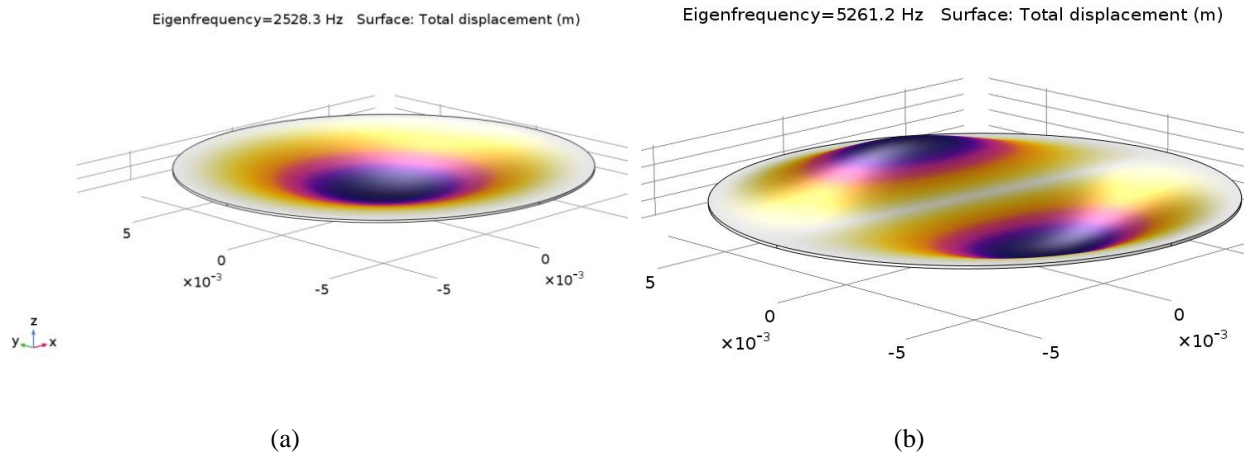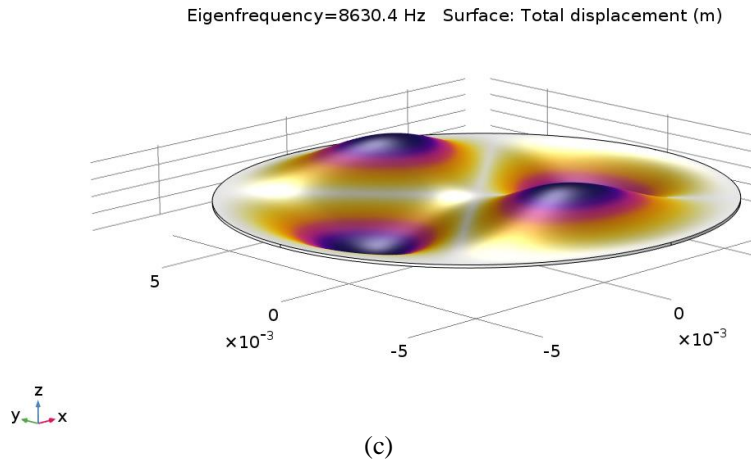
Figure 4-6 The natural frequencies of the multiple PZT sheets along with the epoxy bonding layer in Comsol

Multiphysics, a) The first mode shape, b) The second mode shape, c) The third mode shape.

Table 4-3 The first, second, and third natural frequencies.

Resonant frequency	Multi-sheet Model (Hz)	Optimized Model (Hz)	Absolute percentage Error (APD)
1	2528.3	2400.2	5.07
2	5261.2	4994.7	5.33
3	8630.4	8189.5	5.32

Table 4-4 The first, second, and third natural frequency.

Resonant frequency	Analytical optimized model (Hz)	FEM optimized model (Hz)	Absolute percentage Error (APD)
1	2430	2400.2	1.26
2	5620	4994.7	11.1
3	8890	8189.5	7.87

As listed in Table 4-4, the results show the accuracy of our proposed analytic model. We can

see that this analytic model is very valuable, since the designers can use it to estimate the natural

frequencies of a new system configuration with different geometric dimensions very efficiently and then realize it with the cost-effective over-the-shelf commercial PZT sheets without any expensive FEM simulations. Moreover, the transverse vibration of the optimized PZT layer can be turned into a time-dependent vibration when the input voltage signal changes as a function of time. Thus, the designers can determine the best input signal, which can maximize the efficiency of the system. In order to reach this goal, after calculating the natural frequencies, the first natural frequency will be chosen to apply to the system. A high voltage signal with the same frequency ω_1 will be applied to the system and the maximum deflection will be measured and compared between the FEM simulation and experimental setup.

To verify the accuracy of the proposed model, we have built up an experimental setup. A high voltage signal (i.e., $200\sin(\omega_1 t)$) with the same frequency ω_1 was applied to the system, while the maximum deflection was measured from both the FEM simulation and the experimental setup. The system response is shown in Figure 4-7. The maximum stress, which occurs at the edge, is shown as a function of time in this figure. This figure also reveals that the maximum deflection of the system with respect to that excitation signal is equal to 121 μm as indicated by the reference scale located on the right.

63
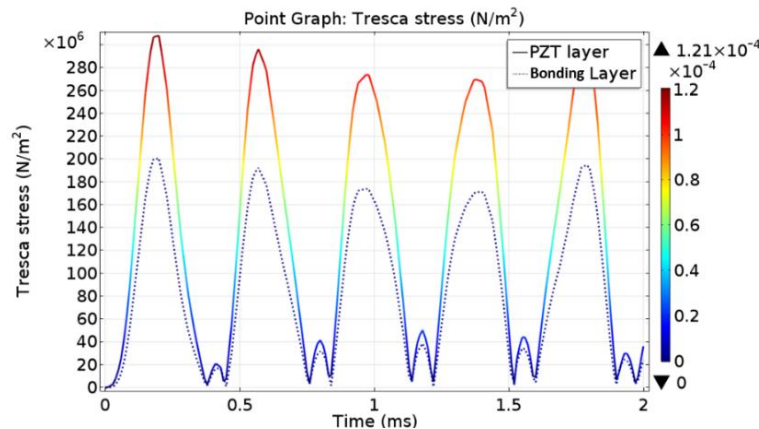
Figure 4-7 Tresca stress at the boundary and displacement profile

The experimental setup, as shown in Figure 4-8, includes a fixture, a high precision laser measurement sensor (LK-H022, resolution of 0.02 μm), a signal generator, a high-precision high voltage power amplifier (TEGAM-2350), and a data acquisition system. In order to verify the FEM simulation with reference to the experimental measurement results, an excitation signal was applied to the system. Figure 4-9 shows the center deflection of the double PZT sheets. As can be seen in this figure, the maximum value of the deflection is equal to 117 μm, which is very close to the FEM result with the error of 3.3%.
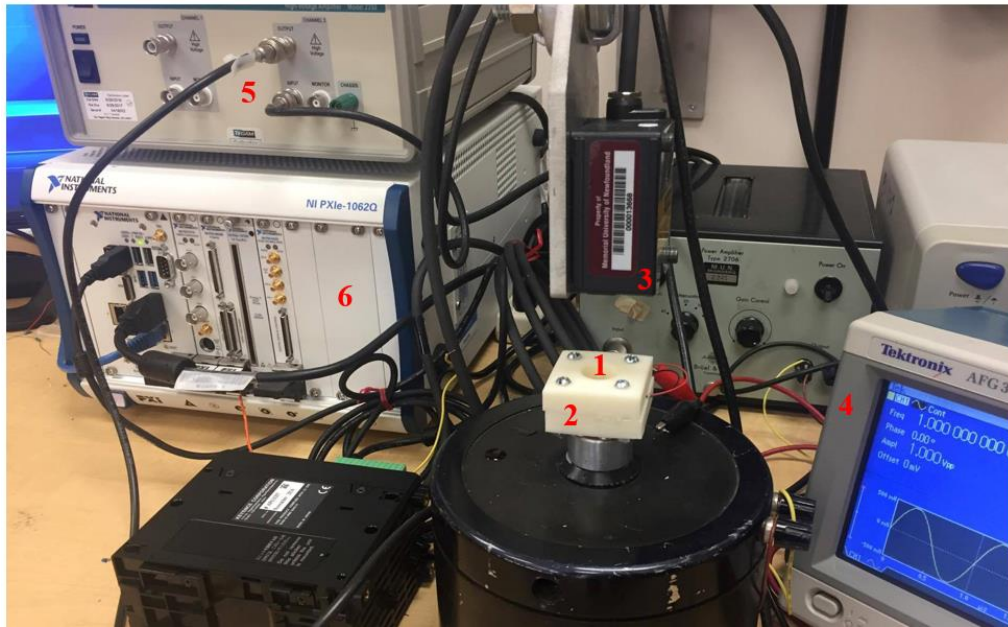
Figure 4-8 1) Double PZT sheets, 2) Fixture, 3) a high precision laser measurement sensor (LK-H022, resolution of 0.02 μm), 4) Signal generator, 5) Precision power amplifier high voltage (TEGAM-2350), 6) Data acquisition system.
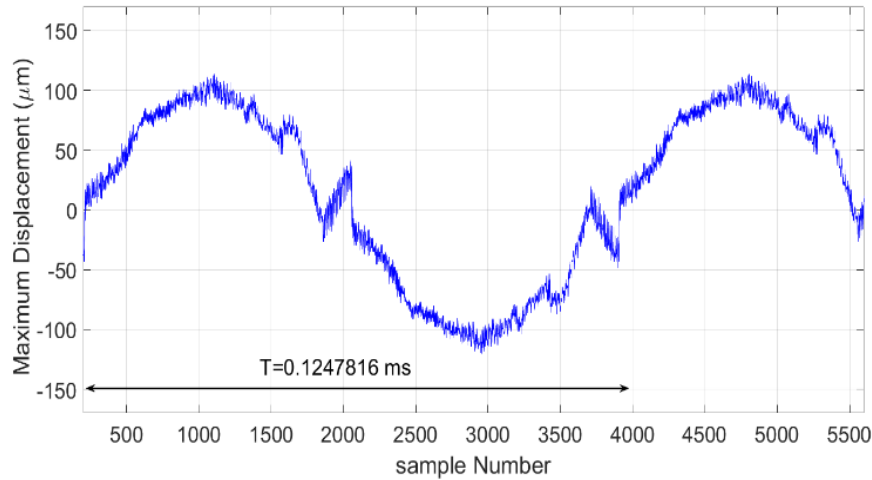
Figure 4-9 The center displacement response of the system under excitation signal of $200\sin(\omega_1 t)$.

In this section, the double-PZT-sheet actuator was modelled onto a valveless micropump to explore the effect of this proposed actuator on the flow rate of the valveless micropump. A typical configuration of the valveless micropump with the double-PZT-sheet actuator is modelled in COMSOL Multiphysics as shown in Figure 4-10. In such a valveless micropump, there is no moving part. It works as per the geometric properties of nozzle and diffuser. The purpose of this section is not focused on the principle of this type of micropumps. More details about the micropump design can be found in the literature [58-59]. Figure 4-10(a) shows the micropump chamber in the suction mode, while Figure 4-10(b) shows the chamber of micropump in the pump mode. In those figures, the first, second, and third color bars show the velocity, total displacement, and norm of the electrical field, respectively.
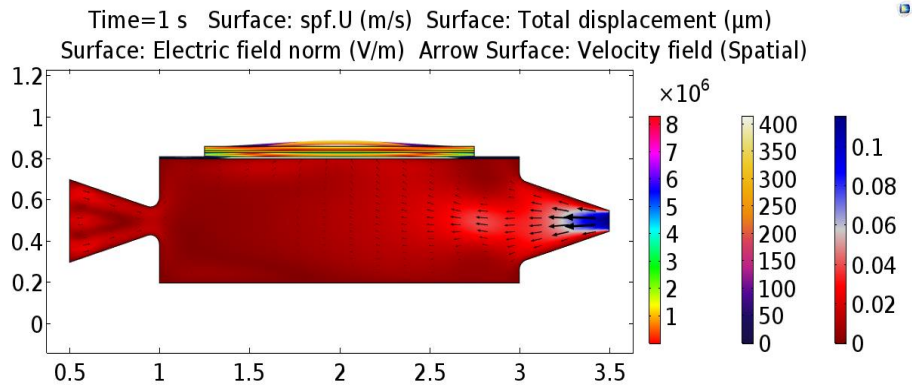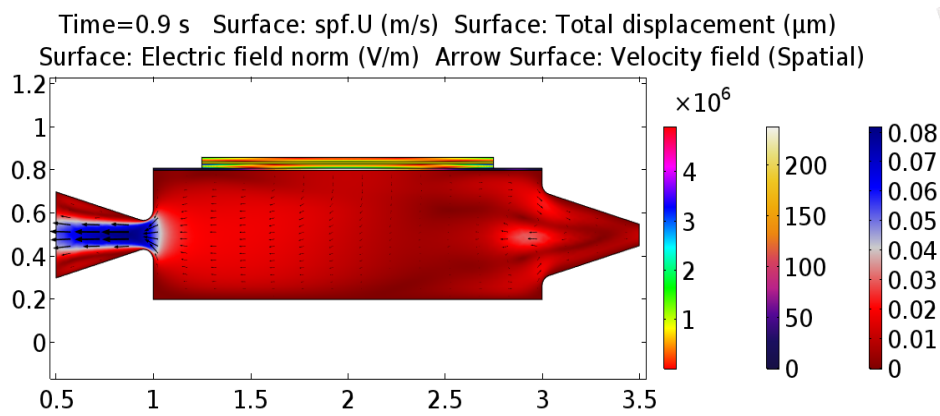
Figure 4-10 The FEM modeling of the valveless micropump with the double-PZT-sheet

actuator a) The suction mode, b) The pump mode.

In order to investigate the effect of the double-PZT-sheet actuator on the system, the flow

rate is calculated by FEM simulations. Figure 4-11(a) shows the flow rate of the valveless

micropump with a regular single-PZT-sheet actuator. As can be seen from this figure, the

maximum flow rate reaches up to $1.47 * 10^{-5} \, m^2/s$. On the other hand, Figure 4-11(b)

shows the flow rate of the same valveless micropump in the same condition, but with the

double-PZT-sheet actuator connected by a bonding layer. As can be seen from this figure, the

maximum flow rate would reach $12.1 * 10^{-5} \, m^2/s$, which is suitable for pumping biological

samples, such as blood. In other words, by utilizing our proposed double-PZT-sheet actuator, the flow rate of the valveless micropump can be increased up to 8.23 times.
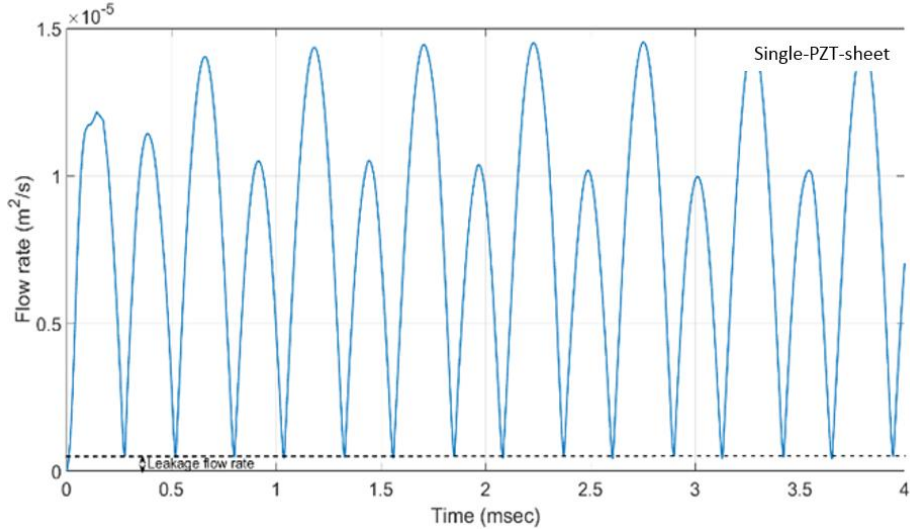
(a)
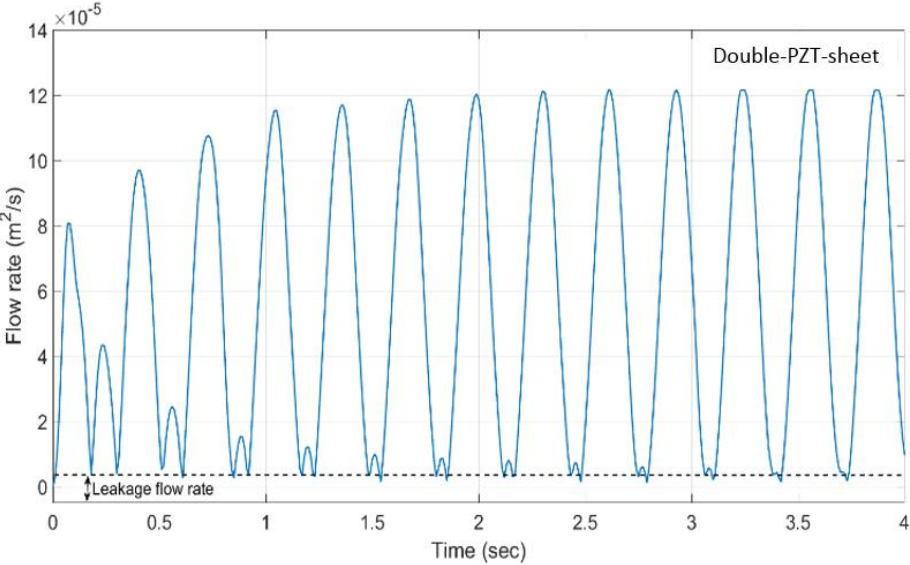
(b)

Figure 4-11 Output flow rates of the valveless micropump a) with a single-PZT-sheet actuator, b) with a double-PZT-sheet actuator.

4.5.   Summary

In this chapter, we designed and optimized a PZT layer as an actuator for the valveless micropump. The analytic analysis of the PZT-layer-based actuator was first conducted and then verified by using FEM simulations. The comparison between the analytic computation and COMSOL Multiphysics simulation reveals the high accuracy of our deducted analytic solution, whose error is less than 1%. This is valuable since the designers can estimate the natural frequencies and mode shapes of a new configuration with different dimensions efficiently by using our proposed analytic solution without depending on any expensive FEM simulations. Moreover, the experimental setup was established to measure the maximum displacement for a comparison with the FEM simulation. The result shows that the difference between FEM simulation and our experimental measurement is less than 4%. Furthermore, the proposed actuator was applied to a typical valveless micropump to evaluate the functionality of the actuator. The comparison between a regular valveless micropump with a single-PZT-sheet actuator and the same valveless micropump with a double-PZT-sheet actuator reveals that the flow rate could be increased up to 8.23 times.

Chapter 5　Design and Optimization of Cost-Effective Coldproof Portable Enclosures for Polar Environment

5.1.   Introduction

Based on the International Electrotechnical Commission (IEC) standards, the electronic devices in the industrial class (e.g., integrated circuits (ICs) or batteries) can only operate at the ambient temperature between -40°C and 85°C. For the human-involved regions in Alaska, Northern Canada, and Antarctica, extreme cold condition as low as -55°C might affect sensing electronic devices utilized in the scientific or industrial applications. In this thesis, we propose a design and optimization methodology for the self-heating portable enclosures, which can warm up the inner space from -55°C for encasing the low-cost industrial-class electronic devices instead of expensive military-class ones to work reliably within their allowed operating temperature limit. By considering various factors (including hardness, thermal conductivity, cost, and lifetime), we determine to mainly use polycarbonate as the manufacturing material of the enclosure. Among the other options, ceramic thermal resistors are selected as the heating elements inside the enclosure. The placement of the thermal resistors is studied with the aid of thermal modeling for the single heating device by using the curve fitting technique to achieve uniform temperature distribution within the enclosure. To maintain the inner temperature above -40°C but with the least power consumption from the thermal resistors, we have developed a control system based on the fuzzy logic controller (FLC). For validation, we have first utilized COMSOL Multiphysics software and then prototyped one enclosure along with the control system. Our experimental measurement exhibits its efficacy compared to the other design options.

This chapter is organized as follows. In Section 5.2, our proposed material selection procedure will be discussed. In Section 5.3, the design constraints and optimization strategies for the type, number, location/style, and placement of heating elements will be studied. An analytic modeling

approach will be presented in Section 5.4 to simplify the enclosure design procedure. In Section 5.5, the battery selection criteria will be discussed. Section 5.6 will present our fuzzy controller, while Section 5.7 will report the experimental results. Finally, a summary is made in Section 5.8.

5.2. Enclosure Material Selection

Material selection is highly important for our enclosure to achieve the due performance. To minimize the leakage of heat flux through the enclosure wall, the manufacturing material of the enclosure should have low thermal conductivity. Meanwhile, the material hardness should be taken into account as well due to harsh environmental conditions on the application sites. It would become easier to pursue these goals optimally if a software tool, such as Cambridge Engineering Selector (CES) [50], is utilized. The CES package can minimize or maximize specific performance aspects of a component based on a scheme called Ashby's selection methodology [60]. In our work, this software is utilized to find the best material with low thermal conductivity, high hardness, and low cost for our proposed enclosure.

Figure 5-1 shows the thermal conductivity of different materials versus price, while Figure 5-2 exhibits their relevance with reference to hardness. As can be seen from Figure 5-1, not only do wood, brick, paper, cardboard, flexible polymer foam (LD and VLD), polymethyl methacrylate, epoxies, and polycarbonate (PC) have low thermal conductivity constants, they are also inexpensive. Another important property to be considered is material hardness because temperature fluctuation may cause a crack or even damage due to thermal stress fatigue. As shown in Figure 5-2, polycarbonate is one of the best options among the materials listed above since it has relatively low thermal conductivity (0.22 W/(m·K)) and high hardness factor (24 HV). To

71

make a quantitative comparison among the factors of thermal conductivity, hardness, and price, we define the following linear cost function:

$$Cost = W.Q'$$ (1)

where W and Q are 1×3 matrices defined as *W= [Thermal conductivity, Hardness, Price]* and Q= [α, β, γ]. Here α, β, and γ are the user-defined weight coefficients equal to 1/3 by default.

Figure 5-1 Thermal conductivity (W/m.°C) versus price (CAD/kg) [50].

Figure 5-2 Thermal conductivity (W/m.°C) versus hardness [50].

By considering the equal weight coefficients for the enclosure design, the polycarbonate material is finally selected. Featuring several unique characteristics such as optical transparency, good toughness, and rigidity even at a relatively high temperature, polycarbonate is one of the most accessible engineering thermoplastics with better mechanical properties than cheaper polymers. These properties make polycarbonate a good choice for the applications such as compact disks, safety hard hats, and various insulators. Another important advantage of selecting polycarbonate as our enclosure material is its compatibility with SLS 3D printer [61]. Thanks to the low price of polycarbonate ($4.7/Kg), the fabrication cost of our proposed enclosure is very low to be fit for any industrial applications.

Besides the thermal conductivity, hardness, price, and compatibility with 3D printing for the prototyping purpose, the effect of the extreme cold environmental condition on polycarbonate needs to be considered as well. Parvin and Willianms investigated the effect of temperature (i.e., $-120\ ^0C \sim 20^0C$) on the fracture of polycarbonate [62]. This comprehensive study shows that the polycarbonate is completely ductile above -40^0C and semi-brittle between -60^0C and -80^0C. This study also discloses that the cracks might appear between -40^0C and -60^0C, but would not grow. In addition, the difference of the yield stress is just less than 4% between -40^0C and -60^0C. In our application for this study, the portable enclosures to be built are normally quite light and static without any constant external forces associated. Therefore, along with another insulation layer around the enclosure polycarbonate body as discussed in Section 5.7, the material reliability working at -60^0C or above can be typically maintained for the practical usage.

5.3.   Study of Heating Elements

In general, there are various electrical devices that can be used as electric heaters. Some of these heating devices in the industrial/commercial applications include incandescent light bulbs, thermal resistors, and thermoelectric devices. In this research, energy conversion efficiency, simplicity, and low cost are the major criteria that we have applied in the component selection.

An incandescent light bulb normally converts less than 5% of the energy into visible light. A study has shown that this number for a standard light bulb is only about 2.2%, while 97.8% of the energy is actually converted to heat [63]. That is to say, the incandescent light bulb may be used as a fair heat source. Another source of heat is the ceramic heating elements, e.g., ceramic thermal resistors that are both simple and inexpensive widely available in the typical electrical laboratories. Each ceramic thermal resistor is made of a small cylinder of graphite, surrounded by a protective ceramic layer. Short wires, or leads, are attached to both ends of the graphite cylinder and held in place by the coating material [64]. The third element that can be utilized as an electric heating source for the enclosure is a thermoelectric device. Its main advantage is that the low-temperature surface would absorb heat and the high-temperature surface would release heat when electrical current passes through the device. If the direction of the electrical current changes, the hot and cold surfaces would actually interchange [55, 65]. In other words, the direction of heat dissipation is completely reversible so that a heating device can be changed to a cooling device if the polarity changes.
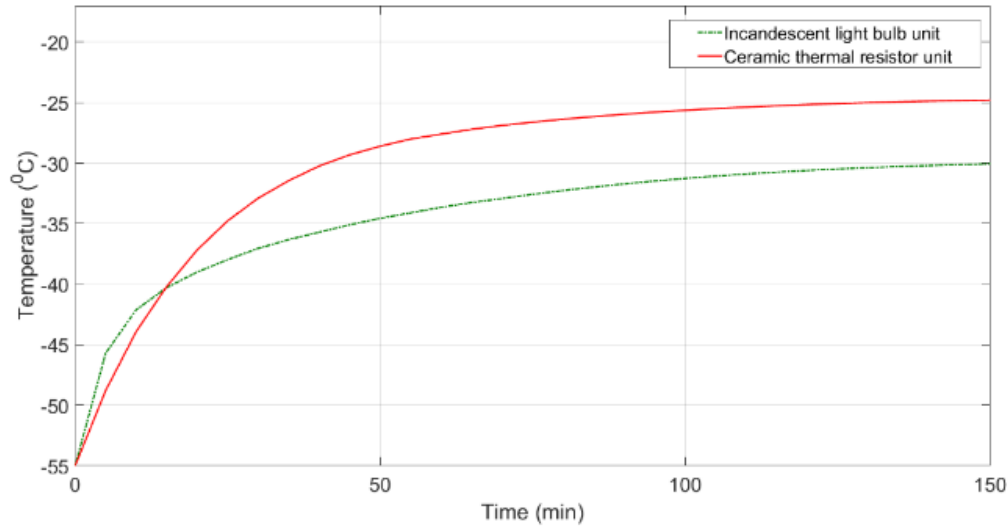
Figure 5-3 FEM temperature outputs of the enclosure equipped with ceramic thermal resistors or incandescent light bulbs as the heating elements.

The main purpose of this study is to design cost-effective enclosures for harsh environmental conditions. As a result, an inexpensive electric heater has to be selected. In general, the cost of a thermoelectric device is 35 times of a thermal resistor, while an incandescent light bulb is within the same price range as a thermal resistor. As a demonstrative experiment, a FEM simulation was done to compare the efficiency of the ceramic thermal resistor unit and the incandescent light bulb unit under the same conditions (i.e., the same total power consumption for both heating units in addition to the same environmental condition such as the same initial temperature $-55\,^{0}$C and the same surroundings). As can be seen in Figure 5-3, the ceramic thermal resistor unit can heat up the enclosure with $4.9\,^{0}$C more than the incandescent light bulb unit if energizing both units with the same amount of power within 150 minutes. As a result, the ceramic thermal resistors, as a better option in terms of heating efficiency, simplicity, and cost, are selected as the heating elements for the portable enclosures.

75

Besides the type of the heating elements, the number and placement of the thermal resistors have to be also studied. The placement study is to identify the best location and define the constraints for orientating the heating elements to warm up any enclosure with the best heating effect. Below our study will be mainly focused on three aspects: the number of the heating elements, the location/style of the heating elements, and the placement constraints.

First of all, we conduct two FEM simulations to study whether one single or multiple heating elements (given the identical electrical power) would lead to better heating effect. This case study is based on an enclosure with the dimension of 10 cm*10 cm*10 cm (for width, length, and height, respectively). For the first simulation, we use one thermal resistor consuming electrical power of 5W. In the second FEM simulation, we deploy two thermal resistors, each of which consumes electrical power of 2.5W. Figure 5-4 shows the temperature profile of the enclosure, which utilizes one single 5W thermal resistor. The initial ambient and inside temperature of the enclosure is -55 °C. Upon the initial conditions, the simulation is set to run 150 minutes.

As shown in Figure 5-4, the enclosure inner space cannot be warmed up uniformly although the temperature of some locations reaches around -40°C. As a result, it may cause serious damage due to the thermal stress that would be applied to the internal printed circuit boards or batteries accommodated inside the enclosure. Certain cracks might be propagated along the electronic devices to eventually cause open circuit problems [67,68].
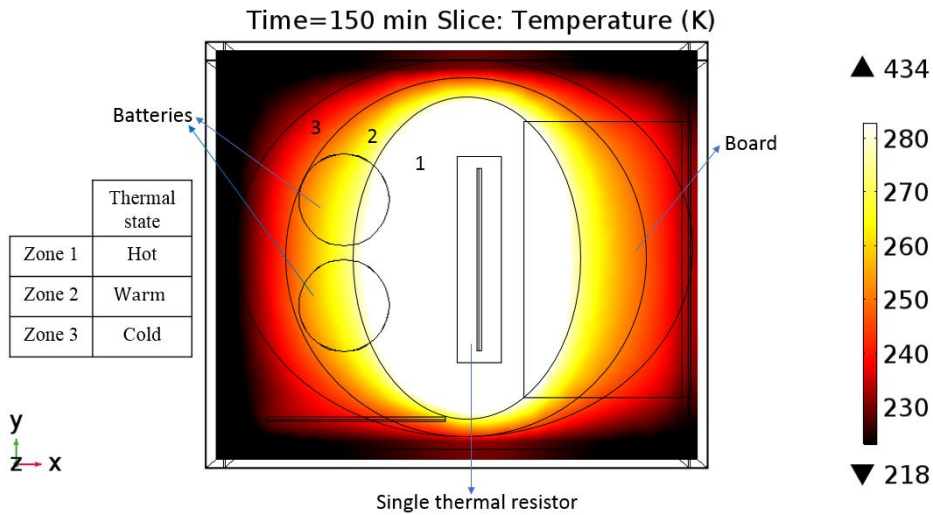
Figure 5-4 Enclosure FEM temperature profile with one single thermal resistor

In the next step, we deploy two thermal resistors, each of which consumes electrical power of 2.5W (i.e., the same total power as the previous model). As can be seen from Figure 5-5, the enclosure inner space still cannot be warmed up uniformly although the temperature profile looks better than the single thermal resistor case. Our further study shows that the same situation takes place when three 1.66W thermal resistors are utilized. However, as can be seen from Figure 5-6, with four 1.25W thermal resistors, the enclosure inner space can be warmed up uniformly.
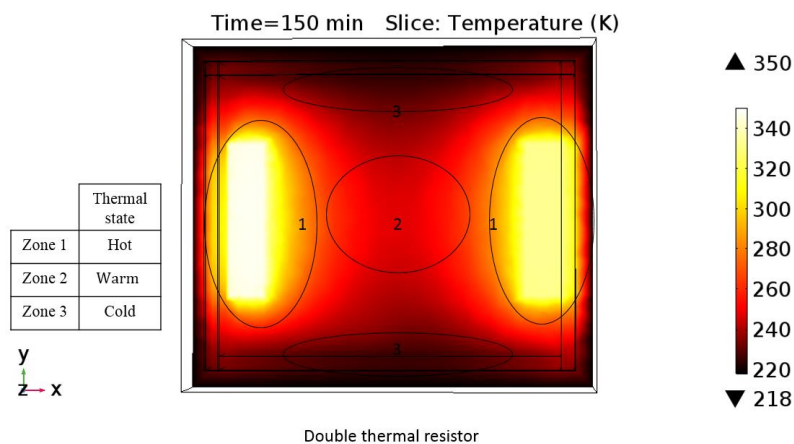
Figure 5-5 Enclosure FEM temperature profile with two thermal resistors

77
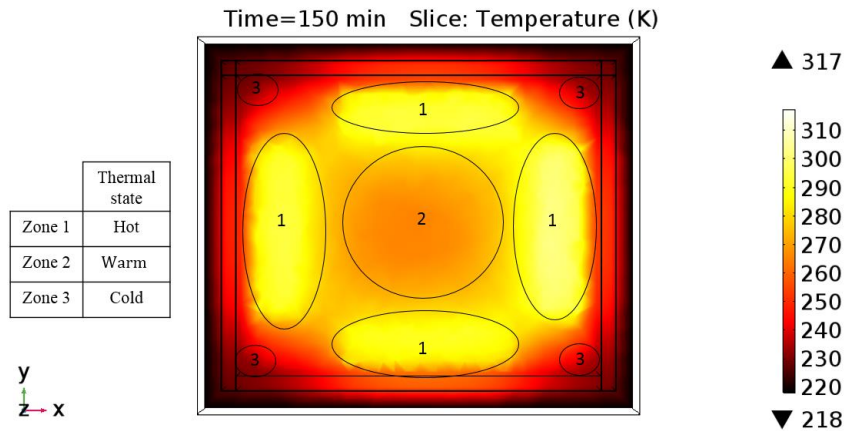
Figure 5-6 Enclosure FEM temperature profile with four thermal resistors

By assuming constant total power consumption, a comparison between the heating efficiency and the number of the deployed thermal resistors is shown in Figure 5-7. The temperature average and standard deviation are summarized into Table 5-1. As can be observed from the table, when five 1W thermal resistors are used, the average inner space temperature reaches $-33.37\,^0\text{C}$, which is less than 0.2% compared to that achieved by the four 1.25W thermal resistors. Meanwhile adding one more thermal resistor would incur more cost in addition to more space. As a result, a placement of four thermal resistors along each side is the best arrangement for uniformly warming up the inner space of the enclosure in this case study.
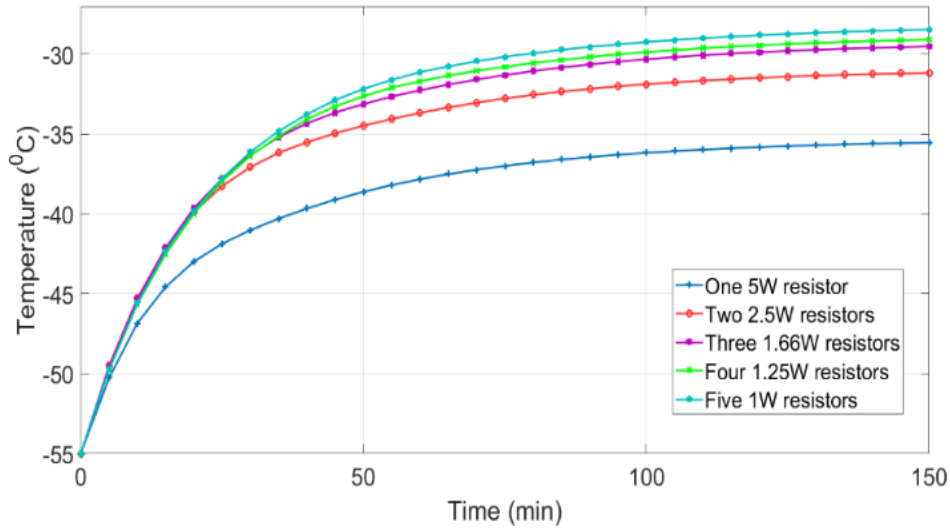
Figure 5-7 Average inner temperature profile versus the number of the deployed thermal resistors.

Table 5-1 The average temperature and standard deviation for 18 sampling points.

Number of thermal resistors	1	2	3	4	5
Average Temperature	-36.43	-35.46	-34.75	-33.42	-33.37
Temperature Standard Deviation.	8.6749	6.2694	5.8429	2.9726	2.5982

Another important issue for the heating element placement is to understand the constraints with reference to the electronic devices accommodated in the 3D enclosure. A 2D analysis shows that the best location of the heating elements is along the sides, while in the 3D model the heating elements may be placed on the top, bottom, or in the middle of the enclosure. Therefore, another group of simulation is executed to find out *the effective distance* from a thermal resistor. The effective distance stands for the distance from a unit power thermal resistor that can warm up the surrounding operational elements (e.g., printed circuit boards or batteries) without causing damage. By using curve fitting technique, the best approximation of a linear model based on a series of sampled data points can be obtained. As can be seen in Figure 5-8, the radial effective

79

distance d_r (i.e., the vertical one in the 2D view) and axial effective distance d_a (i.e., the horizontal one in the 2D view) for heating up the surrounding objects are between zone 2 and zone 5 (i.e., $l/9 < d_r < l/2.3$ and $w/6.4 < d_a < w/1.6$, where l and w are the thermal resistor device length and width respectively on the facing side). The root mean square (RMS) error is also listed in Figure 5-8. As a result, the best place of locating a thermal resistor unit is in the middle since it can distribute the heat in both directions. Another point that can be observed from Figure 5-8 is that the operational elements must not be placed in zone 1 (i.e., very close to or overlapping with the heating elements), which has the highest temperature compared to the other zones. Instead they should be located within the effective distance with reference to the thermal resistors.

	Approximate radial effective distance	Approximate axial effective distance	RMS Error
Zone 1	0	0	0
Zone 2	$l/9$	$w/6.4$	0.0104
Zone 3	$l/4.5$	$w/3.42$	0.0178
Zone 4	$l/2.75$	$w/1.96$	0.0115
Zone 5	$l/2.3$	$w/1.6$	0.0168
Zone 6	$> l/2.3$	$> w/1.6$	0.0143
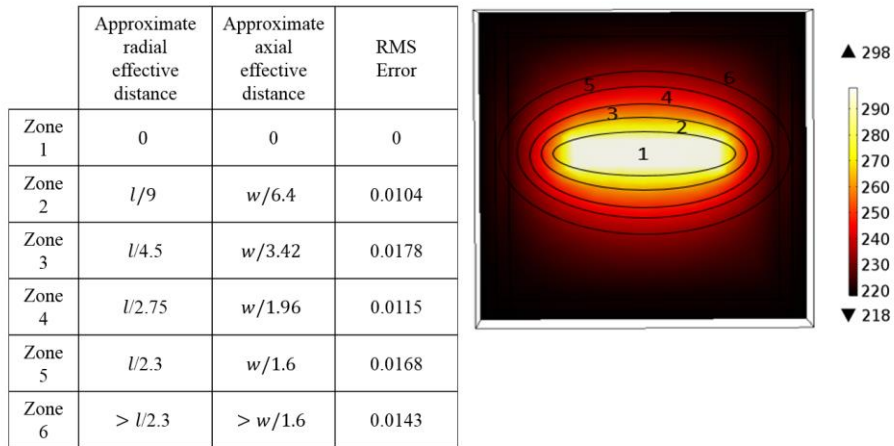
Figure 5-8 The effective distance of a unit power thermal resistor (l and w are the length and width of the thermal resistor).

Figure 5-9 shows the average temperature of 18 sampling points inside zones 1-6 in the 3D model of the enclosure as a function of time. The points, which are selected at $l/9 < d_r < l/2.3$ and $w/6.4 < d_a < w/1.6$ (i.e., within zones 2-5), have an average temperature above -40°C at the steady state (i.e., after passing the first 150 minutes), whereas the points located elsewhere are either too cold or unnecessarily too warm.
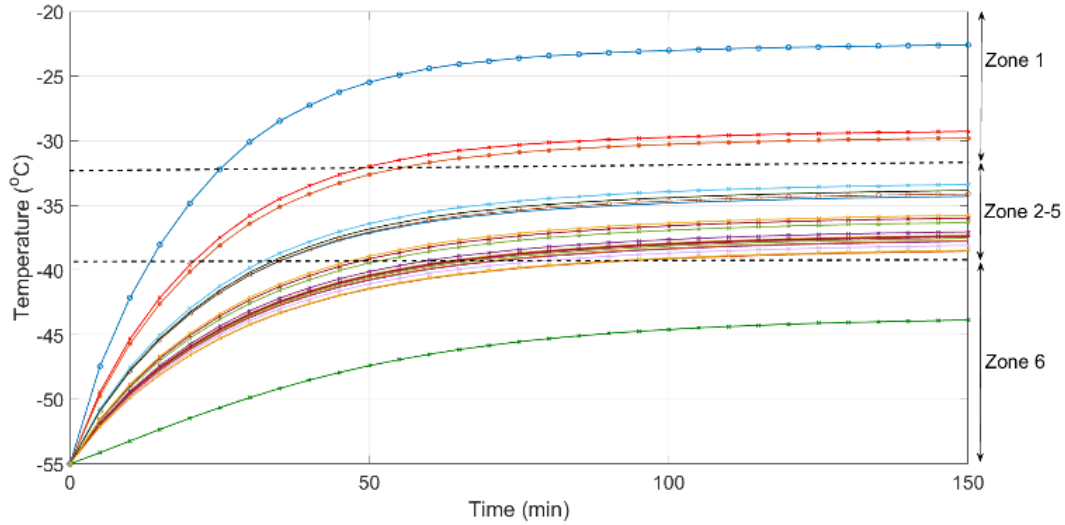
Figure 5-9 The temperature plot as a function of time for 18 sampling points inside zones 1-6.

Typically, thermal resistors are made from a small cylinder of graphite, surrounded by a protective ceramic layer. Short wires, or leads, are attached to the ends of the graphite cylinder, and held in place by the coating [11]. Figure 5-10 shows a typical style of thermal resistors. The heating conduction along the radius of carbon cylinder, which eventually leads to the radial effective distance as shown in Figure 5-8, is much more than the axial one because of larger surface contact with the coating layer. As a result, the area determined by the effective distance in Figure 5-8 has a rectangle shape instead of a square one.
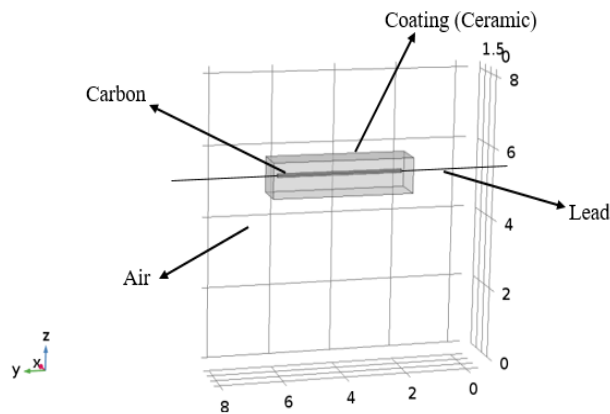
Figure 5-10 The schematic model of the ceramic thermal resistor.

81

In addition, we conduct another group of FEM simulation to study whether the size of the enclosure may change the effective distance of one unit thermal resistor. We deploy two unit thermal resistors in two different size enclosures with the same environmental condition, each of which consumes the same electrical power. As can be seen from Figure 5-11, the effective distances of two thermal resistors bear no change from each other due to the enclosure size change.

	Approximate radial effective distance	Approximate axial effective distance
Zone 1	0	0
Zone 2	$l/9$	$w/6.4$
Zone 3	$l/4.5$	$w/3.42$
Zone 4	$l/2.75$	$w/1.96$
Zone 5	$l/2.3$	$w/1.6$
Zone 6	$> l/2.3$	$> w/1.6$
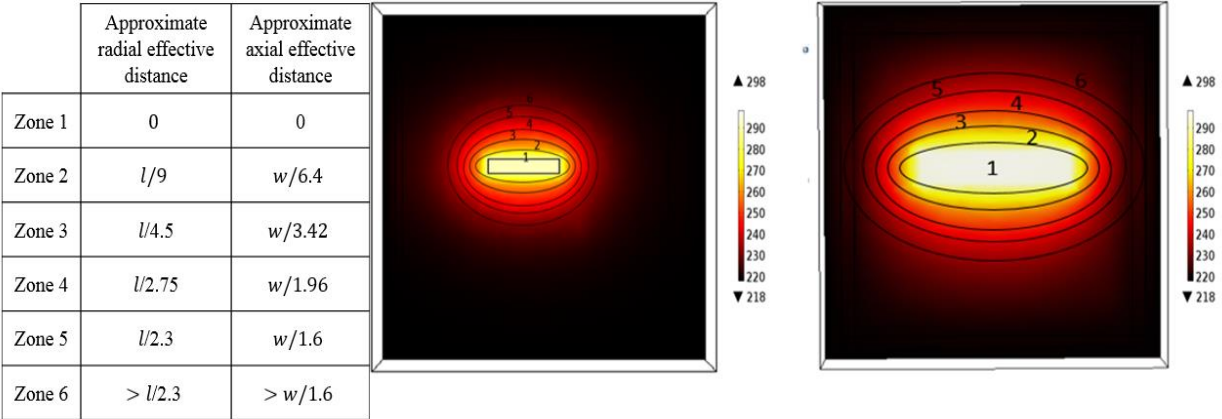
Figure 5-11 The effective distance of one unit thermal resistor in two enclosures with different sizes.

5.4.   Analytic Modeling

The case-study tactics and design knowledge accumulated from the previous section are highly valuable in the practical design process so that the designers can work out a specific enclosure design without any further expensive FEM simulations once the thermal modeling of the unit thermal resistor is completed. To this end, we are motivated to study how to optimize and compute the total required power and the total required number of the unit thermal resistors for maintaining the average inner temperature of the enclosure above -40℃ in the cold environment. Note that such a threshold temperature of -40℃ can be changed to another user-defined number as

82

long as the thermal modeling of the unit thermal resistor is conducted in advance accordingly. Based on the concept of effective distance supported by the curve fitting technique detailed in Section 5.3, we propose a general analytic design methodology as follows, with which the designers can quickly estimate the required power and thermal resistor number for heating up the enclosure to above -40℃ without any expensive FEM simulations. Figure 5-12(a) shows the schematic view of the enclosure with unit thermal resistors in the row-based configuration, which is aimed for the enclosures with relatively large geometry size (with reference to the size of the unit thermal resistor). In contrast, Figure 5-12(b) shows the schematic view in the side-based configuration, which is dedicated to the enclosures with small geometry size. Figure 5-12(c) depicts the effective distance of each unit thermal resistor.
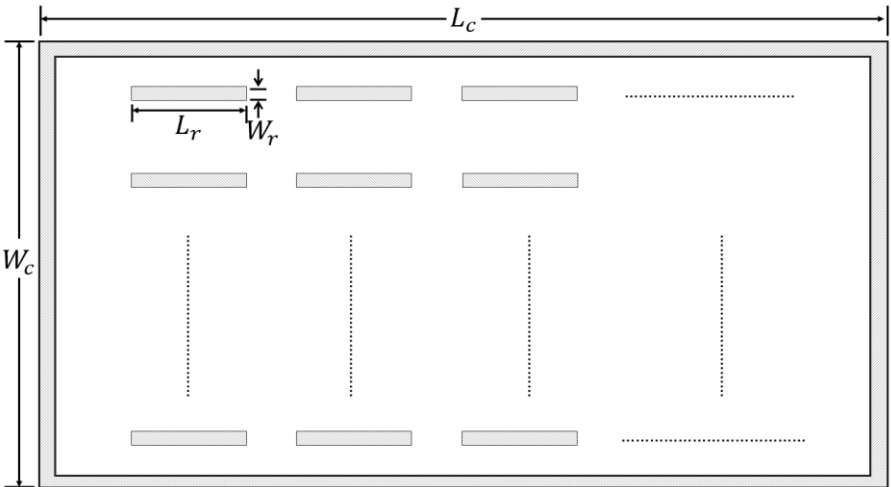
(a)
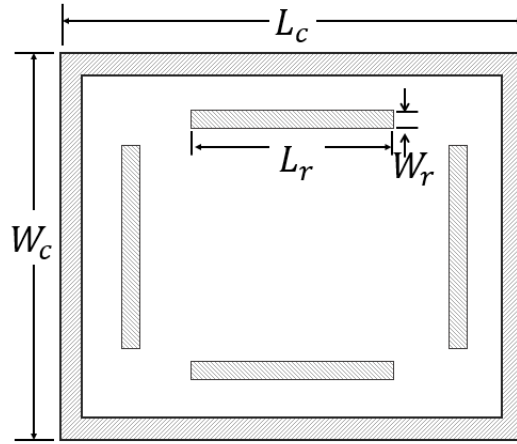
(b)
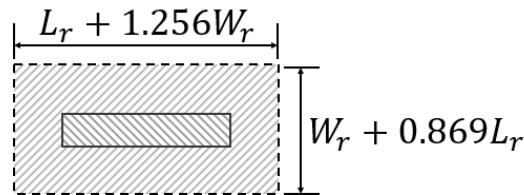
(c)

Figure 5-12 The schematic view of the enclosure with unit thermal resistors in the row-based configuration (a) and in the side-based configuration (b), with the effective distance (c) around a unit thermal resistor.

To establish the relationship between the number of unit thermal resistors and enclosure size, we should formulate a set of analytic functions. By considering the size limitation of the unit thermal resistor in addition to the maximum effective distance of each thermal resistor, we have set up two different models to identify the best location for orientating the heating elements to warm up the enclosure with the best heating effect. We have utilized a user-defined threshold value, which is equal to $2L_r$ by default, to determine which model should be selected. In other words, if each dimension of the enclosure is less than $2L_r$, the side-based configuration will be utilized so that each thermal resistor will be placed near each side for warming up the inner space of the enclosure uniformly. Otherwise, the following functions will be utilized:

$$A_1 = (W_c - 2t) \cdot (L_c - 2t), \tag{2}$$

$$A_2 = (L_r + 1.256W_r) \cdot (W_r + 0.869L_r), \tag{3}$$

$$A_1 = m.\,A_2, \tag{4}$$

$$m = \frac{(W_c-2t)\cdot(L_c-2t)}{(L_r+1.256W_r)\cdot(W_r+0.869L_r)} \text{ if } (L_c - 2t) > 2L_r \text{ and } (W_c - 2t) > 2W_r \ , \tag{5}$$

where W_c and L_c are the width and length of the enclosure, t is the thickness of the insulation layer, W_r and L_r are the width and length of each unit thermal resistor, and m is the number of the unit thermal resistors in the 2D view of the enclosure.

With the same tactic, for the 3D modeling, the number of the levels in Z direction can be found as follows:

$$k = \frac{H_c - 2t}{0.869L_r + W_r}, \tag{6}$$

where H_c is the height of the enclosure.

Thus, in all, the total required number of the unit thermal resistors can be calculated as follows:

$$N = m \cdot k \ . \tag{7}$$

To identify the number of the unit thermal resistors, N must be an integer number. As a result, the following ceiling function should be applied:

$$\widetilde{N} = \lceil N \rceil, \tag{8}$$

where N is the number of the applied unit thermal resistors. Accordingly, the total required power, which can make sure the average inner temperature of the enclosure is always above -40℃, can be expressed as:

$$P = \widetilde{N} \cdot P_{unit} \, , \tag{9}$$

where P_{unit} is the power of the unit thermal resistor. The estimation above would help a designer to evaluate the number of the required thermal resistors and the corresponding required power without any expensive FEM simulations.

Recall the previous case study described in Section 5.3, where W_c , H_c, and L_c are all equal to 10 cm. In addition, W_r and H_r are equal to 1 cm, while L_r is equal to 4.5 cm. As a result, $(L_c - 2t)$ is equal to 8cm, which is less than the threshold value of $L_r = 9$cm. Thus, the side-based configuration will be utilized. It means that each thermal resistor will be placed along each side. In all, this proposed design methodology would significantly simplify the practical design process to output the optimal total number and arrangement of unit thermal resistors yet without compromising the estimation accuracy.

5.5. Battery Selection and Power Management

To select batteries as a power source for the heating elements in the enclosure, there are many constraints to be considered, including size, maximum current discharge, rechargeable or non-rechargeable type, operating temperature, safety, lifetime, etc. By considering these crucial factors, two types of non-rechargeable batteries along with another rechargeable backup battery are selected for this work. Due to the cold initial environmental condition (-55 °C), the best type is the lithium-thionyl chloride batteries (Li/SOCl2), which can work at low temperature with the highest energy density (up to 1280Wh/L) among all the lithium batteries [68]. For instance, a SAFT LST17330LST lithium-thionyl chloride battery can be selected for the initial kick-start stage in the case-study enclosure design discussed in Section 5.3. The operating temperature range of this

battery is between -60°C to 85°C. It is used for warming up the enclosure starting from the initial temperature of -55 °C.

However, the lithium-thionyl chloride battery is non-rechargeable and only good for short-term applications. For the enclosure, a rechargeable nickel–metal hydride battery can be used under the regular weather condition. The solar radiation may be available on certain days each year for the regions such as Alaska, Northern Canada, and Antarctica. Besides the solar cells as an effective charging method, a small wind power turbine can also be used to supply the enclosure in the cloudy or even stormy days. Thus, the rechargeable battery, which is charged during this time, can be used as the main power source. For instance, for the case study described in Section 5.3, we propose to include a 10000 mAh NiMH AccuPower rechargeable battery into that enclosure design. Furthermore, in the worst scenario, an array of backup powerful lithium manganese dioxide batteries whose operating temperature is -40°C and above may be used besides the rechargeable battery. For instance, for the case-study enclosure discussed in Section 5.3, we have selected lithium manganese dioxide Energizer LA522-9 battery, whose nominal temperature range is between -40°C and 60°C. Therefore, the combination of the rechargeable nickel–metal hydride battery and the lithium manganese dioxide battery form the main power source for the enclosure in the regular operation mode.

Another important issue to be considered is the maximum runtime of the batteries at the initial kick-start stage because the thermal resistor unit must be on for a certain period without any rest. In our case-study enclosure discussed in Section 5.3, since the average current of 0.617 A should last for 140 minutes at the initial kick-start stage, the entire heating system needs 1.44 AH. The selected lithium-thionyl chloride battery (Li/SOCl2) has its power capacity of 17 AH. That is to say, this battery can start up the heating system for 11 times from the extremely cold environment

(up to -55°C). This should be sufficient since normally only one time is needed for the heating system to be heated up directly from -55°C ~ -40°C. After the kick-start stage, the control unit will repeatedly tune the heating elements to control the enclosure inner temperature above -40°C. In the sunshine days the rechargeable battery can be continuously charged with solar power, while in the windy days the rechargeable battery can be continuously charged with wind power. In addition, one Energizer LA522-9 battery working at -40°C will supply the system as the backup power source for 228 hours in the worst scenario when there is no solar or wind power for a certain period of time. Depending on the space availability of the enclosure, the number of this backup battery can be increased to maximize the operational time (e.g., four backup batteries can supply the heating system in our case-study enclosure discussed in Section 5.3 for 38 days).

5.6.   Fuzzy Logic Controller

Controlling the inner temperature of the enclosure is an essential part of this research since in the remote area the enclosure has to detect the temperature and tune the thermal unit autonomously. As a result, we have developed a fuzzy logic controller to control the inner temperature of the enclosure. In general, the fuzzy logic control method is useful for the systems that can hardly be mathematically modeled [49]. In our study, the required power that the thermal resistor unit needs to heat up the enclosure is the input of our target system to be controlled, while the temperature that is read out by the temperature sensors is the output of our target system.

The Fuzzy Logic Controller (FLC) consists of four components: fuzzification interface, knowledge base, inference engine, and a defuzzification interface. Each of these components has a different role in the control process and thus affects the performance of the whole system. The fuzzification interface is a mapping operation of numerical data from the input to linguistic terms.

88

The knowledge base works as a knowledge source to provide necessary information for all the components of the fuzzy controller. The inference engine, also called logical decision maker, is actually the brain of the controller. In other words, it simulates the decision-making process of human beings. Table 5-2 lists the properties of the inference engine for our proposed FLC. We have used the Mamdani-type inference engine with the applied options for and-method, or-method, implication, and defuzzification. At the end of the inference stage, the obtained result is a fuzzy value that cannot be directly used to control the real world (e.g., the temperature in our case). So, this fuzzy value has to be defuzzified through the defuzzification interface to a crisp value to be directly used outside [69]- [70].

Table 5-2 Properties of the fuzzy logic controller

Name	Applied Option
Controller type	Mamdani
And method	Min
Or method	Max
Implication	Min
Defuzzification	Centroid

A membership function is a curve that defines how each point in the input space is mapped to a membership value (or degree of membership) between 0 and 1. It is important for the fuzzification and defuzzification stages of the FLC to evaluate the non-fuzzy input values to fuzzy linguistic terms. A membership function can be implemented to measure the linguistic terms. For instance, the membership functions for the linguistic terms of the temperature variable used in our proposed FLC are depicted in Figure 5-13.

89

In the fuzzification process, a real scalar value is mapped into a fuzzy value. The arrangement of fuzzy variables through the defined membership functions can ensure that these real values get translated into the proper fuzzy values. After translating such real values into fuzzy values as shown in Figure 5-13, the possible outcome is called "linguistic terms". The control rules are used to further convert the linguistic terms to the output linguistic variables, which linguistically express the applied values to the real world, i.e., the thermal resistors for temperature control in our proposed FLC. In Table 5-3, we present the developed rules of our proposed FLC. The linguistic input terms include very negative, negative, zero, positive, very positive, while the linguistic output variables include zero, very low, low, high, very high.

Table 5-3 The control rules of the developed fuzzy logic controller

Controller Rule 1: *If the temperature difference is very negative, then the power must be zero*
Controller Rule 2: *If the temperature difference is negative, then the power must be very low*
Controller Rule 3: *If the temperature difference is zero, then the power must be low*
Controller Rule 4: *If the temperature difference is positive, then the power must be high*
Controller Rule 5: *If the temperature difference is very positive, then the power must be very high*
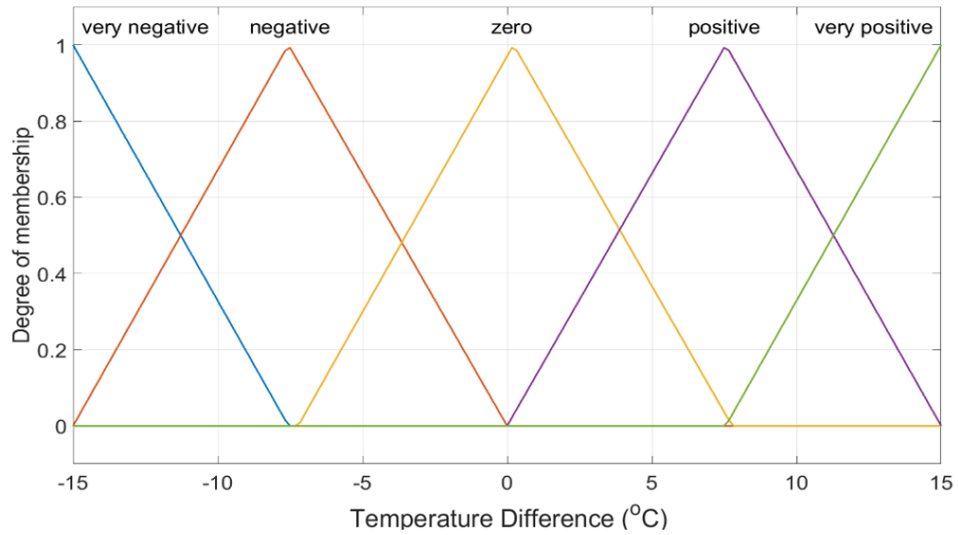
Figure 5-13 The correspondence between fuzzy input values and linguistic terms.

As can be observed in Figure 5-13, the input of the fuzzy sets is defined as the temperature difference between the reference temperature (i.e., -40°C) and the actual sampled temperature. Based on the input fuzzy terms, our developed fuzzy control rules can give an appropriate output fuzzy set and then in turn a specific power value as shown in Figure 5-14.
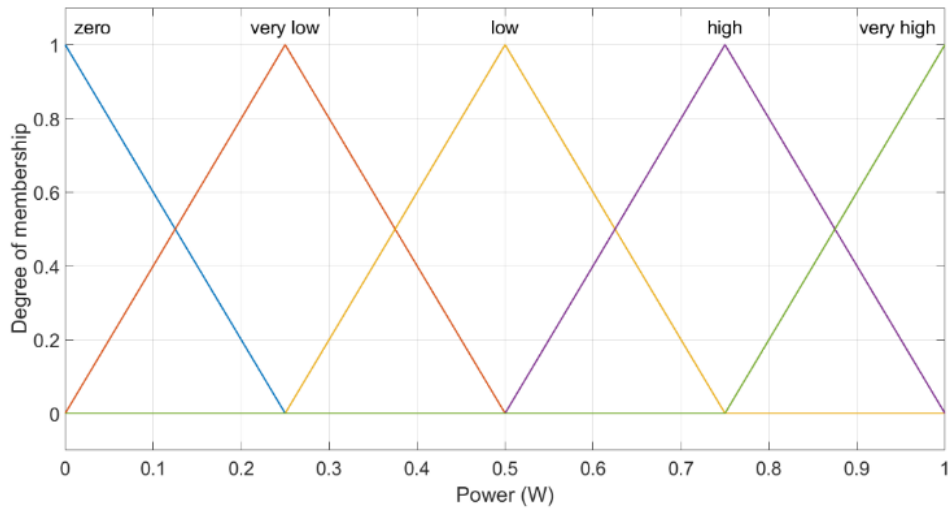
Figure 5-14 Membership functions corresponding to fuzzy out sets.

Figure 5-15 shows an example of mapping a fuzzy input (i.e., temperature difference) to a fuzzy output (i.e., power). Here, we assume the temperature difference to be -3.38°C. This point on that scale has five truth values (one for each of the five functions). The vertical red line in the left image represents a particular temperature difference (-3.38°C). Since the vertical line in the first row indicates zero, this temperature difference may be interpreted as "very negative". Similarly, the second, third, fourth, and fifth rows may be interpreted as "negative", "zero", "positive", and "very positive", respectively. In the next step, for each truth value, the membership function must be evaluated and then with the or-operator the resulting curves will be combined. In the defuzzification step, the weight-center of the shaded area of the curves will be determined. Finally, the X-axis position of this center (e.g., 0.38W as shown in Figure 5-15) is actually used as the final output power of the FLC system.
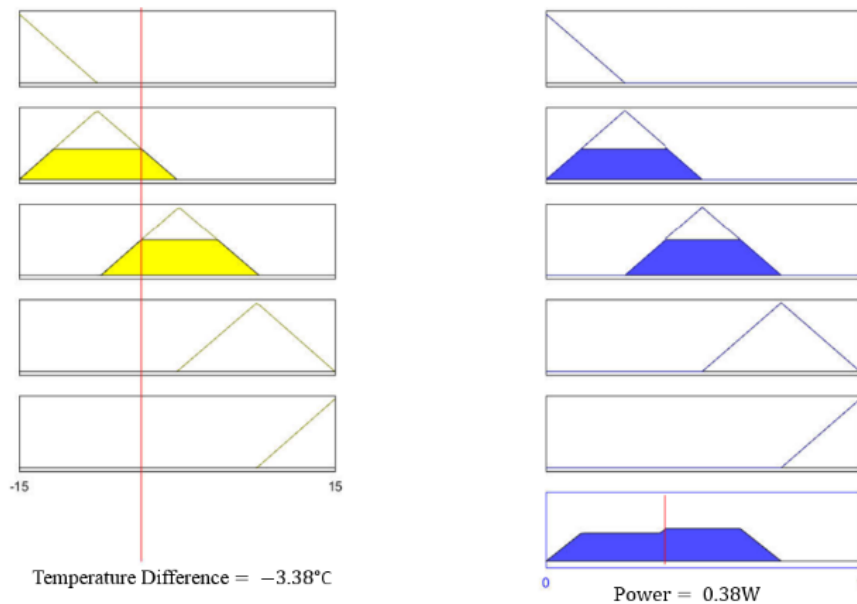
Figure 5-15 An example of the correspondence/mapping between fuzzy input and output set.

92

5.7.   Experiments and Discussion

By following the case study discussed in Section 5.3, we prototyped the enclosure with a 3D printer (Formlabs Form 2SLA). Figure 5-16 shows this prototype, which is made of polycarbonate. To make sure that our enclosure has the minimum heat flux leakage, we need to form proper insulation around the enclosure. Among the different options, foam insulation has become the most widely used insulation method. In this work, we select polyurethane (PU) foam as an insulation layer thanks to its low thermal conductivity and low cost in addition to ease of processing.

Table 5-4 shows the material properties of the enclosure walls, the insulation layer, and the thermal resistors.
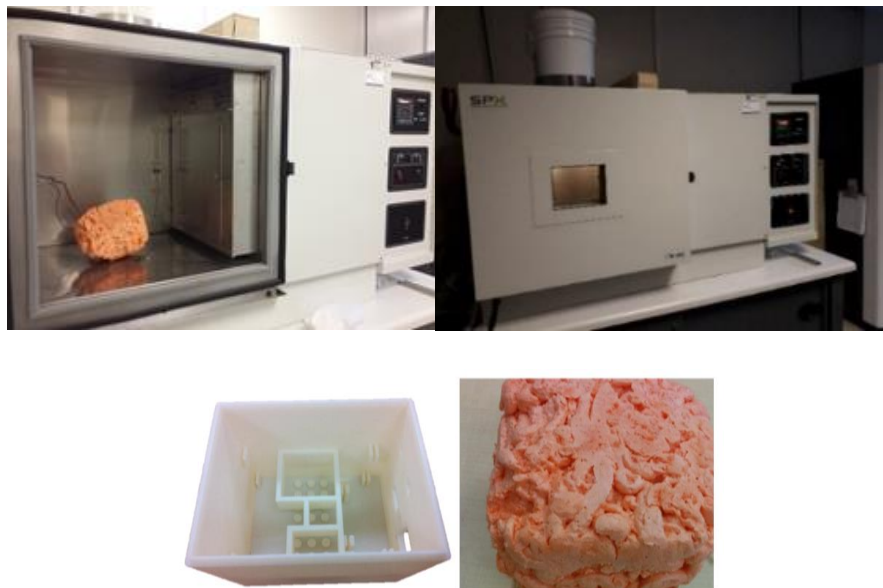
Figure 5-16 Cold chamber setup and the enclosure prototype with an insulation layer.

Table 5-4 Material properties of the enclosure walls (polycarbonate), the insulation layer (air and polyurethane), and thermal resistors (carbon and ceramic).

Mechanical property	Ceramic (SiC)	Carbon (Graphite)	Polyurethane (PU)	Polycarbonate (PC)	Air (T= -55$^o C$)
Mass density	3100 (Kg/m^3)	1950 (Kg/m^3)	446 (Kg/m^3)	1220 (Kg/m^3)	1535 (g/m^3)
Elastic modulus	---	---	---	2.4 (GPa)	---
Poisson's ratio	---	---	---	0.37	---
Thermal Conductivity	125 (W/m·K)	470 (W/m·K)	0.02 (W/m·K)	0.22 (W/m·K)	0.0204 (W/m·K)
Heat Capacity	0.80 (KJ/kg/C)	0.83 (KJ/kg/C)	1.8 (KJ/kg/C)	1.3 (KJ/kg/C)	1.05 (KJ/kg/C)

The enclosure was put into the cold chamber to have its ambient temperature of -55°C. Then the enclosure started to warm up and the inner temperature was recorded. To measure the inner temperature of the enclosure, one temperature sensor DS18B20 (with a measurement range of -55℃ ~ +125℃ featuring strong disturbance resistance and high precision) was utilized.

In order to maintain the average temperature of the enclosure at -40℃ or above, our proposed fuzzy control logic, which is detailed in Section 5.6, was utilized in our experiments. Figure 5-17 shows the schematic of the close-loop testbench with our proposed fuzzy logic controller and enclosure prototype. The reference temperature of the fuzzy logic controller was set as -40℃. We implemented the proposed fuzzy logic controller and power-to-voltage converter with MATLAB

Simulink. The output voltage from the power-to-voltage converter module was connected to our enclosure prototype to power up the thermal resistor unit. Figure 5-18 shows the average temperature of the enclosure prototype when a fuzzy control controller is utilized. As can be seen from this figure, the settling time decreases compared to the open-loop system as shown in Figure 5-9. This shows the performance of our proposed enclosure heating and control system, which can reach -40℃ faster and more smoothly.
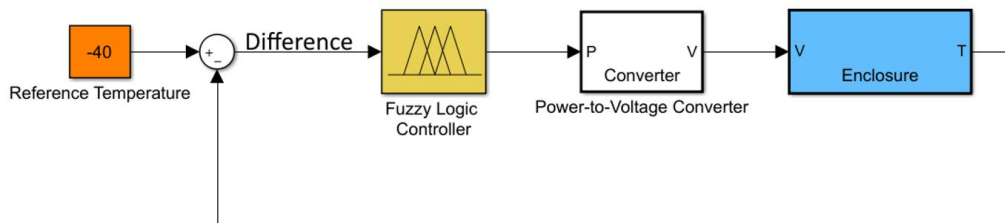
Figure 5-17 The schematic of the close-loop system with the proposed fuzzy controller.

To demonstrate the efficiency of our proposed fuzzy logic controller, we also implemented two other controllers for the comparison purpose with the same testbench depicted in Figure 5-18. State machine controllers and proportional–integral–derivative (PID) controllers are widely used for the systems that can hardly be mathematically modeled. The state machine represents a reactive system that contains a finite number of states [56,70]. In other words, the controller changes states based on the categorized conditions of the target system. In our implementation there are two states: "0" when the controller is not active, and "1" when the controller is active. The controller would decide when to switch between these two states based on a function called "Is System Cool", which compares the sensed temperature from the DS18B20 temperature sensor with the reference temperature (-40°C). On the other side, the PID controller calculates the error between the reference temperature and the sampled temperature of the target system. It can decrease the error by using proportional, integral, and derivative operators. Figure 5-19 shows the comparison among

95

the state machine, PID, and our proposed fuzzy logic controllers. As can be seen from this figure, the output from the fuzzy logic controller has the least oscillation around the reference temperature since the output power can continuously change between 0 and 1. In contrast, the state machine controller suffers large fluctuation (±0.26℃) around the reference temperature of -40℃. This is mainly due to the simple control logic used in this controller. Although the classical PID controller could work better than the state machine controller in terms of temperature smoothness segmentally, the magnitude of the temperature rippling (±0.31℃) along the reference temperature was actually even larger. As for our proposed fuzzy logic controller, the average oscillation around the reference temperature (-40℃) was only less than ±0.02℃.
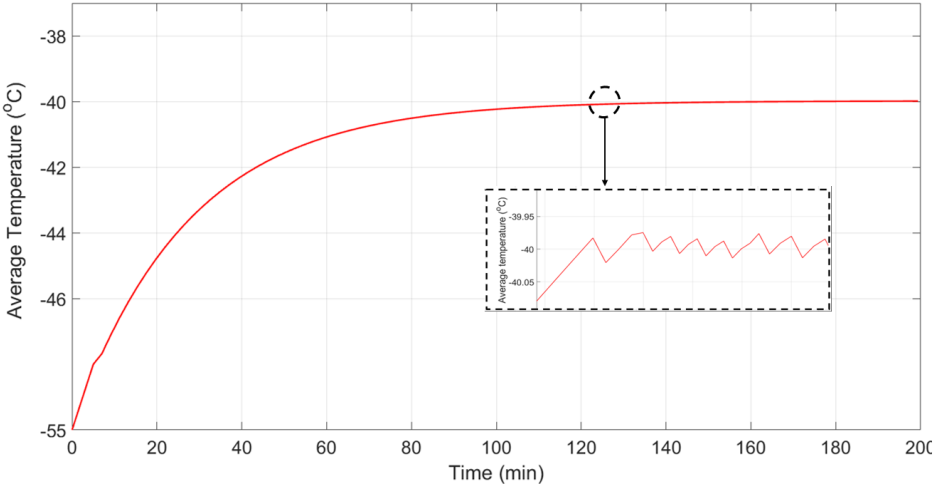
Figure 5-18 The average temperature of the enclosure prototype versus time driven by the proposed fuzzy logic controller.

To demonstrate the power consumption, the outputs of the system for the state machine, PID, and fuzzy logic controllers are plotted in Figure 5-20. To calculate the total power consumption within the unit time (e.g., one hour), equation (10) can be utilized and the results are summarized in Table 5-5. One can observe that, in the steady-state period, the total power consumption of the

96

FLC system is 17.6% less than the state machine controller and 38.04% less than the PID controller.

$$P_t = \int_{t=0}^{n} P dt \qquad (10)$$

Table 5-5 The total power consumption (Wh)

Time (min)	60	120 (steady-state)	180	240
State machine	5.6173	9.4640	13.3277	17.1672
PID	3.5567	9.9767	16.3967	22.8267
FLC	4.8121	7.9197	11.0997	14.1495
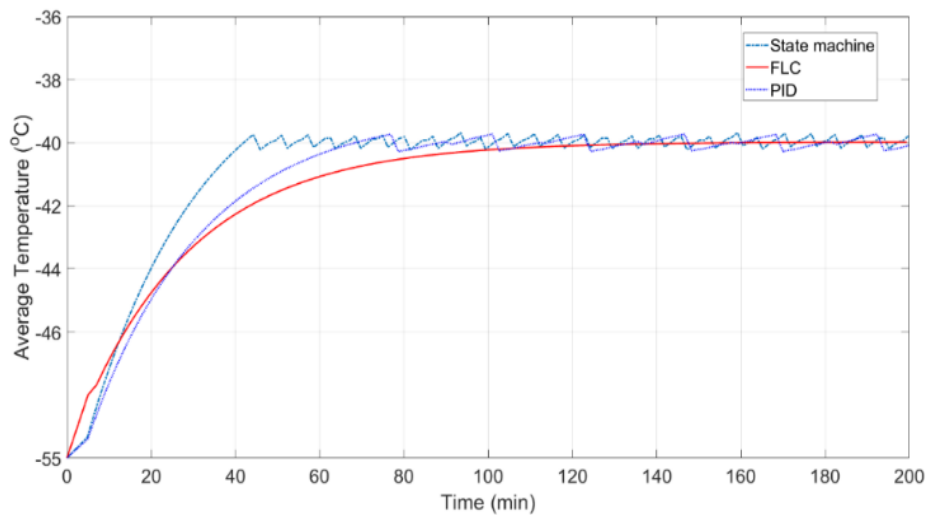
Figure 5-19 Comparison of the average temperature versus time among the state machine, PID, and fuzzy logic controllers.
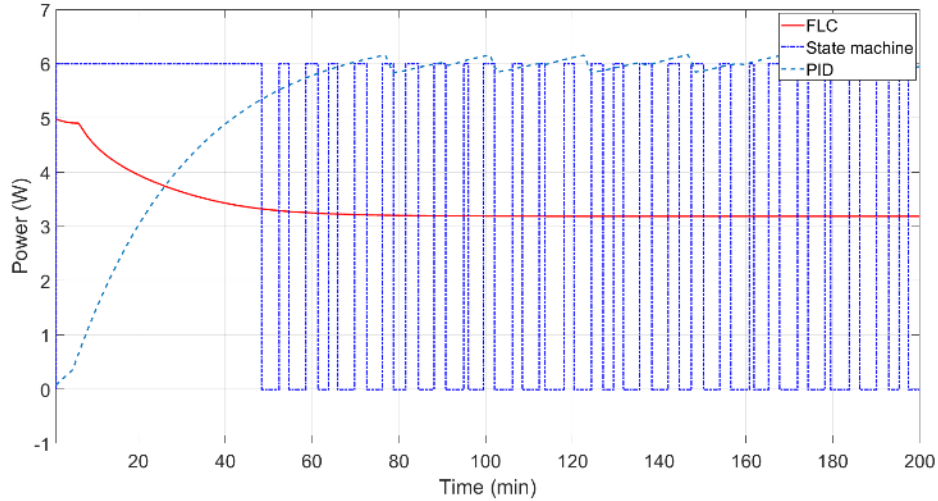
Figure 5-20 Comparison of the power outputs among the state machine, PID, and fuzzy logic controllers.

5.8.   Summary

In this chapter, we presented a complete design methodology for cost-effective portable enclosures, which can accommodate industrial-class electronic devices at the ambient temperature as low as -55°C. Thanks to low thermal conductivity, high hardness, and low cost, polycarbonate was selected as the manufacturing material. Among the alternatives, we selected ceramic thermal resistors as the heating elements inside the enclosure. Moreover, the optimal number, location/style, and the placement constraints of the heating elements were studied. Based on the thermal modeling of the unit heating elements by using curve fitting technique, we proposed an analytic model, which can be used to estimate the number of the required thermal resistors or the total required power in the practical enclosure design. Besides studying the battery power management, we developed a fuzzy logic controller to control the inner temperature of the enclosure. Our experimental results demonstrated that the prototype enclosure with the proposed fuzzy logic controller can achieve excellent performance compared to the other alternatives.

Chapter 6   Conclusion and Future Work

In this thesis, we have studied the applications of finite element method in the design and optimization of cost-effective portable instrumentation. In particular, we have presented a complete design methodology for cost-effective portable micro-dispensers for bio-medication applications. We have developed an analytic modeling method to design the key micro-dispenser parameters, including the critical displacement of the elastic diaphragm layer and the outlet hole diameter of the disposable tank. We have validated our proposed design method and demonstrated its high efficacy by using FEM simulations and prototype measurements.

In addition, we have proposed an optimization method for the piezoelectric-based actuator, which can maximize the performance of micropump systems. The analytic analysis of the piezoelectric-based actuator was first conducted and then verified by using FEM simulations. The comparison between the COMSOL Multiphysics simulation and analytic computation reveals the high accuracy of our deducted analytic solution, whose error is less than 1%. This is valuable since the designers can estimate the natural frequencies and mode shapes of a new configuration with different dimensions efficiently by using our proposed analytic solution rather than depending on any expensive FEM simulations. Moreover, the experimental setup was established to measure the maximum displacement for a comparison with the FEM simulations. The results show that the difference between the FEM simulations and our experimental measurements is less than 4%. Furthermore, the proposed actuator was applied to a typical valveless micropump to evaluate its functionality. The comparison between a regular valveless micropump with a single-PZT-sheet actuator and the same micropump with a double-PZT-sheet actuator reveals that the flow rate can increase up to 8.23 times.

Furthermore, we have also presented a complete design methodology for cost-effective portable enclosures, which can accommodate industrial-class electronic devices at the ambient

temperature as low as -55°C. We have used the FEM to model the thermal profile of the unit heating element with the aid of curve fitting technique. On top of that, we have proposed an analytic model, which can be used to estimate the number of the required heating elements or the total required power in the practical enclosure design. Besides studying the battery power management, we have developed a fuzzy logic controller to control the inner temperature of the enclosure. Our experimental results demonstrated that the prototype enclosure with the proposed fuzzy logic controller can achieve excellent performance compared to the other alternatives.

As the future work, we plan to explore more FEM applications in the engineering and applied science domain. In particular, we may extend our research on the micro-dispensers. For the future development of our proposed model, an active microvalve may be designed for the disposable main tank. In this way, the volume of droplets can be automatically controlled by the users for flexibility improvement. As for the enclosure design, a further study on the material aspects can be conducted in the context of cold environment. We may also refine our enclosure structural study and enrich our experimental measurements by following the international and national enclosure rating standards.

References

[1]   S. Kaviani, M. Bahrami, A. M. Esfahani, and B. Parsi, "A modeling and vibration analysis of a piezoelectric micro-pump diaphragm," *Comptes Rendus Mécanique,* vol. 342, no. 12, pp. 692–699, 2014.

[2]   Y. Hu, X. Liang, and W. Wang, "A theoretical solution of resonant circular diaphragm-type piezo actuators with added mass loads," *Sensors and Actuators A: Physical,* vol. 258, pp. 74–87, 2017.

[3]   A. M. Esfahani and M. Bahrami, "Vibration analysis of a circular thin polymeric piezoelectric diaphragm with fluid interaction," *International Journal of Mechanics and Materials in Design,* vol. 12, no. 3, pp. 401–411, Oct. 2015.

[4]   A. M. Esfahani, M. Bahrami, and S. R. G. Anbarani, "Forced vibration analysis of a viscoelastic polymeric piezoelectric microplate with fluid interaction," *Micro & Nano Letters,* vol. 11, no. 7, pp. 395–401, 2016.

[5]   Y. Sheikhnejad, Z. Vujicic, Á. Almeida, R. Bastos, A. Shahparia, and A. Teixeira, "Analytical transient analysis of peltier device for laser thermal tuning," *Third International Conference on Applications of Optics and Photonics,* pp. 15-27, 2017.

[6]   P. S. Dittrich and A. Manz, "Lab-on-a-chip: microfluidics in drug discovery," *Nature Reviews Drug Discovery,,* vol. 5, no. 3, pp. 210–218, 2006.

[7]   I. Barbulovic-Nad, H. Yang, P. S. Park, and A. R. Wheeler, "Digital microfluidics for cell-based assays," *Lab on a Chip,* vol. 8, no. 4, pp. 519-529, 2008.

[8]   E. Samiei, M. Tabrizian, and M. Hoorfar, "A review of digital microfluidics as portable platforms for lab-on a-chip applications," *Lab on a Chip,* vol. 16, no. 13, pp. 2376–2396, 2016.

[9]   J. Berthier, Micro-drops and digital microfluidics, Waltham: William Andrew, 2013.

[10]   Y.-N. Wang and L.-M. Fu, "Micropumps and biomedical applications A review," *Microelectronic Engineering,* vol. 195, pp. 121–138, 2018.

[11]   L. Shang, Y. Cheng, and Y. Zhao, "Emerging droplet microfluidics," *Chemical Reviews,* vol. 117, no. 12, pp. 7964–8040, 2017.

[12]   K. Choi, A. H. Ng, R. Fobel, and A. R. Wheeler, "Digital Microfluidics," *Annual Review of Analytical Chemistry,* vol. 5, no. 1, pp. 413–440, 2012.

[13]   E. Samiei, M. D. D. L. Derby, A. V. D. Berg, and M. Hoorfar, "An electrohydrodynamic technique for rapid mixing in stationary droplets on digital microfluidic platforms," *Lab on Chip,* vol. 17, no. 2, pp. 227–234, 2017.

[14]   W. Satoh, H. Hosono, and H. Suzuki, "On-chip microfluidic transport and mixing using electrowetting and incorporation of sensing functions," *Analytical Chemistry,* vol. 77, no. 21, pp. 6857–6863, 2005.

[15]   R. B. Fair, "Digital microfluidics: is a true lab-on-a-chip possible?," *Microfluidics and Nanofluidics,* vol. 3, pp. 245–281, 2007.

[16]   P. Hung, A. Chen, J. Lee, Y. Lu, and S. Fan, "Genetic testing on electrowetting-on-dielectric chips for magnetic bead-based DNA extraction," in *In Proceedings of the 14th IFToMM World Congress*, Room, 2015..

[17]   D. Chatterjee, H. Shepherd, and R. L. Garrell, , "Electromechanical model for actuating liquids in a two-plate droplet microfluidic device," *Lab on a Chip,* vol. 9, no. 9, pp. 1219-1229, 2009.

[18]   H. Ren, "Automated on-chip droplet dispensing with volume control by electro-wetting actuation and capacitance metering," *Sensors and Actuators B: Chemical,* vol. 98, no. 2-3, pp. 319–327, 2004.

[19]   H. Ding, S. Sadeghi, G. J. Shah, S. Chen, P. Y. Keng, C.-J. "C. Kim, and R. M. V. Dam, "Accurate dispensing of volatile reagents on demand for chemical reactions in EWOD chips," *Lab on a Chip,* vol. 12, no. 18, pp. 3331-3340, 2012.

[20]   H. Kim, M. S. Bartsch, R. F. Renzi, J. He, J. L. V. D. Vreugde, M. R. Claudnic, and K. D. Patel, "Automated digital microfluidic sample preparation for next-generation DNA sequencing," *Journal of Laboratory Automation,* vol. 16, no. 6, pp. 405–414, 2011.

[21]   D. J. Laser and J. G. Santiago, "A review of micropumps," *Journal of Micromechanics and Microengineering,* vol. 14, no. 6, pp. 50-62, 2004.

[22]   J. S. Hong, S. H. Ko, K. H. Kang, and I. S. Kang, "A numerical investigation on AC electrowetting of a droplet," *Microfluidics and Nanofluidics,* vol. 5, no. 2, pp. 263–271, 2007.

[23]   M. Russel, P. Selvaganapathy, and C. Ching, "Electrical discharge characteristics of a dielectric liquid under external flow in a microchannel with planar electrode configuration," *Journal of Electrostatics,* vol. 87, no. 2, pp. 212–216, 2017.

[24]   B. Liu, J. Sun, D. Li, J. Zhe, and K. W. Oh, "A high flow rate thermal bubble-driven micropump with induction heating," *Microfluidics and Nanofluidics,* vol. 20, no. 11, pp. 1-8, 2016.

[25]   A. Darhuber, J. Valentino, S. Troian, and S. Wagner, "Thermocapillary actuation of droplets on chemically patterned surfaces by programmable microheater arrays," *Journal of Microelectromechanical Systems,* vol. 12, no. 6, pp. 873–879, 2003.

[26]   A. A. García, A. Egatz-Gómez, S. A. Lindsay, P. Domínguez-García, S. Melle, M. Marquez, M. A. Rubio, S. Picraux, D. Yang, P. Aella, M. A. Hayes, D. Gust, S. Loyprasert, T. Vazquez-Alvarez, and J. Wang, "Magnetic movement of biological fluid droplets," *Journal of Magnetism and Magnetic material,* vol. 311, no. 1, pp. 238-243, 2007.

[27]   Z. Guttenberg, H. Müller, H. Habermüller, A. Geisbauer, J. Pipper, J. Felbel, M. Kielpinski, J. Scriba, and A. Wixforth, "Planar chip device for PCR and hybridization with surface acoustic wave pump," *Lab on Chip,* vol. 5, no. 3, pp. 308–317, 2005.

[28]   S. Riffat and X. Ma, "Thermoelectrics: a review of present and potential applications," *Applied Thermal Engineering,* vol. 23, no. 8, pp. 913–935, 2003.

[29]   S.-Y. Park, M. A. Teitell, and E. P. Y. Chiou, "Single-sided continuous optoelectrowetting (SCOEW) for droplet manipulation with light patterns," *Lab on a Chip,* vol. 10, no. 13, pp. 1655-1659, 2010.

[30]   A. Gholizadeh and M. Javanmard, "Magnetically actuated microfluidic transistors: miniaturized micro-valves using magnetorheological fluids integrated with elastomeric membranes," *Journal of Microelectromechanical Systems,* vol. 25, no. 5, pp. 922–928, 2016.

[31]   M. Esashi, S. Shoji, and A. Nakano, "Normally close microvalve and micropump fabricated on a silicon wafer," *IEEE Micro Electro Mechanical Systems, Proceedings, An Investigation of Micro Structures, Sensors, Actuators, Machines and Robots ,* vol. 24, no. 2, pp. 29–34, 1989.

[32]   E. Stemme and G. Stemme, "A valveless diffuser/nozzle-based fluid pump," *Sensors and Actuators A: Physical,* vol. 39, no. 2, pp. 159–167, 1993.

[33]   T. Ishida, D. Mclaughlin, Y. Tanaka, and T. Omata, "First-come-first-store microfluidic device of droplets using hydrophobic passive microvalves," *Sensors and Actuators B: Chemical,* vol. 254, pp. 1005–1010, 2018.

[34]   E. Bassous, H. H. Taub, and L. Kuhn, "Ink jet printing nozzle arrays etched in silicon," *Applied Physics Letters,* vol. 31, no. 2, pp. 135–137, 1977.

[35]   P. Gravesen, J. Branebjerg, and O. S. Jensen, "Microfluidics-a review," *Journal of Micromechanics and Microengineering,* vol. 3, no. 4, pp. 168–182, Jan. 1993.

[36]   J. Cunneen, Y.-C. Lin, S. Caraffini, J. G. Boyd, P. J. Hesketh, S. M. Lunte, and G. S. Wilson, "A positive displacement micropump for microdialysis," *Mechatronics,* vol. 8, no. 5, pp. 561–583, 1998.

[37]   Z. Chen, P. Wang, and H.-C. Chang, "An electro-osmotic micro-pump based on monolithic silica for micro-flow analyses and electro-sprays," *Analytical and Bioanalytical Chemistry,* vol. 382, no. 3, pp. 817–824, Jan. 2005..

[38]   O. C. Jeong and S. Konishi, "Fabrication and drive test of pneumatic PDMS micropump," *Sensors and Actuators A: Physical,* vol. 135, no. 2, pp. 849–856, 2007.

[39]   A. Loth and R. Forster, "Disposable high pressure peristaltic micropump for standalone and on-chip applications," in *2016 IEEE 11th Annual International Conference on Nano/Micro Engineered and Molecular Systems (NEMS)*, 2016.

[40]   S. Nabavi and L. Zhang, "Design and Optimization of Piezoelectric MEMS Vibration Energy Harvesters Based on Genetic Algorithm," *IEEE Sensors Journal,* vol. 1, no. 2, pp. 7372-7382, 2017.

[41]   C. Mo, R. Wright, W. S. Slaughter, and W. W. Clark, "Behaviour of a unimorph circular piezoelectric actuator," *Smart Materials and Structures,* vol. 15, no. 4, pp. 1094–1102, Jul. 2006.

[42]   R. Kumar and V. Kursun, "Impact of temperature fluctuations on circuit characteristics in 180 nm and 65 nm CMOS technologies," *in IEEE Int. Symp. on Circuits and Syst.,* pp. 3858-3861, May 2006.

[43]   R. Kumar and V. Kursun, "Voltage optimization for simultaneous energy efficiency and temperature variation resilience in CMOS circuits," *Microelectronics J,* vol. 38, no. 4-5, pp. 583-594, Apr./May 2007.

[44]   B. Keane, G. Schwarz, and P. Thernherr, "Electrical equipment in cold weather applications," *Industry Applications Society 60th Annual Petroleum and Chemical Industry Conference,* pp. 1-7, 2013.

[45]   Y. Ji and C. Y. Wang, "Heating strategies for Li-ion batteries operated from subzero temperatures," *Electrochimica Acta,* vol. 107, pp. 664–674, 2013.

[46]   C.-Y. Wang, G. Zhang, S. Ge, T. Xu, Y. Ji, X.-G. Yang, and Y. Leng, "Lithium-ion battery structure that self-heats at low temperatures," *Nature,* vol. 529, no. 7587, pp. 515–518, 2016.

[47]   J. N. Reddy, "Nonlinear Bending of Elastic Plates and Shells," *An Introduction to Nonlinear Finite Element Analysis,* pp. 141–228, 2004.

[48]   H. Lam, F. Leung, and P. Tam, "Stability analysis and design of fuzzy observer-controller for fuzzy systems," *10th IEEE International Conference on Fuzzy Systems. (Cat. No.01CH37297),* vol. 3, pp. 1259–1262, 2001.

[49]   W. B. Xie, Y. L. Wang, J. Zhang, and L. Huang, "Membership function dependent observer-based controller design for a t-s fuzzy system," *Asian Journal of Control,* vol. 19, no. 4, pp. 1496–1507, 2017.

[50]   PRODUCTS, *Granta Design,* [Online]. Available: http://www.grantadesign.com/. [Accessed: 24-Nov-2017].

[51]   O. Gutmann, R. Kuehlewein, S. Reinbold, R. Niekrawietz, C. P. Steinert, B. D. Heij, R. Zengerle, and M. Daub, "A Highly Parallel Nanoliter Dispenser for Microarray Fabrication," *Biomedical Microdevices,* vol. 6, no. 2, pp. 131–137, 2004.

[52]   M. A. Renshaw, B. P. Olds, C. L. Jerde, M. M. Mcveigh, and D. M. Lodge, "The room temperature preservation of filtered environmental DNA samples and assimilation into a phenol-chloroform-isoamyl alcohol DNA extraction," *Molecular Ecology Resources,* vol. 1, pp. 127-136, 2014.

[53]   H. Ping-Yi, A.T. Chen, J. H. Lee, Y.W. Lu, and S. K. Fan, "Genetic testing on electrowetting-on-dielectric chips for magnetic bead-based DNA extraction," *In Proceedings of the 14th IFToMM World Congress,* pp. 47–51, 2015.

[54]   K. Rudi, M. Kroken, O. J. Dahlberg, A. Deggerdal, K. S. Jakobsen, and F. Larsen, "Rapid, universal method to isolate PCR-ready DNA using magnetic beads," *BioTechniques,* vol. 22, no. 3, pp. 506–511, 1997.

[55]   Y. Sheikhnejad, Z. Vujicic, Á. Almeida, R. Bastos, A. Shahparia, and A. Teixeira, "Analytical transient analysis of peltier device for laser thermal tuning," in *Third International Conference on Applications of Optics and Photonics*, Jun. 2017.

[56]   H. Grégoire, and J. Rushby, "An operational semantics for stateflow," *FASE,* vol. 2984, pp. 229-243, 2004.

[57]   M. Arik, S. M. Zurn, A. Bar-Cohen, and D. L. Polla, "Design, fabrication, and characterization of thin film PZT membranes for high flux electronics cooling applications," *Smart Materials and Structures,* vol. 14, no. 6, pp. 1239–1249, 2005.

[58]   Q. Cui, C. Liu, and X. F. Zha, "Modeling and Numerical Analysis of a Circular Piezoelectric Actuator for Valveless Micropumps," *Journal of Intelligent Material Systems and Structures,* vol. 19, no. 10, pp. 1195–1205, 2007.

[59]   E. Stemme and G. Stemme, "A valveless diffuser/nozzle-based fluid pump," *Sensors and Actuators A: Physical,* vol. 39, no. 2, pp. 159–167, 1993.

[60]   M. F. Ashby, in *Materials selection in mechanical design*, Amsterdam, Butterworth-Heinemann, 2017.

[61]   B. C. Gross, J. L. Erkal, S. Y. Lockwood, C. Chen, and D. M. Spence, "Evaluation of 3D printing and its potential impact on biotechnology and the chemical sciences," *Analytical Chemistry,* vol. 86, no. 7, pp. 3240–3253, 2014.

[62]   M. Parvin and J. G. Williams, "The effect of temperature on the fracture of polycarbonate," *Journal of Materials Science,* vol. 10, no. 11, pp. 1883–1888, 1975.

[63]   N. Armaroli and V. Balzani, "Towards an electricity-powered world," *Energy & Environmental Science,* vol. 4, no. 9, pp. 3193, 2011.

[64]   F. Wilson, "Ceramic heating element". U.S. Patent Patent 6,075,230, 13 Jun 2000.

[65]   E. Antonova and D. Looman, "Finite elements for thermoelectric device analysis in ANSYS," in *ICT 2005. 24th International Conference on Thermoelectrics*, 2005.

[66]   C. A. Boano, N. Tsiftes, T. Voigt, J. Brown, and U. Roedig, "The impact of temperature on outdoor industrial sensornet applications," *IEEE Transactions on Industrial Informatics,* vol. 6, no. 3, pp. 451–459, 2010.

[67]   J. Lau, Thermal Stress and Strain in Microelectronics Packaging, Verlag: Springer , 2012.

[68]   B. Li, Z. Yuan, Y. Xu, and J. Liu, "N-doped graphene as an efficient electrocatalyst for lithium-thionyl chloride batteries," *Applied Catalysis A: General,* vol. 523, pp. 241–246, 2016.

[69]   A. Sarkar, "Secured wireless communication using fuzzy logic based high speed public-key cryptography (FLHSPKC)," *International Journal of Advanced Computer Science and Applications,* vol. 3, no. 10, pp. 1-7, 2012.

[70]   G. Bosque, I. D. Campo, and J. Echanobe, "Fuzzy systems, neural networks and neuro-fuzzy systems: A vision on their hardware implementation and platforms over two decades," *Engineering Applications of Artificial Intelligence,* vol. 32, pp. 283–331, 2014.

Appendix: Published/Submitted Papers

[1] B. Parsi, L. Zhang, and V. Masek, "Vibration Analysis of a Double Circular Pzt Actuator for a Valveless Micropump," *CSME International Congress 2018,* May 27-30, 2018, Toronto, On, Canada.

[2] B. Parsi, L. Zhang, and V. Masek, " Disposable Off-chip Micro-dispenser for Accurate Droplet Transportation," *Submitted to IEEE Sensor Journal*, June 2018.

[3] B. Parsi and L. Zhang, "Design and Optimization of Cost-Effective Coldproof Portable Enclosures for Polar Environment," *Submitted to IEEE Transactions on Consumer Electronics*, May 2018.